Julius Flitsch M.Eng.

Characterization of the flow resistance and deformation relationship of wood fiber mats

DOCTORAL THESIS

to achieve the university degree of

Doktor der technischen Wissenschaften

submitted to

Graz University of Technology

Supervisor

Prof. Dr. Wolfgang Bauer

Graz University of Technology, Institute for Paper, Pulp and Fiber Technology

Prof. Dr. Steven Keller
Miami University, Department of Chemical, Paper and Biomedical Engineering

Graz, November 2017

AFFIDAVIT

I declare that I have authored this thesis independently, that I have not used other than the declared sources/resources, and that I have explicitly indicated all material which has been quoted either literally or by content from the sources used. The text document uploaded to TUGRAZonline is identical to the present doctoral thesis.

Date

Signature

Like some other arts,
papermaking has been tending to become a science.

W.B. Campbell, 1947

Characterization of the flow resistance and deformation relationship of wood fiber mats

by

Julius Flitsch

This thesis presents a novel test device to investigate the effect of pressure and time on the flow resistance and compressive behavior of fiber mats. The test device uses a filtration cell with continuous water flow. Most previous investigations into the flow of a liquid through a fiber mat have dealt separately with either the measurement of flow velocity or mat height. The new test device described here allows investigation of both parameters simultaneously. The experiments were conducted on fiber pads at 40 and 80 g/m^2 and with three pulp types: hardwood, softwood and a recycled pulp. The results show that the relationship between flow resistance and pressure drop follows a power law function. The fiber mat height is proportional to the flow resistance for a pressure range between 10 kPa and 80 kPa. The investigation of the rheological components of the fiber mat during the compression reveals elastic, viscoplastic and plastic behavior.

The presented simulation of a double wire former segment shows the influence of backflow on the pressure profile along the model domain. In the case of backflow, water flows from outside of the wire into the gap between the wire and the fiber mat forming a liquid layer. The model simulates the forming of the liquid layer and considers the change of the flow resistance. In the model it is assumed, that only the flow resistance of the wire instead of the combination of the flow resistance of the wire and the fiber mat is present in case of backflow. Thus, in this model, the flow resistance depends on the flow direction of the liquid. The model domain covers the unsupported wire between the forming roll and the first blade. This includes the calculation of the release point of the wire from the forming roll.

The simulation results show a good agreement to the pressure measurements at an industrial double wire former. This includes the positive as well as the negative pressure levels. This good agreement is only possible due to the flow-direction-dependent flow resistance.

Keywords: Fiber, compression, expansion, sheet forming, filtration resistance, pressure pulse, former simulation, former dewatering, paper machine simulation, fiber mat simulation.

Charakterisierung des Fließwiderstandes und des Deformationsverhaltens von Holzfasermatten

von

Julius Flitsch

Diese Arbeit beschreibt ein neu entwickeltes Messgerät zur Untersuchung des Fließwiderstandes und der Fasermattenkompression in Abhängigkeit von Druck und Zeit. Das Messgerät verwendet eine Messzelle in der die Fasermatte kontinuierlich mit Wasser durchströmt wird. Bisherige Arbeiten auf dem Gebiet der Durchströmung von Fasermatten untersuchten die Fließgeschwindigkeit des durchströmenden Fluids und die Fasermattenhöhe in zwei getrennten Messvorgängen. Das in dieser Arbeit vorgestellte Messgerät erlaubt die Messung von Fließgeschwindigkeit und Fasermattenhöhe während eines Messvorgangs. Die Versuche wurden an Papierfasermatten mit 40 g/m² und 80 g/m² durchgeführt. Getestet wurden drei Fasertypen: Laubholz-, Nadelholz- und Altpapierfasern.

Die Ergebnisse zeigen, dass die Beziehung zwischen Fließwiderstand und Druckverlust einem Potenzgesetz folgt. Für einen Druckbereich zwischen 10 kPa und 80 kPa ist die Fasermattenhöhe proportional zur Fließgeschwindigkeit. Die Untersuchung der rheologischen Eigenschaften einer Papierfasermatte ergab eine Kombination aus elastischem, viskoplastischem und plastischem Verhalten.

Die in dieser Arbeit durchgeführte Simulation eines Doppelsiebformers im Bereich der Blattbildung zeigt den Einfluss von Rückströmungen in das Innere des Siebspalts auf das Druckprofil im Suspensionskern. Durch die Rückströmung in das Innere des Siebspaltes bildet sich eine Wasserschicht zwischen Sieb und Fasermatte. Das Modell simuliert die Entstehung dieser Wasserschicht und berücksichtigt die Änderung des Fließwiderstandes. Im Modell wird dabei angenommen, dass bei Rückströmung nur der Fließwiderstand des Siebes wirkt. Bei einer Entwässerung hingegen, wird die Summe aus dem Fließwiderstand des Siebes und der Fasermattenwiderstand verwendet. Dadurch ist im Modell der Fließwiderstand abhängig von der Fließrichtung der Flüssigkeit. Das Modell beschreibt den Abschnitt zwischen Formierwalze und Formierleiste in der das Sieb ungestützt ist und in dem sich das Sieb von der Formierwalze ablöst. Die Simulation zeigt eine gute Übereinstimmung mit den Druckmessungen eines industriellen Doppelsiebformers. Dies gilt sowohl für den positiven als auch negativen Druckbereich.

Schlagworte: Papierfaser, Kompression, Expansion, Blattbildung, Fließwiderstand, Druckpuls, Siebpartiesimulation, Siebpartieentwässerung, Papiermaschinensimulation, Fasermattensimulation.

Acknowledgements

There are many people to whom I am indebted for their help and encouragement during the course of this thesis. First of all, I wish to thank my academic supervisor Professor Wolfgang Bauer. His guidance, support, constructive criticism, and discussions improved this thesis. I am also grateful to my second supervisor, Professor Steven Keller from the Department of Chemical, Paper and Biomedical Engineering, for his helpful comments throughout the completion of this thesis.

I would also like to thank Christian Naydowski from Voith Paper for the opportunity to conduct this research. A great debt is owed to my fellow worker for their contributions, and the superb working atmosphere and team support throughout the last years. Very special thanks to Jens Haag and Siegfried Graser for the fruitful collaboration, innumerable stimulating discussions, help, and inspiration. Their careful review of the thesis manuscript was invaluable.

Finally, I owe my deepest thanks to my family. My parents Sieglinde and Klaus Flitsch and my sisters Johanna and Lisa for their help and encouragement during all these years.

Julius Flitsch
München, 07 November 2017

Contents

List of Figures

List of Tables

Nomenclature

AR	fiber aspect ratio	
A_{sp}	specific surface area of the fibers	(m^2)
a	fitting parameter	
B	basis weight	(kg/m^2)
b	fitting parameter	
c	solid concentration	(kg/ m^3)
c_{mat}	concentration of the fiber mat	(kg/m^3)
c_{sus}	concentration of the suspension	(kg/m^3)
c_{vol}	Volume concentration	
E	modulus of elasticity	(Pa)
e	porosity	(m^3 solid fraction/ m^3 total volume)
F_{drag}	drag forces which are generated by the flow	(N)
F_h	hydrodynamic drag forces from the fluid to the fibers	(N)
F_{sup}	network forces which fix the individual fiber in the network	(N)
$\bar{f}$	direct path from the center roll to the blade of the upper wire	(m)
$\tilde{f}$	deflected path from the center roll to the blade of the upper wire	(m)
f	position upper wire	(m)
G	shear modulus	(kg/ms^2)
g	position lower wire	(m)
$\bar{g}$	direct path from the center roll to the blade of the lower wire	(m)
$\tilde{g}$	deflected path from the center roll to the blade of the lower wire	(m)
h_{df}	height of the drag water outside of the wire	(m)
$h_{f,0}$	height of the liquid layer	
h_m	height of the fiber mat	(m)
h_w	height of the wire	(m)

K	permeability constant	(m^2)
K_l	Kozeny constant	
k	control variable	
L	mat height	(m)
m_f	mass of the liquid	(kg)
m_m	mass of the fiber mat	(g)
n	number of compressions	
n_r	compressibility indicator	
$\hat{n}$	direction normal to the wire surface	
p	pressure	(Pa)
$p_{adapter}$	pressure across the wire	(Pa)
p_{comp}	pressure during the compression state	(Pa)
p_d	doctoring pressure	(Pa)
p_e	exterior pressure	(Pa)
p_{exp}	pressure during the expansion state	(Pa)
p_h	liquid pressure	(Pa)
p_{ini}	reference pressure before compression	(Pa)
p_s	network pressure	(Pa)
p_{sus}	pressure between the wires	(Pa)
p_{stat}	static pressure	(Pa)
r_{cont}	specific filtration resistance calculated by results of continuous loading experiments	(m/kg)
r_{ctd}	specific filtration resistance caused by time-dependent compression.	(m/kg)
r_{disc}	specific filtration resistance calculated by the results of discontinuous loading experiments	(m/kg)
r_{el}	specific filtration resistance caused by elastic deformation	(m/kg)
r_{epd}	specific filtration resistance caused by pressure-dependent expansion	(m/kg)
r_{etd}	specific filtration resistance caused by time-dependent expansion	(m/kg)
r_{ini}	initial specific filtration resistance	(m/kg)
r_{lin}	linear change in specific filtration resistance	(m/kg)
r_{nonl}	nonlinear specific filtration resistance	(m/kg)
r_{pdc}	specific filtration resistance caused by pressure-dependent compression	(m/kg)/ (m/kg)
r_{pl}	plastic change of specific flow resistance	(m/kg)
r_{tot}	total change of specific flow resistance	(m/kg)

r_{viscel}	viscoelastic change of specific flow resistance	(m/kg)
r_{viscel}	viscoplastic change of specific flow resistance	(m/kg)
$r_{viscoel}$	specific filtration resistance caused by viscoelastic deformation	(m/kg)
$r_{viscopl}$	specific filtration resistance caused by viscoplastic deformation	(m/kg)
R	specific flow filtration resistance	(kNs/m^3)
$\widetilde{R}$	hydraulic conductivity	(kNs/m^3)
Re	Reynolds number	
R_m	specific flow resistance of the fiber mat	(kNs/m^3)
R_{tot}	specific flow resistance of the wire and the fiber mat	(kNs/m^3)
R_w	resistance of the wire	(kNs/m^3)
S_V	specific surface of the fiber	(m^2/m^3)
t	time	(s)
t_{n_i}	time of pressure pulse	(s)
t_{cont}	time during which the fiber mat is loaded	(s)
t_{disc}	sum of every single pulse length	(s)
T_i	tension of the wire	(N/m)
t_k	pulse lengths	(s)
$\hat{t}$	direction tangential to the wire surface	
U	velocity of the wire	(m/s)
u_f	velocity of the liquid	(m/s)
u_{grow}	velocity with which the fiber mat grows	(m/s)
u_m	velocity of the fiber mat	(m/s)
$\mathbf{u_m}$	velocity vector of the particular segment of the suspension	(m/s)
u_s	velocity of the suspension in machine direction	(m/s)
u_{sus}	velocity of the suspension	(m/s)
u_w	velocity of the wire in machine direction	(m/s)
$\mathbf{u_w}$	velocity vector of a particular segment of the wire	(m/s)
v	flow velocity	(m/s)
V_{bulk}	total volume	(m^3)
v_{comp}	flow velocity during compression	(m/s)
v_{exp}	flow velocity during expansion	(m/s)
v_{ini}	reference flow velocity before compression	(m/s)
$v_{loc,i}$	flow velocity dependent on t_{n_i}	(m/s)
V_{solid}	volume of fibers	(m^3)
w_s	velocity of the suspension in machine direction	(m/s)
w_w	velocity of the wire in machine direction	(m/s)

$\tilde{x}$	release point of the lower wire from the center roll	(m)
α	capillary diameter	(m)
ϵ	modified strain for compression	(m/m)
ϵ_{min}	modified strain for expansion	(m/m)
ϵ_{re}	modified strain for reloading	(m/m)
η	dynamic viscosity	(Pa*s)
ρ_{bulk}	bulk density	(kg/m^3)
ρ_{fl}	density of the liquid	(kg/m^3)
ρ_{solid}	solid density	(kg/m^3)
θ	initial time	(s)
σ	stress	(Pa)
σ_{fc}	applied stress	(Pa)
σ_{re}	stress during reloading	(Pa)
σ_{un}	stress during unloading	(Pa)
σ_v	threshold stress	(Pa)

Chapter 1

1 Introduction

The paper production process is, simply put, a dilution and a dewatering of a wood fiber suspension. In the stock preparation section of a paper machine, the manipulation of the concentration is used for cleaning and a more efficient dispersion of the wood fibers. The dewatering in the forming section of a paper machine essentially defines the final sheet properties, the machine runability, and the energy consumption.

The sheet forming process requires a huge amount of water to achieve a homogenous distribution of fibers both in the suspension and in the final sheet. The mass-specific concentration at this production stage is typically 99% of water and 1% fibers. Numerous investigations were carried out in order to increase the specific mass concentration and reduce the energy, needed to remove the water. In these investigations, it was observed that with an increase of the concentration of the stock at the headbox the uniformity of the fiber distribution decreases and the visual appearance of the final paper sheet deteriorates from a quality perspective. For this reason, the concentration for graphical paper is limited to a maximum of about 1.5%.

Throughout the last century, efforts have been made trying to replace the water by other substrates like alcohol or foam. Ng, Grandmaison, & Topolinsky (1990) and Ng (1990) investigated the possibility to create a sheet with an air stream. In theory, this system would totally remove the need for water. However, in a dry environment the fibers do not form hydrogen bonds between each other. Such bonding only occurs in the presence of water. This fact limits the advantage of air stream formation because in order to form a cohesive network the fibers would eventually have to get in contact with water.

Another promising technology, which uses significantly less water than the traditional forming process, is foam forming (Radvan & Gatward, 1972). A mixture

of foam and fibers is transported through the headbox and distributed on the wire. The foam is then removed by vacuum. Surfactants are needed to generate and stabilize the metastable foam. The VTT Technical Research Centre of Finland has recently investigated this technology for several years. One of the most recent publications was presented by Torvinen & Kiiskinen (2014). They showed the application of foam forming in an industrial environment with promising results.

Despite these developments, no alternative technology exists, so far, that replaces the forming of the sheet using a large amounts of water. There is a need for further optimization of the traditional process, to reduce the consumption of resource, and to improve the paper quality.

In order to optimize the traditional process of sheet forming, it is important to understand the phenomena during the dewatering in the forming section of a paper machine. The most representative information could be obtained by analyzing the fiber mat structure and hydrodynamic conditions directly inside an industrial former. But this is only possible to a limited extent. There investigations of the flow resistance are restricted to analyzing the boundary states, like the flow rates of the suction boxes, as well as the effect of typically adjustment parameters, like the slice lip of the headbox and the vacuum of the suction boxes, on the network structure in the final paper. It is not even possible to get information on the conditions of the suspension at previous stages like in the headbox or in the approach flow system. The effects of process parameters are typically evaluated by the drainage, the retention, and the final sheet properties. There are only a few investigations that give a approximation of the mechanism inside the former. Hergert & Sandford (1982) and Holm et al. (2005), for example, measured the pressure distribution at the very early forming process in a double wire former. These comprehensive works showed how the geometries and the permeability of the fiber mat influence the local pressure drop. However, they do not deal with the compression behavior of the fiber mat and its local macroscopic condition. Other kinds of investigation are particle-level simulations of fibers during the build-up of a fiber mat (Gren & Ljungkvist, 1983; Lindström, 2008). These investigations show the fundamental fiber movement during the fiber mat forming process. However, they assume only a simplified paper structure, neglecting, for instance, detailed fiber morphology and suspension components. These models allow a rough estimate of the fiber mat permeability.

A macroscopic simulation of the dewatering process in a former was done by Green & Kerekes (1998) and Holmqvist (2002) for example. They simulated the dewatering and the pressure inside the suspension along the dewatering process in a former. They modeled the fiber mat as a continuum and used empirical dewatering curves from fiber mats, which were generated with laboratory trials using filtration cells. The disadvantage of these models is the inaccuracy of the simulation results. The

pressure inside the suspension and thus the dewatering velocity show, for low filtration resistances, a good agreement with measured values at a real former. For high filtration resistances, the simulation shows an oscillating behavior.

The common technology used to experimentally investigate the fiber mat behavior during the filtration process involves filtration cells, as they are used in the works of Kalliokoski (2011), Kataja & Hirsilä (2001), Pires et al. (1989) and Wildfong (2000a). These cells are vertical tubes, which are filled with the suspension of water and fibers. At their bottom, a wire is installed on which the fibers are deposited. Depending on the focus of the investigations, different configurations are available. However, the validity of the laboratory results in an industrial environment is only limited.

The limitations of this approach can be summarized as follows:

- Mechanical conditions: In case of a double wire former, dewatering occurs at the bottom and upper wire instead of the one-sided dewatering of the filtration cell. Between these two wires complex shear and turbulent flow conditions exist. Also, the local wire tension, curvature, and thus the local wire permeability vary significantly along during dewatering. In a test apparatus, laminar flow is typically used, and the wire is clamped into a planar adapter.
- Process dynamics: Dewatering in an industrial paper machine takes less than one second and the pressure varies with high frequency during dewatering. Under typical experimental conditions, the dewatering takes several minutes and the hydrostatic pressure is constant.
- Suspension composition: Typically, the process water has a complex chemical and biological composition. The same is true for the solid fractions of the suspension with a mixture of fresh fibers, broke fibers, and recovered fibers. In typical laboratory experiments, a simplified stock composition is used.

In order to overcome most of the disadvantages of the previously used test devices, an apparatus was designed to represent, as close as possible, the suspension composition and the hydrodynamic dewatering characteristics in a double wire former. The new design is based on a filtration cell with continuous flow. During the trials, the fiber mat was loaded with hydrostatic pressure pulses. During the complete trial series, the hydrostatic pressure and the pulse length were varied. The flow resistance and the mat height during compression and expansion were investigated. The test furnishes were bleached mechanical softwood kraft pulp (LF), bleached hardwood eucalyptus pulp (SF) and deinked news paper pulp (RF).

The results were used to characterize and model the flow resistance during loading and reloading of the fiber mat. This knowledge was used to support the development of a double-wire former simulation model, which describes the pressure gradient and dewatering in machine direction. The former model is an extension of the model of Holmqvist (2002). In contrast to the model of Holmqvist, the model presented here distinguishes between the combined flow resistance of the wire and the fiber mat, in the case of dewatering flows, and the resistance only from the wire in the case of backflows. Another extension of the model is the inclusion of a doctoring pressure at the edge of a blade which was original introduced by Roshanzamir et al. (1999). It can be shown that these extensions lead to higher accuracy of the simulation results at high filtration resistance.

1.1 Motivation for characterizing the filtration process

Throughout the last decade, the development of paper machines has been moving towards faster and more efficient production. This trend leads to complex systems with more and more adjustment options and higher process sensitivity. Typical adjustment options for modern former types are the suction pressure, blade pressure and wire tension.

An example of the complexity of such a system is shown in FIGURE 1.1, where the pressure inside the suspension at a forming blade of a double wire former is shown (Schmidt-Rohr, 2007). Schmidt-Rohr used capillary which was inserted in the gap between the top and the bottom wire in order to measure the pressure. The method was also used by Gooding et al. (2004). The curves show three different process settings for the suction pressure and the basis weight. The characteristic trends are similar for each measurement, but the details of the local pressure varies for the different settings.

At the same basis weight, an increase of the vacuum in the suction box from 1 kPa to 5 kPa leads to a decrease of the suspension pressure from approximately 220 mbar to 150 mbar. If the basis weight decreases from 80 g/m^2 to 40 g/m^2, the pressure in the suspension decreases from 220 mbar to 130 mbar. These changes can be traced back to changes of the flow resistance and wire trajectory along the blade. This can be derived by the simulation results of Holmqvist (2002). These values are not measured and impossible to predict.

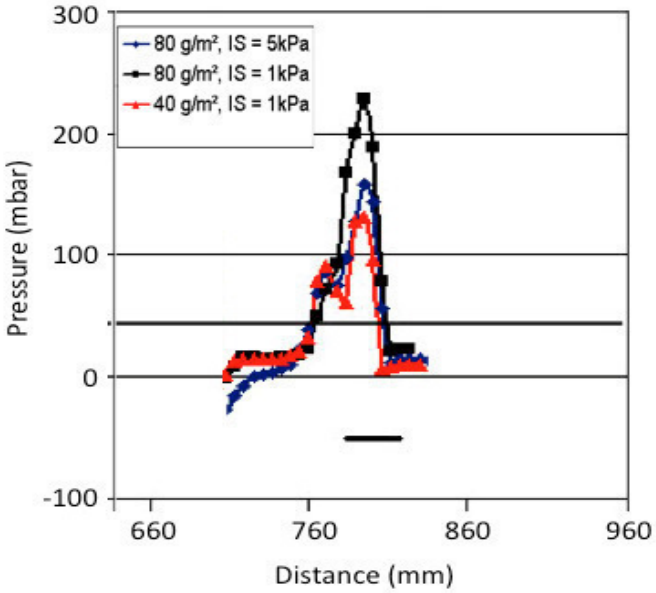

FIGURE 1.1: Pressure distribution along the blade section of a double wire former. The measurement was presented by Schmidt-Rohr (2007). The same method was also used by Gooding et al. (2004). The figure shows the pressure distribution for three different process settings of a double wire blade former. The line at the bottom of the figure indicates the position of the blade. The results show a similar overall pressure characteristic for all three different process settings. Differences of the pressure profile are only significant at the end of the blade.

It is well known that different pulp types show different behavior in retention, dewatering and network structure due to the different properties in shape, sizes and flexibility (Sayegh & Gonzalez, 1995). An exact prediction of the behavior of an unknown pulp composition is usually not possible.

Representative laboratory tests and modern simulation tools offer a high potential to decrease the resource consumption by the use of model based controls, to accelerate developments of new former concepts and to increase the product quality.

Model based controls and sensors

In the age of "Industry 4.0" the degree of automation of industrial plants increases. One interpretation of this industrialization phase for the paper industry can be a complete vertical and horizontal integration of plant management systems, sensors, and controls. The development of sensors is therefore a key component to increase the information level in order to evaluate processes and derive actions. The development of new sensors is slow and expensive. Nevertheless, the market demands for low-energy and resource-saving processes, as well as enhanced product quality, can only be fulfilled, if process and quality measurements are available to optimize the

processes. To supply the operator with information regarding the current status of the process, simulations are an adequate and common method to predict process data, which are not directly measurable at a running machine. Another application of a process modelling is the integration of the model into a model-based control for complex systems. The simulation of the former section for a model-based control, and the automatic adjustment of process parameters, like slice lip former, vacuum of the suction boxes and wire tension contain a considerable potential to reduce the drive load, to save retention agents and pump energy, and to reduce the wear of the forming wire.

Former design

The design of a new paper machine is still more or less a transfer of the experiences from existing machines with adjustments made for the desired production specifications. Site specific conditions, such as pulp quality, are only incorporated to a limited extent. In order to fulfill the construction specifications, high safety margins are added. The results are unnecessary equipment costs and a high optimization need for new machines. A more precise prediction of the dewatering behavior of a specific pulp quality in a former section would allow a reduction of capital investment and operating costs.

Paper properties

A general challenge for industrial manufacturers is to produce high quality products at low operating costs. In the case of a testliner paper board, high quality means low air permeability and high material strength. These quality parameters are determined by specific fiber network structures. Air permeability decreases if the network is compacted and the void volume is low. Paper strength is mainly influenced by the directionality and the bonding of the fibers. The crucial process step to influence the network structure is the dewatering process of the fiber suspension (Parker, 1972). More specifically, three different hydrodynamic processes exist, which determine the characteristic of the fiber network: drainage, oriented shear and turbulence (FIGURE 1.2). Drainage is the flow of water from the fiber mat. It determines the path of transport and the final position of fibers and fillers. Thus, the local concentration in z-direction of the paper and the incorporated degree of mobility of fibers and fillers are defined. The oriented shear is characterized by a velocity gradient perpendicular to the MD/CD plane along the direction of the wire movements. It results in an orientation of the fibers in the free suspension. Through the drainage, the orientation remains constant, and is fixed when the fiber settles on the surface of the wire. Turbulences leads to a breakup of flocculated fibers and to a homogenization of the fiber distribution.

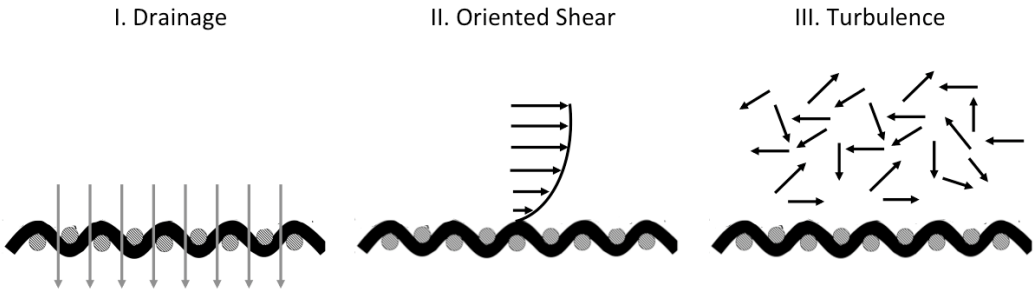

FIGURE 1.2: The three flow regimes during the drainage of the suspension (adapted from Parker (1972)).

The intensity of the hydrodynamic processes are mainly determined by the mobility and thus by the local concentration of the suspension. The concentration and the dewatering, respectively, in a former section can be adjusted by machine parameters like the slice lip opening or the vacuum of the suction boxes. The relationship between the settings of the machine parameter and the intensity of the hydrodynamic processes are nonlinear. If the operating costs are considered, it is a more dimensional nonlinear relationship between the intensity of the hydrodynamic processes, machine parameter and operating costs. So, there is an optimum at which the highest quality at the lowest operating costs is achieved. It is therefore essential to know the local concentration and the influence of machine parameter to the concentration, in order to coordinate the intensity of drainage, oriented shear and turbulences in the most efficient way.

Machine operation

In the former section of a paper machine, high operational costs are required for removing water from the fiber suspension. These costs can be reduced by optimizing vacuum settings during dewatering. In an industrial environment, such an optimization is not carried out because there is no general strategy known yet. Vomhoff & Schmidt (1997) give one example which describes the complexity of the dewatering and sheet formation process. They report cases where the drainage does not increase when the vacuum increases which is typically expected. The individual process behavior of paper machines is therefore not known *a priori*. One way to optimize the process is by trials However these are time intensive and possibly disturb the production.

An alternative to process trials is the simulation of the process. Process configurations and the individual process behavior can be implemented in the model. The simulation results are then used to optimize the process settings and to define operation strategies. Even though the simulation needs to be adapted to the process by

empirical process data or laboratory data, the effort is significantly lower than for industrial trails, and the results can be of significant value.

1.2 Background

The presented work is a part of a project in which an automated process control system for the dewatering of a double wire former is developed. The project is funded by Voith Paper. In the project, Jens Haag and I were working in the following areas:

- Development of a test device which represents the dewatering in a double-wire former as realistic as possible, in order to characterize the dewatering behavior of a wood fiber mat.
- Modeling of the dewatering in a double wire former to characterize the influence of typically changed process parameters such as slice lip gap, wire tension and vacuum pressure.
- Development of a model which can be used in a model based process control.

1.3 Thesis Outline

This thesis deals with the characterization of the flow through a wood fiber mat under hydrostatic compression at laboratory scale as well as in a simulated industrial environment.

The literature review in Chapter 0 reveals that only limited information about the flow resistance behavior of a fiber mat under hydrodynamic compression is available. In conclusion, the literature review shows the need to quantitatively and qualitatively determine the deformation components like viscoelastic, viscoplastic, plastic and elastic deformation and their influence on the filtration resistance. The models for the flow through a wood fiber mat in a double wire former which are available in the literature show unrealistic results at high flow resistance. In order to simulate the pressure distribution and drainage velocity at a double wire former with a higher predictive quality, modifications of the existing models must be elaborated and incorporated.

In Chapter 3 a test device is presented to investigate the relationship between flow velocity, pressure loss, and fiber mat height during the flow through a fiber mat. The results of the test device are validated and are in good agreement with existing the data from literature. The experimental results were used to calculate the changes in the filtration resistance due to viscoelastic and viscoplastic, as well as the plastic and

elastic deformation. The separation of the deformation components showed that the changes in the filtration resistance due to viscoelastic and viscoplastic deformation at time spans smaller than 75 ms are one order of magnitude smaller than the changes in filtration resistance due to pure elastic and pure plastic deformation that occur in the first few milliseconds, which are considered to be time-independent. For the simulation of the fiber mat in an industrial former section viscoelastic and viscoplastic deformations can be neglected, since the time spans of the pressure pulse are smaller than 30 ms.

In Chapter 4, a simulation model of a double wire former segment is presented. It shows the influence of backflow on the pressure profile along the machine direction. The simulation results are in good agreement with the pressure measurements for an industrial double wire former. This includes the positive as well as the negative pressure levels. It can be assumed that this agreement is caused by the flow-direction-dependent flow resistance. This means that in the case of backflow, one has to consider only the flow resistance of the wire, instead of using the combined flow resistance of the wire and the fiber mat, as was performed by Holmqvist (2002) and Zhao & Kerekes (1995). With their approach, the simulation results showed an oscillating pressure at a flow resistance level of approximatelly 70 kNs/m^3 which corresponds to a basis weight of 10 g/m^2. In this work an initial flow resistance of 700 kNs/m^3 is assumed, and the results show no oscillation in the pressure distribution along the machine direction.

Chapter 2

2 A review regarding wood fiber mat characterization

This chapter shows a literature review of previous investigations that deals with flow resistance and deformation behavior of wood fiber mats and former modeling. In section 2.2 the paper making process with its sub-processes is explained. Section 2.3 and 2.4 show methods currently used and the state of knowledge to characterize and model the filtration resistance and the compression behavior, respectively. The focus is on the discussion of methods to determine pressure related changes in flow resistance and its behavior under dynamic conditions. In section 2.5, existing models of the dewatering in a double wire former are presented. The advantages and disadvantages of these models are discussed in detail.

2.1 Introduction

Characterization and Modeling of the drainage behavior in a double wire former is a complex problem. The existence and the magnitude of the influences of various drainage phenomena are highly dependent on the boundary conditions. There are some conflicting requirements which should be met to accomplish the objective of this study.

- As explained by Ingmanson & Andrews (1959), the discrepancy between laboratory and industrial filtration analysis can be related to time effects. For instance, the dewatering process in a modern double wire former at a machine speed of 1600 m/min takes approximately 100 to 200 ms. Typical

test times at a laboratory apparatus are in the range of minutes. The apparatus, which was developed for this work, should be able to represent the time scales of an industrial gap former.

- It is known, that the filtration resistance depends on the compression history of the fiber mat (see Wilder, 1960). For the modeling of a non-monotonic compression behavior, typically an incremental formulation is used. Within this approach a complex equation system is created. The numerical methods, which are used in this work, are not robust enough to solve such an equation system. The complexity of the model, which is developed in this work, should be suitable for the numerical method used in this work. Nevertheless, the model must represent all relevant phenomena during the filtration process to offer high precision and prediction power.

- Literature provides various former models, which vary significantly at small-scale level. There are particle-level simulations that require high-intensive computational efforts (Lindström, 2008) and simple analytical calculations with insufficient model accuracy (Jong, 1998). The objective of this work is to develop a model with a high numerical stability, and a suitable level of detail to represent the process behavior of typical process settings during the operation of an industrial paper machine.

2.2 Papermaking process

2.2.1 Paper machine and sheet forming

In a paper machine, the sheet is formed and the water of the formed paper web is gradually removed. This is performed in several steps, which are shown in FIGURE 2.1. The first step is the sheet forming process. This is achieved by the distribution of a fiber suspension over the width of a wire. The concentration of the suspension at this process step is approximately 100- 200 kg water/kg fibers. The uniform distribution is achieved by a slotted nozzle, which is called headbox. The suspension dispersed on the top of the wire is drained mainly by momentum induced or mechanical vacuum. The suspension leaves the wire section with a water content of approximately 5 kg water/kg fibers. In the press section, the water is removed from the suspension by pressing. The fiber mat is transported between two felts and passes between several roll nips. The water content of the fiber mat after the press section is approximately 1 kg water/kg fibers. In the drying section, the remaining water is removed by thermal

energy. The wet paper gets in contact with steam-heated cylinders alternating form both paper sides. At the end of the paper machine, the fiber mat has a water content between approximately 0.03 to 0.07 kg water/kg fibers.

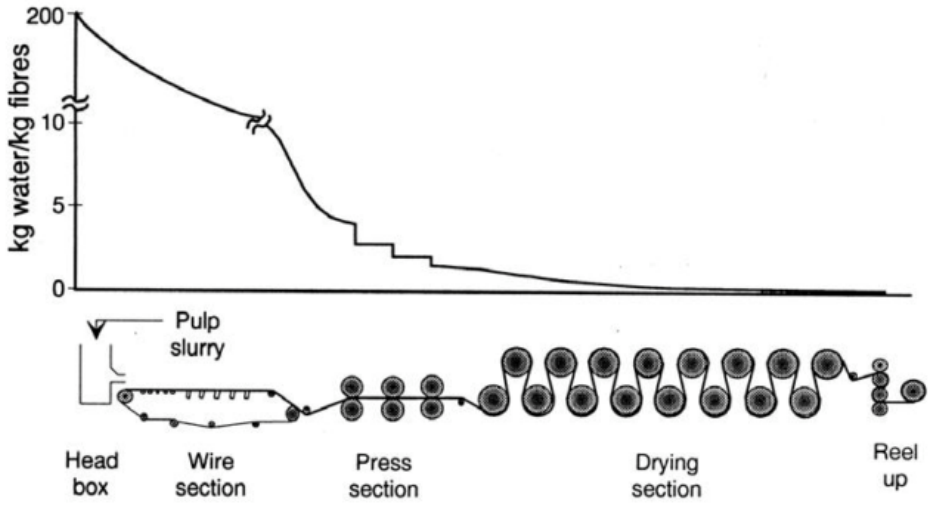

FIGURE 2.1: Paper machine sections and the local specific water content (Krook, 1996).

The focus of this work is the dewatering in the wire section, which is also called forming section. There are basically two wire section configurations widely used for communication papers. The Fourdrinier wire section, which carries the suspension on the top of a single wire. A schematic layout of such is displayed in FIGURE 2.1. In the 1960s, a new former section was developed, which is called double wire, twin wire, or gap former, shown in FIGURE 2.2. Since this thesis deals with the double wire former the corresponding sheet forming process is explained in more detail. The sheet forming process starts with the distribution of the wood fiber suspension by a slotted nozzle. A water jet is generated and injected between two converging plastic meshes called the forming wires. Schematically, the headbox and the configuration of a roll former is displayed in FIGURE 2.2. At the impingement point of the jet, two rolls, which are called forming roll and breast roll, support the wires and ensure the removal of the drained water. In the next dewatering step, the water is removed by a vacuum box, called the forming box. In the blade section bars are pressed against the wire. These bars cause turbulences and shear forces between the wires leading to a uniform distribution of mass distribution. The wire suction roll is a vacuum roll with an open structure in the cover. The water is removed through the holes into the cylinder.

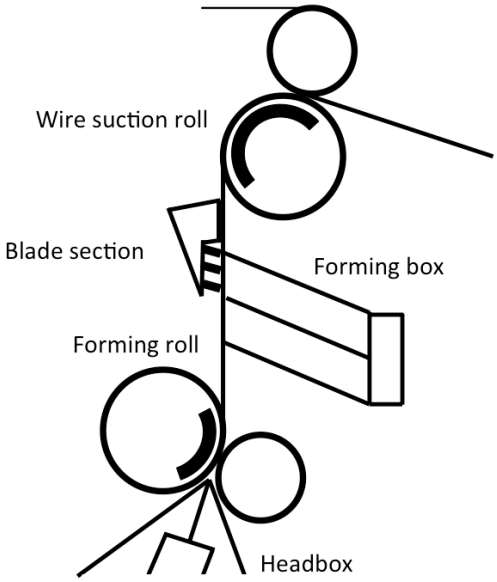

FIGURE 2.2: Double wire former with a headbox, forming roll and box and blade section.

The fundamental hydrodynamic mechanisms of the dewatering processes in the wire section are therefore drainage, oriented shear, and turbulences (Parker, 1972). An illustration of these processes is shown in FIGURE 1.2.

2.2.2 Dewatering

In the drainage process the water flows through the forming fabric and the fiber mat grows continuously. According to Parker (1972), the hydrodynamic drag forces cause a movement of fibers and fines perpendicular to the forming wire. The solid fraction is retained and accumulated on the surface of the forming wire. According to this description, oriented shear is the result of a velocity gradient in the suspension transversal to the forming wire. Horizontal and vertical movements of the fibers and fines influence the sheet forming process. Turbulent flow is an apparent three-dimensional chaotic flow regime, which promotes the homogenization of the suspension.

Baines (1967) characterized the drainage process at different process steps along the dewatering in a double wire former. He introduced three distinct zones in a twin wire former: the free-jet zone, the wedge zone, and the press zones as shown in FIGURE 2.3.

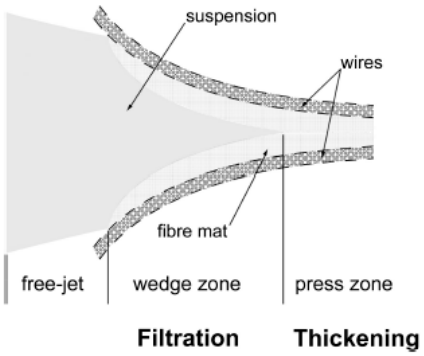

FIGURE 2.3: Process steps during sheet creation process (Lobosco, 2005)

In the free-jet zone, the fiber pulp suspension is transported from the headbox to the impingement point on the forming wire, which is located where the upper and lower forming wire converge in a narrow nip. The next zone is the wedge zone, in which the suspension starts to drain and the fiber mat is built on the surfaces of the forming wire. As soon as the suspension core is removed and both fiber mats get in contact with each other a networked fiber mat is formed and the fiber mat enters the press zone (Lobosco, 2004).

According to Hisey (1956), the dewatering process can be characterized by two dominating dewatering processes. These processes are filtration and thickening. Schematic illustrations of these processes are shown in FIGURE 2.4. The dewatering starts with filtration. It is characterized by mobile fibers in a suspension, which are deposited on the surface of the wire. This mechanism occurs mainly in the wedge zone. Thickening takes place when a mat is formed with networked fibers and with an increasing concentration. The mobility of the fibers decreases (see Parker, 1972). In a paper machine, thickening is the dominating process in the press zone when the wire is pressed against the network, being compressed. A detailed description of this mechanism is given by Norman & Söderberg (2001).

FIGURE 2.4: Schematic illustration of the dominating dewatering processes. During the sheet forming processes filtration (left) and thickening (right) occurs.

2.3 Governing equations for filtration resistance

The paper fiber mat consists of networked single wood fibers with open channels. The fibers can be described as a solid volume, and the open channels as a void volume. The sum of the solid and void volumes is the total volume of the fiber mat. The ratio between the void volume and the total volume is the porosity of the fiber mat. The flow through a porous medium can be described by a fundamental filtration equation, which is derived from filtration theory. The filtration equation for the stationary one-dimensional case is (Ripperger, 2005):

$$v = \frac{\Delta p}{\eta R} \quad , \tag{2.1}$$

where v is the fluid velocity, Δp is the pressure drop through the porous medium, η is the dynamic viscosity and R is the total hydraulic resistance. This equation includes no material and boundary conditions.

Another equation, which can be used for describing the flow, is Darcy's semi-empirical law. This widely used equation for fiber mats was originally developed to describe the flow through a sand bed. The fluid flow is proportional to the pressure drop Δp across the sand bed and the bed thickness h

$$v = \frac{\widetilde{R}}{\eta} \cdot \frac{\Delta p}{h} \quad , \tag{2.2}$$

where $\widetilde{R}$ is the hydraulic conductivity of the porous medium, and h is the thickness of the porous medium.

The Darcy equation in its original form is only valid for laminar flow and considers only viscous forces. Inertial forces from a turbulent flow regime are not included. This equation can be used for cake building filtrations with constant pressure cases where mass forces can be neglected. Furthermore, a uniform porosity of the suspension is assumed.

Many researchers used the Darcy equation to describe the filtration of wood fibers. In their investigations, they assume that the thickness is equal to the ratio of the basis weight, B, and the mass concentration c

$$v = \frac{\Delta p K c}{\eta B} = \frac{\Delta p}{\eta B R} \tag{2.3}$$

The permeability K and the mass concentration c are fiber mat properties, which are influenced by the size and geometry of the pad. These parameters, in the form $\frac{1}{Kc}$, refer to a physical property, which is related to the specific filtration resistance, R.

The parameters K and c are independent of fluid, permeable medium, or experimental conditions. The coefficient is an experimentally determined proportionality factor. Therefore, mediums with different network structure can have the same permeability. Hence, some authors related the permeability to certain microstructures of the porous medium, such as porosity, the pore-size distribution, the orientation, and the surface of the particles (Bellani, 2011; Johnson & Jackson, 1987).

In the case of a formed fiber mat at low pressure, the orientation and the surface of the particles can be assumed to be constant. The porosity may not be assumed to be constant because of high compressibility of a wood fiber mat. The transfer of the basic filtration equation from the incompressible case to the compressible case is achieved by using the average of the porosity and the resistance of the inhomogeneous fiber mat.

A common equation for a compressible medium is based on the Hagen-Poiseuille law and is called Carman-Kozeny equation. In this equation, the fluid flow through the porous media is treated as the flow through a series of cylindrical pipes or as capillary flow. The permeability is referred to the porosity, e, and the specific surface area, S_V, by the hydraulic radius, (Ripperger, 2005)

$$K = \frac{e^3}{K_1 \cdot (1-e)^2 \cdot S_v^2} \tag{2.4}$$

The porosity, e, which is defined as the void volume fraction of the total volume, between 0 and 1.The specific surface area, S_V, is the total surface area of a solid fraction per unit of mass or bulk volume. The Kozeny-constant K_l is determined by the geometric shape of the pores, the particle orientation and the pore-size distribution.

In order to express the specific filtration resistance, r, in terms of fiber mat properties, Equation (2.3) and (2.4) can be combined, which results in

$$r = \frac{K_l L(1-e)^2 S_v^2}{Be^3}. \tag{2.5}$$

Although the Carman-Kozeny equation (2.5) is applicable for compressible media, the validity remains doubtful due to the uncertainty of the Kozeny constant (Jackson & James, 1986; Wildfong et al., 2000a). In addition, the Carman-Kozeny equation is applicable only for laminar flow.

In order to overcome this constraint, different expansions were developed in order to describe the flow through a fiber mat.

The Darcy and Kozeny-Carman equations neglect inertial forces, which limit the usability for cases where the Reynolds number, which is defined as

$$Re = \frac{\rho_{fl} \alpha v}{\mu}, \tag{2.6}$$

is less than unity. The parameter ρ_{fl} is the fluid density and α the pore size radius. This is the case in the initial filtration process, where the fiber mat is extremely thin. As a consequence, resistance remains rather low and the filtration velocity is very high. Turbulent effects can also occur. For this reason, the transition between turbulent and laminar flow must be evaluated by the Reynolds number. In order to consider the inertial effect, the Darcy law has been extended by a second term. This extended Darcy equations is called Darcy-Forchheimer equation and was introduced by Forchheimer (1901)

$$\frac{\Delta p}{L} = a \cdot v + b \cdot v^2, \tag{2.7}$$

where a and b are constants which can be determined experimentally. These constants are correlated with specific properties of the microstructure of the fiber mat.

An alternative to this approach was presented by Grace (1953). He developed the relationship between the permeability constant K and the pressure, p, as a power law in the form:

$$r = K\Delta p^{n} \tag{2.8}$$

This equation is not applicable for small stresses. Furthermore, the coefficient K describes no physical entity, because its unit depends on the numerical value of the exponent. A way to avoid this constraints is using the equation of Alles (2000)

$$r = \bar{r_0}\left(1 + \frac{\Delta p}{\Delta p_0}\right)^{n_r} \tag{2.9}$$

Drawing on Tiller and Hsyung (1993), the exponent n_r is called the global compressibility indicator for assessing the compression behavior. For an incompressible medium the exponent remains $n_r = 0$; for a strongly compressible medium the exponent n_r tends to 1. The parameter $\bar{r_0}$ and n_r are determined experimentally. Equation (2.9) is used in multiple investigations to describe the experimental results. The focus of these experiments is to identify changes in the boundary conditions such as fiber mat thickness, suspension composition, and suspension pressure.

Campbell (1947) investigated the filtration behavior of wood fiber mats with a conventional freeness tester. He compared the experimental data of the drainability of the fiber mat with data of an industrial paper machine and concluded that the differences in drainability may be related to the compressibility of the fiber mat.

With his drainage experiments using constant-pressure, Ingmanson (1952, 1953) showed that the average specific filtration resistance increases with increasing pressure drop. He also showed that the basic fiber mat properties could be described by the parameter of the Carman-Kozeny equation (2.5).

The influences of pressure and basis weight on the filtration resistance during the filtration process were investigated in more detail by Wildfong et al. (2000b). In their experiments, they varied the basis weight, the applied pressure and also the fines content of the suspension. The results showed an increasing filtration resistance with increasing fines content.

Herzig et al. (1999) considered thin fiber mats at high flow velocity in their experiments. The results showed a constant pressure loss from approximately 1 g/m^2 to 10 g/m^2 and no variation of pressure loss for flow velocities from 0.22 m/s to 0.68 m/s.

Jong (1999) investigated the filtration resistance for a wide range of layer thicknesses at high flow velocity. He used a test device similar to the test device in this study, but with only two pressure levels. He concluded that a more complex test device would be required in order to fully determine the relationship between pressure loss, flow velocity, and basis weight. He used the Darcy-Forchheimer equation (2.7) to determine the permeability constant of the wire and the fiber mat.

An empirical approach is used by Kalliokoski (2011) similar to equation (2.9). He claims that the measured filtration resistance shows a more curved graph than predicted by the Darcy equation. The solution for this problem was to substitute the exponent of the Darcy equation with an empirical fitting parameter. This approach improved the fitting results significantly.

The investigations discussed above are only a small fraction of published work that is relevant for this study. There are many publications, which deal with the determination of the permeability constant, K. They investigated different dependencies such as pulp types, pulp freeness and temperature. Hubbe (2007) published a comprehensive literature review in which various investigations are discussed. The presented investigations apply different methods to calculate the permeability constant K. Most of these investigations obtain well-fitting results by derivations of the Darcy-law (2.3). The test devices used are mostly similar to a handsheet former and are equipped with an external vacuum source for an individual pressure adjustment. During the course of an experiment, the pressure level remains constant or continuously increases.

The investigation of an industrial filtration is more complicated with regard to the filtration pressure. The pressure in a double wire former can be considered as a profile, which is characterized by significant variations between high and low pressure levels. The effect on the fiber mat is a sequence of compression pulses followed by expansion pulses. The local filtration resistance is determined by this pressure history.

The pressure dependence of the filtration resistance in relation to the pressure history was experimentally investigated by Sayegh et al. (1995). The experimental results are used to create a compression model consisting of a serial dash and damper model, in which a linear transfer function describes the relationship between the mat height and the filtration resistance. Their model includes reversible and irreversible deformation phenomena, which were linked to changes in the filtration resistance. The reversible deformation is proportional to the pressure. The irreversible changes in filtration resistance are proportional to the integral of the pressure over the time. The importance of time was previously described by Ingmanson (1957). He compared the results of a constant-flow filtration experiment with the drainability of a fiber mat in a Fourdrinier-former. As a result, the filtration resistance of the test device was significantly higher than the filtration resistance in the paper machine. He explains this

discrepancy by the differences in filtration time. As observed during the compression test by Ingmanson & Whitney (1954), viscous deformation phenomena lead to a continuous change in filtration resistance. This deformation process phenomenon is typically called “creeping”.

As the literature review shows, the fiber mat, the pressure time and the pressure history are fundamental factors during the flow through, which influence the filtration resistance over time. Because of the retention mechanism, it is difficult to distinguish further between phenomena related to pressure, time, and history under hydrodynamic conditions. For this reason, some authors use the relationship between filtration resistance and compression of the fiber mat in order to describe the pressure and time related changes in the filtration resistance. The requirement to transfer the compression phenomenon to the hydrodynamic phenomenon is a transfer function between mat height and filtration resistance.

Two investigations which deal with this relationship were presented by Ingmanson (1952) and Robertson & Mason (1949). They determined permeability data of sulfite pulp with various degrees of freeness and the concentration of the fiber mat. The specific surface area S_v and the porosity e were then fitted to equation (2.4). As shown in FIGURE 2.5, the fitting results are in good agreement with equation (2.4).

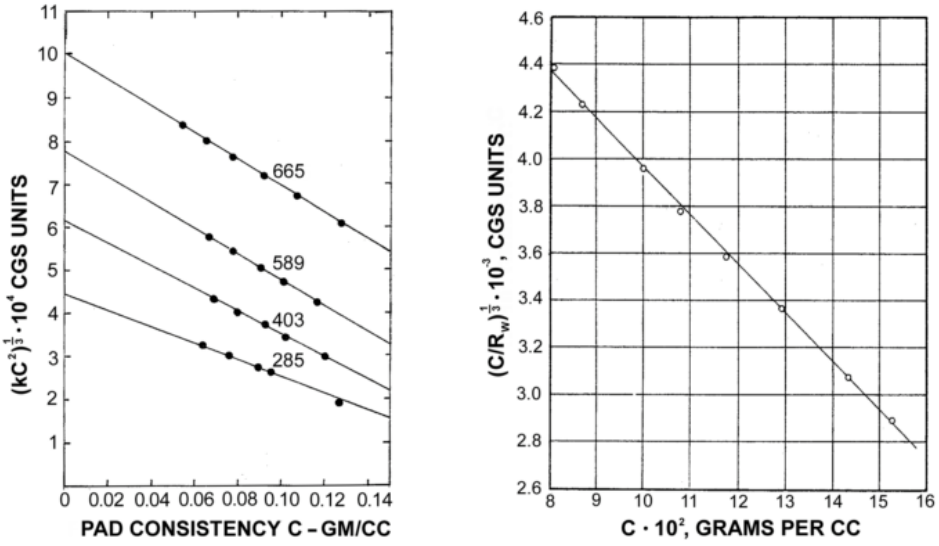

FIGURE 2.5: Linear correlation between the permeability and the pad consistency. Left: experiments at four different freeness levels carried out by Robertson & Mason (1949). Right: Analogical experimental results of Ingmanson (1952).

2.4 Compression of the fiber mat

2.4.1 Network strength

In a diluted suspension with a low solid concentration, the fibers are moving freely and the forces acting between the fibers are quite small. Through the filtration process the concentration increases and the fibers then contact each other, a process in which a fiber network is formed. The flowing medium transfers hydrodynamic drag forces from the fluid to the fibers in the network. These forces of a suspension F_h can be described by Darcy's law. An alternative approach to describe F_h is the use of the hindered settling factor which was used by Batchelor (1972) and Landman et al. (1988). In practice, there are no differences between these approaches (Landman et al., 1988). However, the hydrodynamic drag forces cause compressive and shear forces on the fibers that are then transferred via the contact points from one to another. These compressive and shear forces accumulate through the height of the fiber mat. The accumulation of these forces is the network pressure, p_s. The weight of the fibers is typically low and can be neglected in cases where the wood fiber mat is related to the papermaking process.

Along a defined mat height, dh, the network pressure, dp_s, increases while the fluid pressure, dp_h, decreases with the same rate. This relationship can be described by the following equation,

$$dp_h + dp_s = 0 \tag{2.10}$$

At a defined mat height, the sum of the network pressure and the fluid pressure is the static pressure p, which acts on the top of the fiber network. Mathematically, this can be expressed as

$$p_h + p_s = p \tag{2.11}$$

The lowest network pressure and the highest fluid pressure can be measured at the top of the fiber mat. This concept is based on the Terzaghi principle, which is assumed to be applicable for fibrous networks (Campbell 1947). As already mentioned, and observed by Campbell (1947), the concentration is a function of the network pressure, as shown in equation (2.12). More precisely, the volume concentration increases with increasing network pressure.

$$c_{vol} = f(p_s) \tag{2.12}$$

c_{vol} is calculated by $c_{vol} = V_{solid}/V_{bulk}$, where V_{solid} is the volume of the solid fraction, e.g. the fiber fraction, and V_{bulk} is the volume of the mixture, e.g. the volume of the water and the fiber fraction in a suspension. The concentration can be expressed by the porosity, e.Using this relationship, equation (2.12) can be written as:

$$e = f(p_s) = 1 - \frac{\rho_{bulk}}{\rho_{solid}} \tag{2.13}$$

This equation assumes that the volume, which is not available for the flowing fluid, is constant and no other forces are at work. In the case of a typical compression cell, it can be assumed that the surface of the control volume and solid volume is constant. The porosity can simply be expressed as a function of mat height, h.

The relationship between the porosity and the mat height was investigated by several authors (Boxer, Dodsen, & Sampson, 2001; Campbell, 1947; Ingmanson, 1952; Jones, 1963; Jong, 1998; Kataja & Hirsilä, 2001; Vomhoff, 1998). In most of these investigations, the relationship between the network pressure and concentration is described by a power law similar to equation (2.8). In the work of Jong (1998), the changes in concentration are investigated. For this type of observation, he applied the stress-strain relationship. The porosity, e, and the mat height, h, can be related to the strain, ε, in the following form:

$$h = h_0(1 - \varepsilon) \tag{2.14}$$

$$e = \frac{e_0 - \varepsilon}{1 - \varepsilon} \tag{2.15}$$

where the zero-subscript relates to the initial deformation condition. Equation (2.12) which is typically appropriate for a simple correlation between pressure and concentration, is not suitable for the complex strain behavior of a fiber mat. This requires the application of differentials, which is explained in the next chapter.

2.4.2 Deformation components

At a high volume concentration, the network assumes a high average number of contact points and has the properties of a solid structure (Landman et al., 1988). This means that the hydrodynamic drag forces which act on the fibers can be transferred from one fiber to another. If the hydrodynamic drag forces increase, the compressive forces increase as well, whereby the fiber mat undergoes a compressive strain. In case of an elastic strain, the fiber-fiber connections resist the compressive forces. This

implies that during the expansion process the fiber mat height recovers to the initial value.

If the compression force is further increased, the network structure collapses and fiber-fiber connections at the contact points start to rearrange. New connections are formed, the result of which is a denser network structure. This denser structure has a network pressure, which resists the hydrodynamic drag forces. Through this irreversible deformation, the equilibrium pressure changes. This equilibrium pressure, which is also called compressive yield stress, is a rheological parameter that describes the compression process. It is defined as the stress at which the network structure starts to react plastically. In order to generate a further plastic deformation, it is necessary that the stress on the network structure exceeds the compressive yield stress. The deformation of the network, and thus the matching of the yield stress of the network pressure, happens so fast that the network pressure exceeds the yield stress only for a short period of time. If the network pressure is equal or lower than the yield stress, the fiber mat height keeps constant or, alternatively, the fiber mat expands.

As reported by several authors (e.g. Wilder, 1960; Jong, 1998), the fiber network has a viscous behavior. This means that at constant pressure, the strain increases with time. This behavior is also called "creeping," which can be described by a continuous rearrangement of particles over time.

In his compression experiments under hydrostatic conditions, Wilder (1960) studied the creeping behavior of the fiber mat. He investigated the compression and expansion behavior of the fiber mat at mechanical stress. In order to describe this, he expanded the power-law relationship of Campbell (1947) by a logarithmic term. He observed that a significant deformation of the fiber mat takes place in the first few seconds after the pressure increases. He also found out that a significant difference exists between the initial mat height before the compression and the expanded mat height after the release of the compression stress. This can be traced to a significant viscous deformation component, which does not degenerate to its initial value (hysteresis). This behavior can be observed after every additional compression and expansion process. It took six repetitions with a compression time of 5000s until the irreversible deformation was completed, and the mat height did not change before and after compression.

Similar observations were made by Chen (2014), Bellani (2011) and Ingmanson & Whitney (1954) for hydrodynamic conditions. They determined a linear relationship between solid concentration and time with a logarithmic scale.

Bellani (2011) investigated the velocity field above a fiber mat using particle image velocimetry and measured the fiber mat height. They carried out compression and expansion experiments at different flow velocities and observed an elastic and plastic deformation of the fiber mat. The results showed that the plastic deformation

increases when the flow velocity decreases. This result was not expected. Bellani (2011) assumed that a longer filtration time at lower flow velocity causes a larger viscous deformation. In their velocity field analysis, they determined that the size of the velocity gradient ranges from 4 mm to 8-20 mm depending on the mass of fibers deposited on the wire. Furthermore, the size of the velocity gradient did not change with changing flow velocity, a result which was also not expected. They concluded that, because the velocity gradient corresponds to the fiber length, the potential of the velocity field to rearrange the fiber position increases with decreasing fiber length and the fiber mat is deformed irreversibly.

At shorter compression times, no logarithmic change in fiber mat height was observed. Wilder (1960) assumed that during the initial phase of the compression, the deformation process is more complicated by hydrodynamic drag forces. He concluded that for deformation times less than 40 ms, the creeping effects are only of minor importance. Jones (1963) used the test device of Wilder in order to investigate the compression and expansion process for wood and synthetic fibers. He stated that the compression process below 0.1 sec is dominated by the water removal, and at longer compression times the physical properties of the fibers influence the fiber movement and thus the formation of the network. Adorj´an (1975) and Shirato & Kato (1970) made a similar observation for the drainage of a colloidal suspension (Holmqvist, 2002).

Buscall & White (1987a), Howells et al. (1990), and Landman et al. (1988) investigated the sedimentation of flocculated suspension. They observed that at high concentration the network can resist certain pressures before the network collapse. This means that the network shows an additional elastic behavior. During their experiments, Buscall et al. (1987b) and Channell & Zukoski (1997) observed an elastic behavior and a yield-stress of a flocculated colloidal suspension (Holmqvist, 2004).

As the discussion of different experiments shows, the fiber mat has several rheological properties. These are: elastic, plastic, viscoelastic and viscoplastic deformation components. These are typically modeled in the rheology by series and parallel connections of idealized basic elements. Each element is described mathematically by an equation, which represents the ratio between the stress, σ, and the strain, ε.

Elastic deformation components are modeled by Hooke's law. The characteristic variable of the Hooke's element is the modulus of elasticity, E. Under the assumption of linearity and time independence, the relationship between the stress and the strain is described by

$$\sigma = E\varepsilon \tag{2.16}$$

Newton's damper represents the time dependence of viscous deformation behavior, which can be mathematically expressed as:

$$\dot{\sigma} = \eta\dot{\varepsilon} \quad , \quad \dot{\varepsilon} = \frac{d\varepsilon}{dt} \tag{2.17}$$

This describes the linear relationship between stress and the deformation rate $d\varepsilon/dt$, where η is the viscosity of a Newtonian fluid.

The plastic behavior is described by a St. Venant element. An irreversible deformation happens if a critical threshold stress is exceeded. The mathematical description is

$$\varepsilon = \begin{cases} 0 & \text{for } \sigma < \sigma_v \\ \varepsilon(t) & \text{for } \sigma \geq \sigma_v \end{cases} \tag{2.18}$$

Here σ_v is the threshold stress at which the material starts to flow. The description of the basic elements represents the single idealized behavior of mechanical deformation. For the simulation of the real behavior, the basic elements are combined in consideration of specific coupling rules.

The corresponding literature presents many models, which describe the fiber mat during the compression process. Buscall & White (1987a), Holmqvist (2002), Kataja & Hirsilä (2001) and Landman et al. (1988) modeled the yield stress of the fiber mat depending on the solid concentration of a strongly flocculated suspension. Another approach followed by Bergqvist (1994), Brokate & Sprekels (1996) and Visintin (1991) uses hysteresis operators to describe the deformation behavior and take into account the history of the deformed media. Both approaches are not suitable for incorporation in a complex equation system, which simulate the deformation process in a double wire paper machine. In addition, most of the yield stress models represent only the compression, and not the expansion process. So, they are only suitable for modeling a continuously increasing compression pressure, which is not the case in a paper machine. The use of hysteresis operators in order to describe the compression history of the fiber mat involves the solution of partial differential equations, which is a complex issue with high computational effort (Lobosco, 2004).

Jong (1998) presented a rheology model that consists of a damper and a spring in parallel, which is called Voigt-Model, and added a spring in series and obtained a good agreement with his experimental results. However, it is required to determine the time-dependent modulus for each compressive load, because no general analytical expression has been found yet. The mathematical formulation of the model he used is

$$\left(\frac{1}{E_1}+\frac{1}{E_2}\right)\ \sigma(t)+\frac{\eta}{E_1E_2}\dot{\sigma}(t)=\frac{\eta}{E_1}\dot{\varepsilon}(t) \tag{2.19}$$

Sayegh & Gonzalez (1995) used a spring-damper model for the description of the relationship between pressure and filtration resistance. The relationship between the mat height and the filtration resistance was incorporated by a linear function derived from the Kozeny-Carman equation. In the first approach, they used a Voigt model. This model didn't match the experimental results very well. The reason for this was a continuous increase of the pressure loss at constant flow velocity. A Voigt model cannot represent this behavior, because this model predicts a steady-state value for the filtration resistance. The alternative model they used was a Maxwell model, which is a spring and a damper in series. This model can be expressed by

$$r(p,t)=r_0+\frac{a}{\eta}\int_0^t p(\theta)\,d\,\theta+\frac{a}{G}p(t) \tag{2.20}$$

where r is the local specific filtration resistance, p is the local pressure within the pulp pad, r_0 is the initial local specific filtration resistance, θ is the initial time, a is the proportional factor between the strain γ and the average specific filtration resistance R, and G is the shear modulus.

Another model was presented by Lobosco (2004). In his model, the history is accounted by including the first compression, unloading, and reloading. This simplification limits the validity in case of multiple deformation processes. In equation (2.21) to (2.23) the basic equations of this model are shown.

$$\frac{\sigma_{fc}}{p_r}=\sqrt[N]{c/M} \tag{2.21}$$

$$\sigma_{un}(\epsilon,\epsilon_{min})=\sigma_{fc}(\epsilon_{min})\frac{B-\left(\frac{\epsilon_{min}-\epsilon_0}{\epsilon-\epsilon_0}\right)^{\beta}}{B-1} \tag{2.22}$$

$$\sigma_{re}(\epsilon,\epsilon_{min},\epsilon_{re})=\sigma_{re,0}+\frac{\epsilon_{min}-\epsilon}{\epsilon_{min}-\epsilon_{re}}\left(\sigma_{un}(\epsilon_{re})-\sigma_{re,0}(\epsilon_{re})\right) \tag{2.23}$$

where σ_{fc}, σ_{un} and σ_{re} are the applied pressure and $\epsilon, \epsilon_{min}, \epsilon_{re}$ are the modified strains during compression, unloading, and reloading.

2.5 Model of a double wire

The literature review of former models shows that several investigations dealt with the modeling of the different dewatering components of a former (Dalpke & Green, (1999), Holmqvist (2002), Martinez (1998) and Roshanzamir at al. (2000)). These investigations were assessed with respect to their applicability to the simulation of the suspension dewatering in a double wire former. The following criteria were applied:

- The most relevant physical processes should be included.
- Enable a precise prediction of the pressure difference in the suspension core.
- Create a model of the fiber mat and the suspension core as a continuum.
- Initial and boundary conditions, which describe the dewatering in a double wire former, should be included.

Dalpke & Green (1999) modeled the single side impingement point. Their model uses a force balance including an inertial and viscous term. It is a two-dimensional model, which calculates the shear, the pressures, and the velocity profile along the initial dewatering.

They simulated the influence of jet velocity, jet rush and drag, and drainage resistance. The results showed that inertial and viscous effects should be included in the model. Furthermore, they concluded that the forces of the jet act on the drainage only for a length of the thickness of the jet. The highest drainage rate exists within a length of twice the jet thicknesses. The main parameter influencing drainage is the filtration resistance. The rush and drag setting does not affect the pressure and the drainage significantly.

In the second step, Dalpke & Green (1999) modeled the wedge zone of the roll former. The position of the wire is determined by a force balance. From the simulation results for the predominant part, they received a lower pressure level than it is obtained by P=T/R. They stated that the relationship inside the wedge zone is more complex than this simple equation. However, local pressure peaks exceed the pressure predicted by this relationship.

The simulation results of the impingement point are validated by measurements on a stationary forming wire. The simulation shows satisfying results for the area close to the impingement point and poor results for the succeeding section of the forming roll (FIGURE 2.6). Dalpke & Green (1999) stated that a reasonable explanation for this difference can be erroneous measured values of the drainage at low flow velocity, which is the effect of the flow angle and the roughness of the forming wire on the filtration resistance. The model of Dalpke & Green is two-dimensional. The

computational effort is much higher than for a one-dimensional approach. They also mention that the convergence is only reached for a very narrow operational window.

Holmqvist (2002) presented models of three different former segments. These are models for an unsupported wire and two models for a supported wire for the upper and the lower position. Due to the modular system, several of the former configurations can be built, such as forming blades, suction boxes, and transient regions. The foundations of the model from Holmqvist (2002) are presented by Zhao & Kerekes (1995).

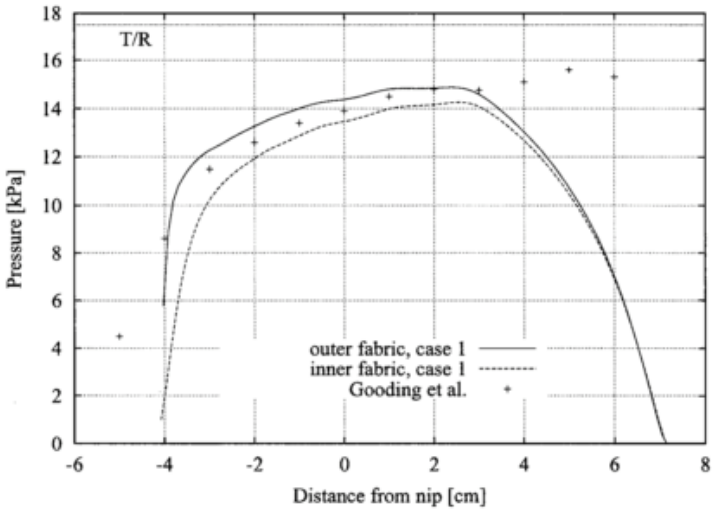

FIGURE 2.6: Pressure distribution along the forming roll of a double wire former. Case 1 presents the computational results of Dalpke & Green. Godding et al. (2001) measured the pressure inside a double wire former. The simulation results are in good agreement with the measurements in the center of the nip. At the boundary area, the simulation results are not satisfying.

The fiber mat and the wire are simulated as a continuum. The fiber mat resistance is modeled as a linear function of basis weight, while no inertial effects are included. The permeability is set constant. Holmqvist (2002) mentions that non-linear behavior could be implemented by determining the permeability constant in dependence of the compression behavior. The continuity equation is a derivation of the Navier-Stokes equation and the suspension is considered to be a Newtonian fluid.

The simulation is done for different boundary conditions such as position, curvature of the blades and load on the blades, the wire tension, and drainage resistance. In general, the model shows a good agreement with the experimental results of Zhao & Kerekes (1995). An example of the accuracy of the blade simulation is

shown in FIGURE 2.7 (left). Holmqvist (2002) concludes that the distance between the blade position induces non-trivial interactions between the pressure pulses. The suction boxes in the opposite position of the blade dampen the amplitude, which is generated by the blade. By analyzing the effect of the curvature of the blade, the simulation shows that the wire is not always in contact with the blade.

One drawback of the model is the generation of oscillating solutions for high values for the initial drainage resistance. Similar results were obtained by the one-dimensional model of Zhao & Kerekes (1995) and the two-dimensional model of Zahrai & Bark (1995). Both have shown that a critical value of the drainage resistance exists when oscillating solutions start to occur. An example of the oscillation tendency is shown in the right subplot of FIGURE 2.7 (right).

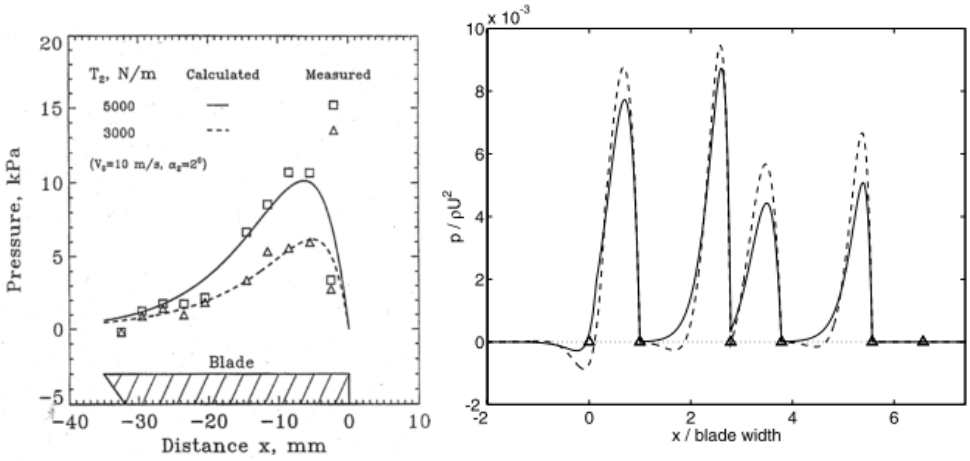

FIGURE 2.7: Left: Validation results of the model of (Zhao & Kerekes, 1995). Simulation conditions: wrap over the trailing edge is 2°; Wire speed 10 m/s. (-) and (□): Wire tension 5 kN/m. Initial gap size 0.8 mm. Estimated drainage resistance 39.5 kNs/m^3. (---) and (Δ): Wire tension 3 kN/m. Initial gap size 1.0 mm. Estimated drainage resistance 23 kNs/m^3. Density 1000 kg/m^3. Right: Simulation results of Holmqvist (2002) for two different values of the initial drainage resistance. The values of the drainage resistance are above the critical value of 67 kNs/m^3. This simulation shows oscillating solutions with high amplitudes for the pressure and regions with a pressure lower than the ambient pressure.

Martinez (1998) developed a physical model to estimate the drainage rate of a double wire roll former. The fiber mat is modeled as a compressible medium, which grows continuously along the forming roll. This is accomplished by using the empirical deformation equation by Ingmanson & Andrews (1959) and the Kozeny-Carmen equation, both of which consider fiber properties such as porosity and specific fiber surface. The pressure distribution within the suspension is determined by

measurements and a force balance, where the force balance considers both, hydrodynamic pressure and centrifugal forces.

Boxer et al. (2001) derived an analytic solution of the model from Martinez (1998). This is accomplished by simplifying the model based on the assumption that the dewatering pressure is constant. The validation was done by experiments at a pilot paper machine. Different machine parameters were tested, such as machine speed, roll vacuum, and wire tension. The results of the experiments agree well with the predicted values. The lowest prediction quality is obtained for a high roll vacuum. A possible reason for this discrepancy can be seen in the method used to determine the initial specific surface are of the fiber, A_{sp}. The total prediction error is about 10%. During the experiments, the pressure profile inside the suspension was measured. An example of the measurements is shown in FIGURE 2.8. This measurement is not used to validate the model. It is used as an input variable. Thus we do not have any information about the simulation quality of the pressure profile.

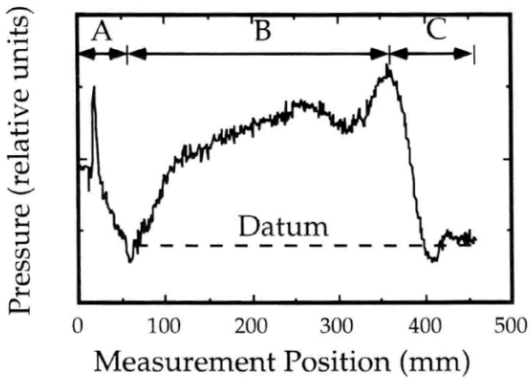

FIGURE 2.8: Pressure distribution within the suspension at the forming roll (Martinez, 1998). The pressure distribution is used as an input parameter for the simulation.

Roshanzamir (2000) developed a simplified one-dimensional and a viscous two-dimensional model considering typical operation parameters, such as wire tension and machine velocity, and parameters which depend on the construction type, such as blade length, curvature, and wrap angle. It is assumed that the suspension behaves like a Newtonian fluid. With his simulation, he shows that the inertia has only a small influence on the amplitude and the length of the pressure pulses. Furthermore, he investigated the effects of doctoring the water on the exterior of the wire, which was primarily introduced by Green & Kerekes (1998). The water is carried at the outside of the wire with a layer thickness of about 0.5 mm. At the point where the water meets the blade (nose radius), a stagnation point is generated (FIGURE 2.9 Left). The water layer is deflected at this point in two directions. Due to the deflection in direction of

the wire, a pressure pulse is induced in the suspension core between the wires. This effect is significant and can increase the pressure pulse by 20 to 30% (FIGURE 2.9, right). The remaining water is deflected parallel to the blade front and is their removed from the wire.

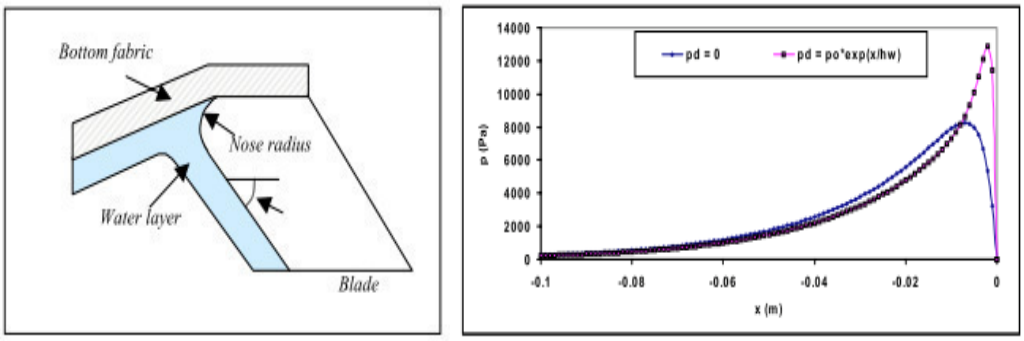

FIGURE 2.9: Simulation of the doctoring effect by a blade. Left: A schematic illustration of the region at a blade where the water is doctored by a blade. Right: Simulation results of Roshanzamir et al., (1999); Small dots: Without doctoring effect; Large dots: With doctoring effect.

2.6 Conclusion

The literature review shows that only a few investigations worked on different deformation phenomena such as elastic, plastic, viscoelastic and viscoplastic deformation and their influences on the flow resistance at low loads. The test devices which are used are either suitable to measure the influence of pressure on the filtration resistance or to measure the influence of pressure on the mat height. With most of the test devices, a simultaneous measurement of flow resistance and mat height is not possible.

The test devices used to measure the filtration resistance are cells at which a suspension is filtered at the surface of a wire. During the filtration process the flow velocity and the pressure drop are measured. The suspension is a mixture of fibers, fillers and water at a solid content between 0.01 and 1%. At this solid content, the suspension is opaque and there is no clear boundary layer between suspension and fiber mat. The measurement of the mat height is not possible, because optical and mechanical distance sensors need a defined boundary layer.

The test devices with which the mat height is measured consist of a vessel filled with a suspension. A piston is moved from the opening on the top down to the bottom. The piston compresses the suspension with a defined pressure and the mat height is measured. With this device, the filtration resistance cannot be measured.

The subject of this work is to experimentally investigate the rheological properties of the fiber mat during compression. For this purpose, a new test device for the investigation of the dynamic compression and recovery process in a fiber mat by measuring the mat height and the flow resistance is developed and validated. This test device enables the simultaneous measurement of the height and the flow resistance of the fiber mat simultaneously under hydrodynamic conditions.

The model, which covers most of the criteria for a double wire former model listed in chapter 2.5, was presented by Holmqvist (2002). This model includes former elements such as suction boxes, or loadable and curved blades. These individual component models can be combined to represent any double wire configuration in the composite model. The simulation results show a good agreement with experimental results for a low filtration resistance. At a high filtration resistance, the system shows physically infeasible oscillations with high amplitudes. An additional limitation of the model is the simplification that the backflow from the outside of the wire must overcome the filtration resistance of the wire and the fiber mat. For the model developed in this work, the equations of Holmquist (2002) are used as a starting point. Some simplifications of Holmquist's model were elaborated and replaced by models with higher accuracy. Following extensions were made:

- Flow-direction-dependent filtration resistance
- Water layer between wire and fiber mat in case of backflow
- Doctoring effects to remove water from the outside of the wire

Chapter 3

3 Development and verification of the test apparatus

3.1 Introduction

Conventional techniques for determining the filtration resistance of a fiber mat are suitable to characterize the influence of basis weight and pressure loss. These techniques are related to a slowly running Fourdrinier former, where smooth dewatering takes place. Phenomena that occur during the laboratory experiments are applied to the industrial environment to analyze the process behavior and deduce operation strategies, in order to optimize the dewatering. For a typical Fourdrinier former, with a machine speed of 800 m/min and a dewatering line of 7 m length, the dewatering process takes approximately 500 ms or longer. In a modern double wire paper machine, the dewatering process is much faster and can take less than 100 ms. Due to this difference in time scale, it is not clear whether the phenomena that influence the dewatering are similar. An investigation which supports this hypothesis was presented by Wilder, (1960). He concluded that significant viscous compressive strain cannot be observed for times smaller than 40ms.

Therefore, in this study an apparatus was designed to represent the dewatering characteristics in a double wire former, as closely as possible. This was accomplished by adding two additional features to the conventional apparatus. First, the sheet forming process and permeability test were decoupled into two separate steps. Since the sheet forming process is completed in the first step and thus the filtration is completed too, the resistance of the formed fiber mat is denoted “flow resistance”. Second, the loading time and the hydrostatic pressure levels could be varied during

the permeability tests by the use of predefined switching sequences. The fiber mats were loaded from 0.6 s up to 45 s at a pressure range from 0.4 to 80 kPa.

This procedure allows a better characterization of the fiber mat and a differentiation of the contribution of steady state and dynamic changes in flow resistance. The literature shows that fiber mats that are loaded with a wide pressure range show elastic, plastic, and viscous behavior. The ratio of these compression components strongly depends on pressure level and time (Wilder, 1960). Therefore, the experimental conditions are defined in a range that is comparable to an industrial dewatering process.

These results were used to develop a simple permeability model, which includes all relevant phenomena to describe the filtration process during double wire dewatering.

3.2 Equipment

In order to characterize the fiber mat behavior under pressure pulses, a drainage tester was designed. The drainage tester has a continuous approach flow system and is suitable for discontinuous flow conditions. During the experiments, the pressure differences and the flow velocities were measured.

As shown in FIGURE 3.1, the permeability cell consists of a transparent cylinder with a diameter of 5.5 cm. A forming wire, which is fixed into an adapter, is installed at the bottom of the cell in order to filter the fiber suspension and to allow the deposition of the fiber mat. Pressure sensors were placed at the positions on the top (P1) and on the bottom (P2). The permeability cell was connected to a reservoir tank for warm and cold water supply. At the outlet of the permeability cell, an ultrasonic flow meter (V) was installed. The valves A, B and C were the control valves to start the permeability test.

The wire was a standard forming wire for graphical paper (FIGURE 3.2). The diameter of the effective wire area was 5.5 cm, which corresponds exactly to the inner diameter of the permeability cell. The wire adapter was designed to support the wire across the complete wire area without a significant increase of the flow resistance of the single adapter. This was accomplished with a bundle of metal tubes with a diameter of 0.8 cm. In the direction of the wire, the tube walls get thinner in order to decrease the contact area between the wire and the tubes. On the top, a coarse metal wire was combined with an industrial forming wire. Both wires were fixed on the tube bundle with a perforated cap. At the bottom, a support ring fixes the adapter centered in the flange.

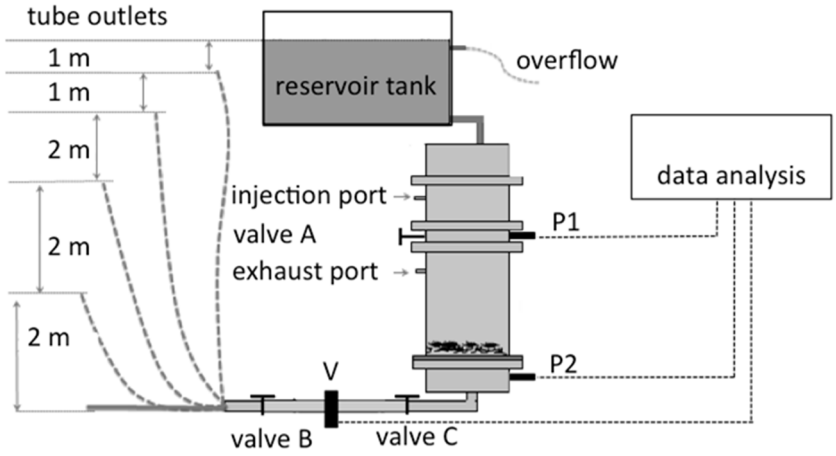

FIGURE 3.1: Schematic description of the compression cell.

The driving force was supplied by the height difference between inlet and outlet. By changing the position of the outlet tube, different hydrostatic pressures could be applied. An overflow out of the receiving tank guaranteed a constant overhead pressure.

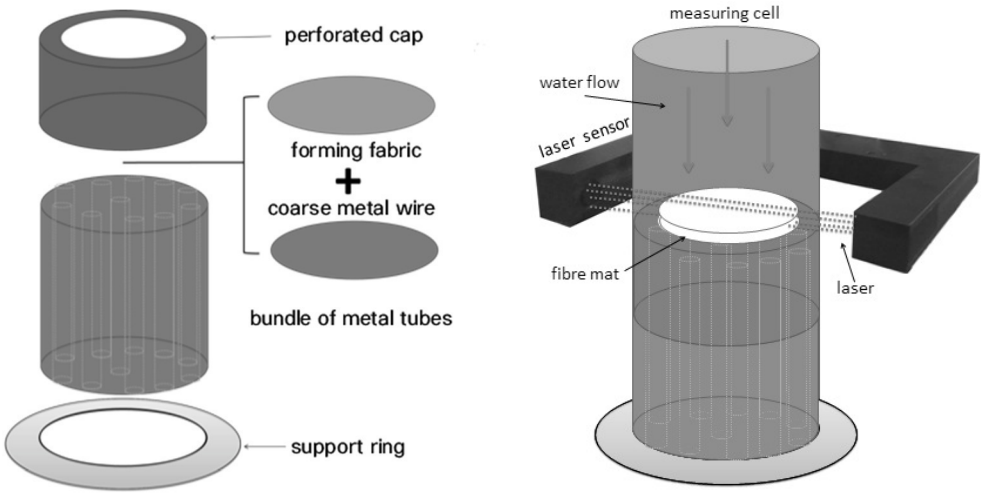

FIGURE 3.2: Schematic description of the wire adapter and measuring cell. (Left) A bundle of small tubes are surrounded by a support tube. On the top, a coarse metal wire is combined with an industrial forming wire. Both wires are fixed on the tube bundle with a perforated cap. (Right) Measuring cell with the laser sensor to measure the fiber mat height.

In other investigations pumps were used to supply the driving force for water flow. However, some authors (Herzig & Johnson, 1999a; Jong, 1998) reported that long stabilization time was necessary to reach steady-state flow conditions. Additionally, depending on the pump type, pressure pulses might disturb the system.

The pressure sensor was a ifm PA 3024 piezoresistive sensor, which was useable for both negative and positive pressure levels. The measurement range was 0-6 bar. The measurement frequency was 1000 Hz with measurement inaccuracy of less than 0.5%. The flow meter was an ultrasonic flow meter with a measurement frequency of 60 Hz (Flowmax 400 i). This sensor was suitable to measure a flow from 1.2 to 120 l/min. The error of measurement was max. +/- 1% of mean +/- 3 mm/s. The reproducibility was $\leq$ 0.5%. The accurate pressure variation during the experiment was guaranteed by fast opening valves A, B and C, shown in FIGURE 3.1. These valves were pneumatic angle valves. The opening time was 250 ms and the closing time was 350 ms.

3.3 Procedure

The fiber suspension was injected into the measurement cell by a syringe through the injection valve. During the injection, there was no flow in the measurement cell and the valves are closed. The injected suspension had a solid concentration of 1% and was diluted down to approximately 0.1% in the measurement cell. By opening the valves A, B, and C, the fiber suspension started flowing and the fibers deposited on the surface of the wire. A fiber mat is formed and the experiment began. After the experiment, the adapter was removed from the measurement cell and the fiber mat sample was withdrawn for the mass determination. The flow velocity, the pressure loss and the mat height were measured during the experiment. The mat height was determined by laser line sensor L-LAS-TB-F-6x1-100 from mu-v (FIGURE 3.2, right). This sensor consisted of a transmitter and a transceiver. The permeability cell was placed in between. While measuring the mat height, it was difficult to obtain reproducible values for the initial mat height. The reason for that was the high compression rates at low pressure losses. Therefore, the initial mat height, h_0, was defined at a pressure loss of 10 kPa. The initial mat height is thus called “modified mat height” in this work. This definition is also applied for parameters which are calculated from the mat height.

The test device was used for two types of trials. In the first procedure, the pressure loss was continuously decreased from 79 to 10 kPa during the expansion process at a basis weight of approximately 40 and 80 g/m^2. This approach was used to determine the relationship between flow resistance, mat height, and pressure loss during the expansion process. In the second procedure, for the analysis of the compression and

recovery, the fiber mat was generated at a low-pressure level. When the sheet forming process was finished, a sequence was initiated in which the valve B was opened and closed. Due to the variation of the tube outlet, different hydrostatic pressures could be set. In the first type, the fiber mat was loaded and unloaded with a pressure pulse of 60s from a pressure loss of 4 kPa up to 79 kPa. Both pressure changes were carried out as a step function. This procedure reflects the compression behavior of a fiber mat during fast pressure changes and it enables the detection of different deformation phenomena.

3.4 Parameters

The fiber suspension was injected into the measurement cell by a syringe at the injection valve. The injected suspension had a solid concentration of 1% and was diluted in the measurement cell to approximately 0.1%. Depending on the dosage amount, the basis weight varies between 40 and 80 g/m^2. By opening the valve A, B, and C, the fiber suspension started to flow and the fibers were deposited on the surface of the wire. A fiber mat was formed and the pulse sequence started. When the trial was finished, the adapter was removed from the measurement cell and the fiber mat sample could be withdrawn in order to determine its mass.

The pulps were prepared by 24hrs of swelling followed by the standard disintegration. The permeability experiments were conducted with recycled DIP fiber pulp (RF) for newsprint paper, bleached softwood kraft pulp (LF) and bleached hardwood eucalyptus pulp (SF). The CSF value for LF pulp was 394 ml, for SF pulp 247 ml, and for the RF pulp 96 ml. The RF pulp contained 16% filler. The compression tests were carried out with LF pulp for a basis weight of 140 g/m^2. The water used in these experiments was tap water at a temperature of 15°C. A complete overview of the experimental parameters used in this study are shown in TABLE 3.1.

TABLE 3.1 Pulp properties of newsprint, corrugated cardboard, and LF cellulose.

Pulp	Pulp type	**Bleached softwood kraft pulp (LF),** 394 ml CSF, fiber length 2.07 mm, fiber width 24 μm, fines content 23%, coarseness 162 mg/m **Bleached hardwood eucalyptus pulp (SF),** 247 ml CSF, fiber length 0.68 mm, fiber width 14 μm, fines content 31%, coarseness 71 mg/m **100% DIP (RF),** 96 ml CSF, 6% ash content, fiber length 0.92 mm, fiber width 17 μm, fines content 45%, coarseness 124 mg/m
	Web basis weight (± 3 g/m^2)	40 and 80 g/m^2
	Temperature (± 3°C)	13°C
Compression	Peak stress (± 3 kPa)	20, 40, 60 and 80 kPa
	Pulse length	0.35 s, 1 s, 2 s, 10 s and 40 s
Expansion	Peak stress (± 0.2 kPa)	3 kPa

(All experiments were duplicated)

3.5 Validation of the method

The validation of the apparatus was carried out in a master thesis by Chen (2014) as a part of this work. The objective of the thesis was the optimization and verification of the apparatus and the investigation of the influence of basis weight and hydrostatic pressure on the flow velocity. The results are in good agreement with the investigation of Jong (1998), who used a similar apparatus.

3.5.1 Wire and apparatus

During the start-up of the test device, the validity of the experimental results was controlled by the measurement of the flow resistance of the wire without a fiber mat. FIGURE 3.3 shows the result of the pressure loss versus the flow velocity through the forming wire. As expected, the characteristic can be described by the Forchheimer equation.

$$\Delta p_{adapter} = 1.797 * 10^4 * v^2 + 3400 * v \quad (3.1)$$

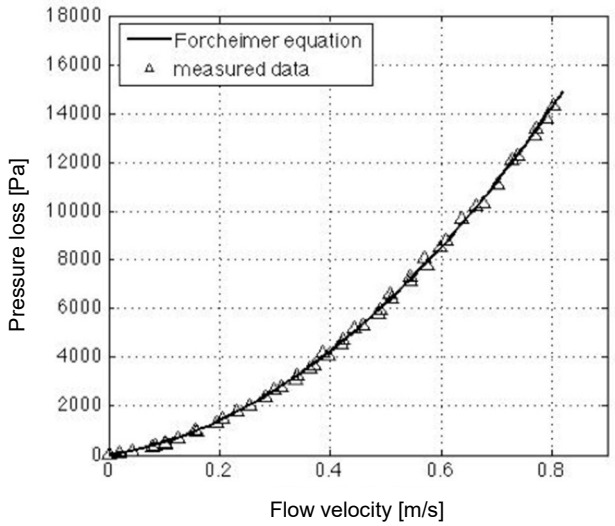

FIGURE 3.3: Flow velocity versus pressure loss across the forming wire. The measured data fits well to the Forchheimer equation (Chen, 2014).

As shown in FIGURE 3.3, at a flow velocity of 0.8 m/s the pressure loss through the forming wire was approximately 14 kPa. The corresponding hydrostatic pressure was 80 kPa. Consequently, the pressure loss through the apparatus was 66 kPa. Generally said, the derivative of the pressure loss with respect to flow velocity decreases with lower flow velocity. In order to reduce the pressure variation during the experiments, the flow velocity range should be limited. Hence in a preliminary study, the influence of basis weight on the pressure loss of the apparatus and flow velocity was determined. The results for a LF pulp are shown in FIGURE 3.4. The figure shows that up to a basis weight of 80 g/m^2 significant changes in pressure loss occur. Above this level, the changes in pressure loss are less than 7% of the hydrostatic pressure. This means that, with a fiber mat at 80 g/m^2, the calculation error is less than 7%.

The same experimental procedure was carried out for SF pulp and recovered fiber pulps (Chen, 2014). The results show that SF pulp at 80 g/m^2 and recovered fibers at 40 g/m are the optimum basis weight values.

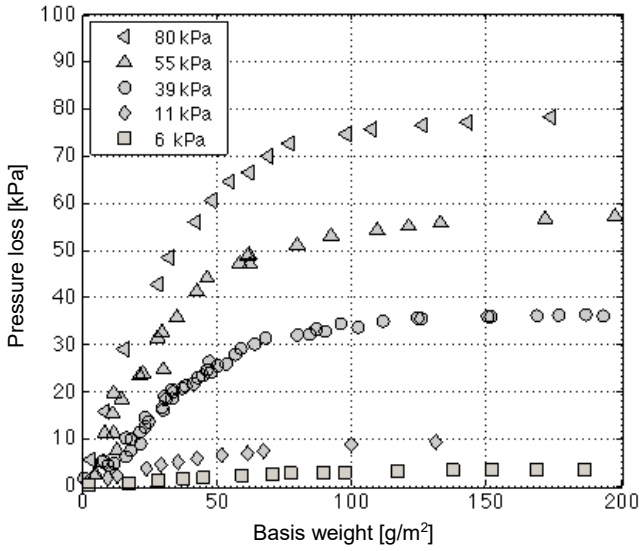

FIGURE 3.4: Pressure loss vs basis weight for LF pulp. The graph shows the optimal basis weight at which the pressure loss is nearly constant (Chen, 2014).

The temperature of the approach flow was constant at 13 °C in this investigation. Pires et al. (1989) analyzed the influence of the suspension temperature between 15-45 °C on the specific flow resistance. The results show that the temperature has no influence on the specific flow resistance. They trace back this observation to the fact that the lower viscosity at a higher temperature is compensated by a higher flow velocity.

3.5.2 Sheet forming

At 80 g/m^2 and 40 g/m^2, respectively, a uniform distribution of fibers at the surface of the wire was attained. At lower basis weights, large areas of fiber-free wire surfaces were apparent. At higher basis weights, a significantly inhomogeneous fiber mat is formed. An indication of the homogeneity of the fiber mat was the repeatability of the experiments. FIGURE 3.5 shows the relationship between pressure loss and flow velocity for three separate tests with the same dosage of suspension volume. The figure shows almost overlapping results. The flow velocity varies in between 0.05 and 0.14 m/s. The variation of the basis weight at a constant dosage amount is smaller than ±2 g/m^2 for a mean basis weight of 80 g/m^2.

The specific flow resistance is calculated by equation (3.3). The determination of the basis weight contains errors, whereby the deviation of R increases significantly up

to 10%, as shown in FIGURE 3.6. Consequently, all experiments were carried out twice.

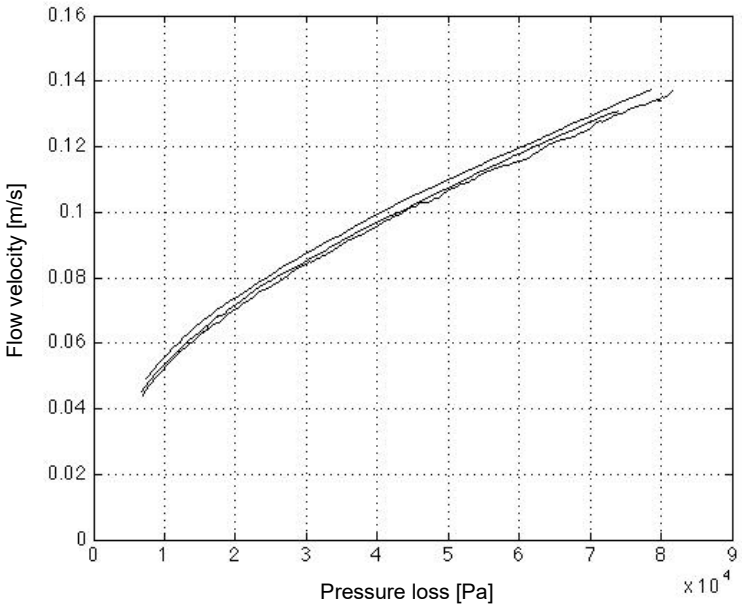

FIGURE 3.5: Flow velocity as a function of pressure for LF pulp at 80 g/m^2. The experiment was carried out three times at the same conditions. The experiments show a good repeatability. The variation of the basis weight at a constant dosage amount is smaller than ±2 g/m^2 at a mean basis weight of 80 g/m^2.

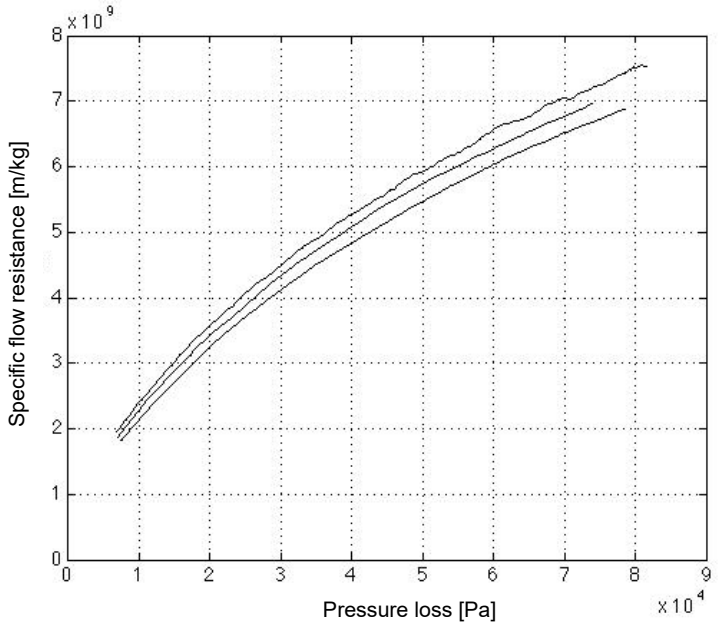

FIGURE 3.6: R as a function of pressure loss for LF pulp. The experiment was carried out three times at the same conditions. Differences in basis weight lead to increased variations up to 10%.

3.5.3 Retention

For the test apparatus, an industrial forming wire was used. A typical total retention level at a paper machine ranges between 50% and 90%. The retention level for fines and fillers is usually between 10% and 40%. This level depends mainly on the flow rate and the particle size distribution. For this reason, the forming process was conducted under constant hydrostatic pressure. When the forming process was completed, pure water was passed through the fiber mat. During this period, it was assumed that small particles were washed out continuously. This means that the basis weight was probably not constant during the experiment, which especially affects the flow rate and the flow resistance, respectively. However, as could be shown in additional experiments, this effect is not significant (FIGURE 3.7). In these experiments, a fiber suspension of LF pulp was filtered by using the suspension twice. In the first test, the fiber fines should be washed out and the fiber size should be narrowed down to only long fibers. This procedure ensures very high fiber retention. The flow resistance test was conducted with the original suspension and with the filtered suspension. The flow resistance measurements of the two suspensions show almost overlapping results.

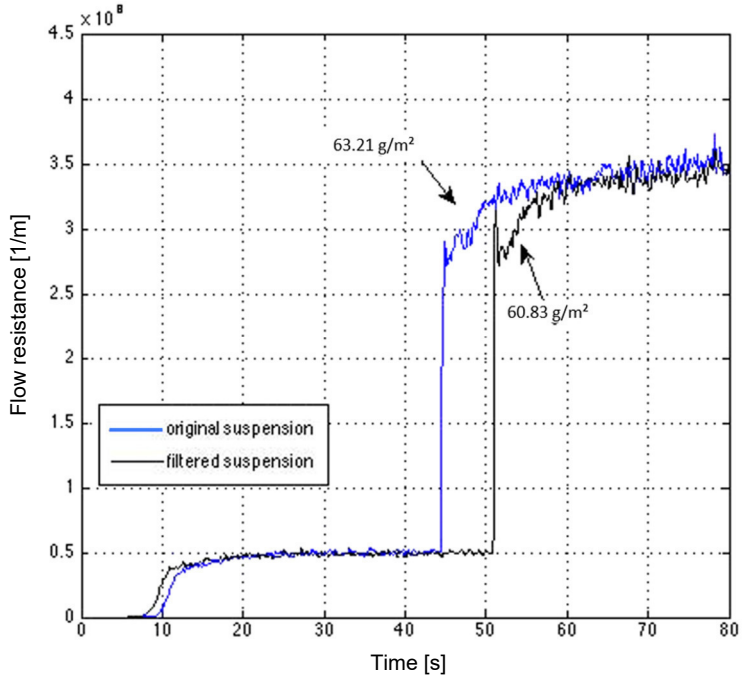

FIGURE 3.7: Flow resistance versus time for LF pulp. For the tests, the original suspension with fiber fines and the filtered suspension with a reduced amount of fiber fines was used.

Since the recovered fiber suspension includes also fillers and a shorter fiber fraction, a higher loss of fibers fines and fillers is highly likely. In the following section, a theoretical analysis is done which addresses the influence of retention effects on the experimental results.

FIGURE 3.8 shows the result when tap water flows through the fiber mat. Accordingly, a continuous decrease of the flow velocity over time can be detected. Assuming a strong loss of fibers during the experiment, an increasing flow rate would be expected. Obviously, there are other effects that are dominant, and it is assumed that the loss of fibers during the experiments is not significant.

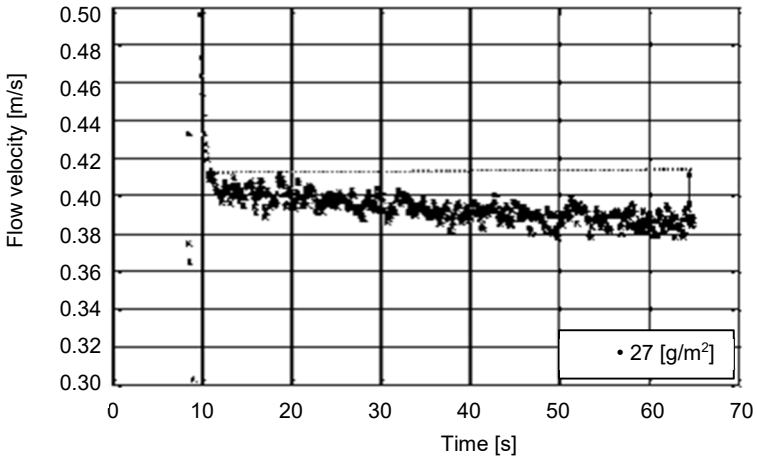

FIGURE 3.8: Flow velocity versus time. The measurements show a monotonic decreasing flow velocity between 10s and 60s.

This assumption is further supported by the fact that the influence of fines on the flow resistance is much higher than the compression of the fiber mat. Therefore, small changes in the fines content of the mat would affect the flow resistance significantly, which would result in an increasing flow velocity between the initial state and the final state (Wildfong et al., 2000b).

3.6 Evaluation

One objective of this work is to develop a simple model to predict the local flow velocity during the compression and recovery process. For this purpose, the following simplifications and assumption are made.

- Neglection of inertial effects.
- Validity of Darcy's law.
- Applicability of Terzaghi's principle.
- Complete saturation of the web.
- Neglection of shear forces
- Constant water velocity across the web thickness.
- Neglection of retention effects

3.6.1 Fiber mat compression

A widely used assumption is that pressure-dependent changes in flow resistance are caused by changes in mat height. However, the relationship between the flow resistance and mat height is not known a priori. Wildfong et al. (2000b) assumed that rearrangements of small particles cause a plugging of pores, leading to a higher flow resistance. From a theoretical point of view, this effect does not necessarily cause changes in mat height. Therefore, this assumption was examined in a preliminary investigation by Flitsch et al. (2016). In this work, the influence of a pressure pulse on the fiber mat height and the specific flow resistance was shown experimentally. The experiments were carried out with the same apparatus developed in this work. The apparatus was equipped with a laser line senor in order to measure the dynamic changes in mat height. Simultaneously, the pressure loss and the flow velocity were recorded. More details of the equipment and the procedure are shown in the work of Flitsch et al. (2016).

Some of the measurement results of this work are presented in FIGURE 3.9, where the subfigures a), b) and c) show the pressure loss, the specific flow resistance, and the mat height during compression, respectively. During this trial, three different processes can be distinguished: sheet formation, compression/creeping, and expansion. The pressure loss during the sheet creation and expansion process is 4 kPa. During the compression process the hydrostatic pressure is increased up to 80 kPa.

FIGURE 3.9 shows that an increase of hydrostatic pressure apparently causes a fast and significant decrease in mat thickness and a significant increase in compressive strain. This behavior indicates that a significant change of deformation is caused by pure plastic, pure elastic or at least very fast viscous deformation. This process is followed by a continuous and slow decrease in mat thickness during the following compression process. This behavior, which is often called creeping, is time-dependent. If the load is removed after about 190 s, the mat thickness increases and reaches a constant value immediately after the unloading. Jong (1998) observed a spontaneous viscoelastic deformation. This conflict relates to the hypothesis that the reversible viscous deformation does not occur at this pressure level, or only at such a small scale that its existence cannot be verified. However, the thickness after the expansion process is much smaller than the mat thickness during the sheet creation process. In summary, during the compression and expansion process, this investigation detected the following deformation phenomena:

- Pure elastic deformation (time-independent reversible deformation)
- Pure plastic deformation (time-independent irreversible deformation)
- Viscoelastic deformation (time-dependent reversible deformation)
- Viscoplastic deformation (time-dependent irreversible deformation)

In the case of time-dependent deformation, it is not known a priori whether the deformation is viscoelastic or viscoplastic. It is also unclear why the time-dependent deformation under compression does not exhibit a time-dependent recovery during the expansion process. After water hammer (hydraulic shock) of 1 kPa, the flow resistance and the mat height are constant. As a possible explanation, the creeping is strongly pressure-dependent and does not occur at a pressure level of 4 kPa for LF pulp. If the pressure in the initial and expansion state is higher, it must be assumed that the creeping effect disappears. The mat height would initially increase, and after some time, it would decrease again slightly due to creeping.

In the literature, the fiber mat is often described as a viscoelastic material which shows an asymptotic increase of mat height during the expansion process and a decrease of mat height during the compression process. This behavior is observed when the pressure is decreased to zero. FIGURE 3.10 shows the results of an experimental results that demonstrate this. The pressure was released 10 times for 30s. At point 1 in FIGURE 3.10 (at an individual expansion phase), the fiber mat shows a high expansion rate in the beginning, which declines steadily. Another phenomenon is the monotonic decrease of the maximum mat height over the expansion phases during the observed 500s. Every compression leads to a monotonic decrease of mat height in the expanded state. This phenomenon is related to a long-time viscous deformation.

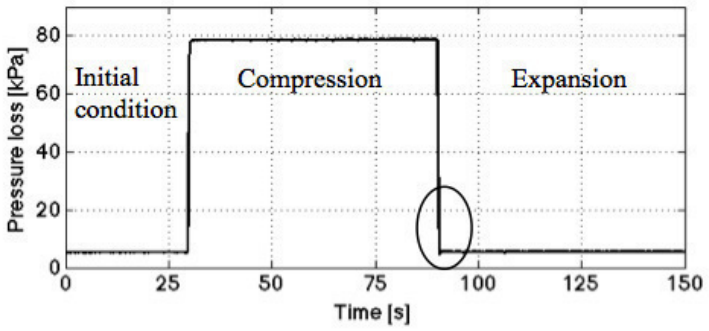

(a)

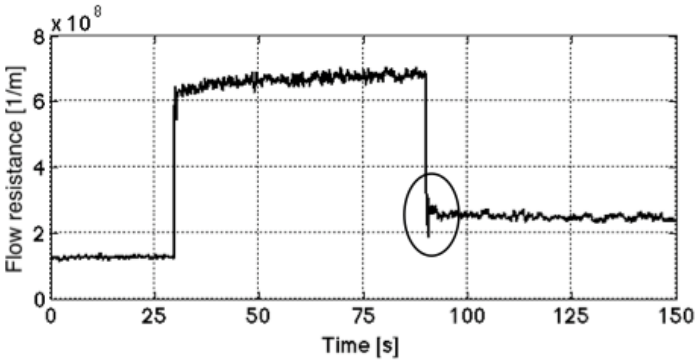

(b)

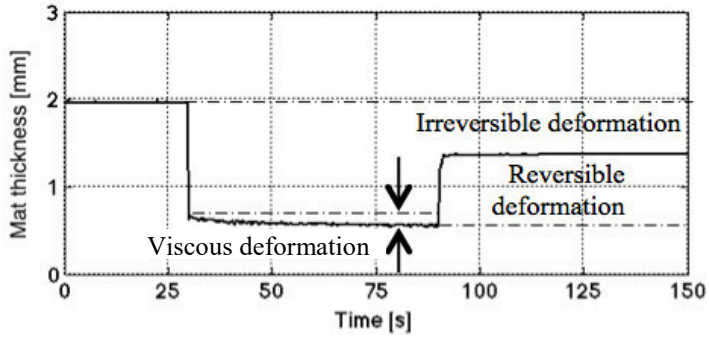

(c)

FIGURE 3.9: Influence of a pressure pulse. Pressure loss (a), flow resistance (b), and mat thickness (c) versus time; due to the increase in pressure loss, the flow resistance increases and the mat height gets compacted. After the loading, the fiber mat shows an irreversible deformation.

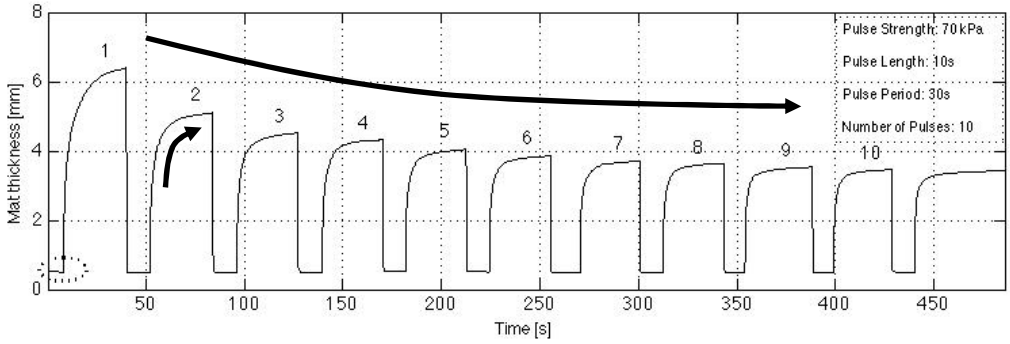

FIGURE 3.10: Mat height versus time for LF pulp. The fiber mat is built up at time zero. During the experiment, the pressure was removed 10 times with an expansion phase of 30s. The fiber mat height shows a viscous recovery during one expansion phase along with a continuous, irreversible decrease of maximum mat height over the entire experiment.

In order to determine the quantitative relationship between mat thickness and flow resistance, additional experiments were performed. A strongly compressed fiber mat was unloaded slowly while, simultaneously, the mat height, the flow velocity, and the pressure drop were recorded. The results are shown in FIGURE 3.11 for LF, SF, and recovered fiber pulp. The compressive strain, ε, was calculated by $\varepsilon = (h - h_0)/h_0$, where h is the final height and h_0 is the initial height. Because of an unreliable measurement of the initial height, a new initial height, $h_{0,m}$, is defined at 10 kPa. This procedure leads to a strain up to 0.6. If the original sedimentation height would be used to calculate the compressive strain, the strain values would be significantly lower. Using the experimental results, a mat height for LF pulp of approximately 2 mm can be estimated. This magnitude of initial height values leads to strain values up to approximately 0.18. The results of the experiments show a linear relationship between modified compressive strain and flow resistance. In contrary to that, the Kozeny-Carman equation shows a non-linear relationship for a wide range of strain. The discrepancy between both results can be explained by two different types of strain. In the experiments of this work, the changes in compressive strain remain insignificant and so, the relationship can be considered linear. In this context, we will therefore apply a linear approximation to describe the relation between specific flow resistance and compressive strain, as shown in FIGURE 3.11. A similar approach is presented by Sayegh & Gonzalez (1995).

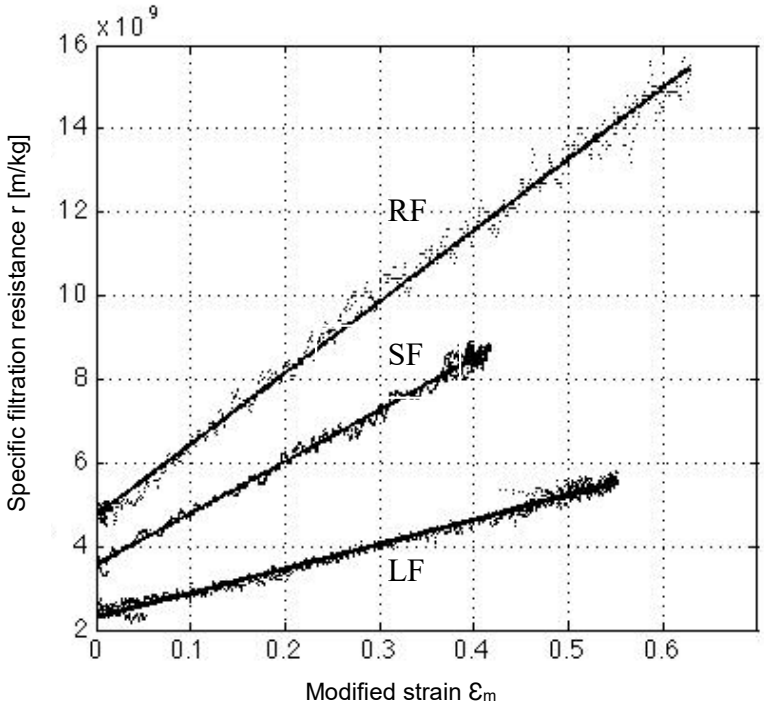

FIGURE 3.11: Linear correlation between specific flow resistance and strain for LF pulp. A linear function of y=a*x+b was fitted to the experimental data, where y is the specific filtration resistance and x is the modified strain. The parameters a and b are fitting parameter. The parameters for LF pulp are a=6E+09 and b=2E+09; the parameters for SF pulp are a=1E+10 and b=4E+09; the parameters for recovered fibers are a=2E+10 and b=5E+09;

The linear relationship between flow resistance and modified compressive strain link the compression behavior to the hydrodynamic flow properties of a fiber mat. This observation shall now be analyzed from a theoretical point of view. The flow through a fiber mat is typically described by Darcy's law shown in equation (3.2). It shows the relationship between the flow rate, $\dot{V}$, and the pressure loss through the fiber mat, ΔP, according to the equation:

$$\dot{V} = \frac{K_D}{\eta}\frac{\Delta p\, A}{L} \tag{3.2}$$

where K_D is the Darcy coefficient, η is the dynamic viscosity, L is the mat height, and A is the mat area. The mat height L can be expressed in terms of the mass per unit area W in the form $L = W/c_m$, where c_m is the mass concentration and W is the basis

weight. Substituting the definition of L into (3.2), and dividing the flow rate by the mat area, A, the expression $\frac{1}{K_D c_m}$ is obtained, which defines the specific flow resistance r [m/kg]:

$$\frac{1}{K_D c} = \frac{\Delta pv}{\eta W} = r \tag{3.3}$$

The coefficient K_D can be related to the following two fiber mat properties: porosity and specific surface area. A widely used semi-empirical equation that which considers these properties was introduced by Kozeny in the following form:

$$K_D = \frac{1}{K_l S_V^2} \frac{e^3}{(1-e)^2} \tag{3.4}$$

According to the description of this equation, the flow resistance depends on the following three parameters: the porosity, e, which is defined as the fraction of the void volume of the total volume; the specific surface area, S_V, which is the total surface area of a material per unit of mass or bulk volume; and the Kozeny-constant, K_l, which is determined by the geometric shape of the pores, the particle orientation, and the pore-size distribution.

The relationship between strain ε and specific flow resistance is calculated by inserting equation (3.3) into equation (3.4) and substituting the fiber mat height, $L = L_0\,(1-\varepsilon)$, and the porosity, $e = (e_0 - \varepsilon)/(1-\varepsilon)$, where the subscript 0 refers to the initial deformation condition. This relationship is shown in equation (3.5).

$$r = r_0 \frac{\left(\frac{e-\varepsilon}{1-\varepsilon}\right)^3}{\left(1-\frac{e-\varepsilon}{1-\varepsilon}\right)^2} \tag{3.5}$$

This equation can be approximated by a linear function in following expression:

$$r \approx r_0 + z\varepsilon, \tag{3.6}$$

where z is a parameter which is determined experimentally. A similar procedure is presented by Sayegh & Gonzalez (1995).

The flow of water transfers hydrodynamic drag forces between the fluid and the fibers. These forces F_h can be related to the pressure loss by Darcy's law. The hydrodynamic drag forces apply compressive forces to the particle, which are transferred via the contact points from one particle to another. At the contact points, compression takes place. These local forces accumulate through the height of the fiber mat. The sum of local forces along a certain mat height is the network pressure, p_s (Martinez, 1998).

For a compressible fiber mat, the relative solid content increases with increasing network pressure p_s. This relationship is typically described by a power law which was first presented by Campbell (1947).

$$c_m = a_c {p_s}^{b_c} \tag{3.7}$$

where c_m is defined by $c_m = m_m/(AL)$ and a_c and b_c are parameters which must be determined experimentally and m_m is the mass of the fiber mat.

The fiber mat height can be related to compressive strain

$$\varepsilon = (L - L_0)/L_0 \tag{3.8}$$

if it is assumed that the fibers do not deform and the volume of the solid fraction is constant. Substituting the concentration in equation (3.7) by the compressive strain, the following equation is obtained:

$$\varepsilon = a_\varepsilon {p_s}^{b_\varepsilon} \tag{3.9}$$

This equation can be related to the specific flow resistance. Provided that the relationship shown in equation (3.6) is valid for the pressure level used in this work, (3.9) can be rewritten as

$$r \approx r_0 + a_r {p_s}^{b_r} \tag{3.10}$$

3.6.2 Repeated compression

In the first approach, which is called continuous loading, the influence of pulse length on the changes in flow resistance was investigated by using a newly built fiber mat for each single pulse length. The results show a strong variation in repeated trials. The reason for this variation was probably the inaccurate determination of the basis weight. Therefore, a new approach was used to investigate the influence of pulse length, which is called discontinuous loading. The pulse length experiments were

carried out by creating a fiber mat and loading it with several pulses with an increasing pulse length. Between the pulses, the fiber mat is loaded with the initial pressure level for 5 s. A schematic description of the procedure is shown in FIGURE 3.12.

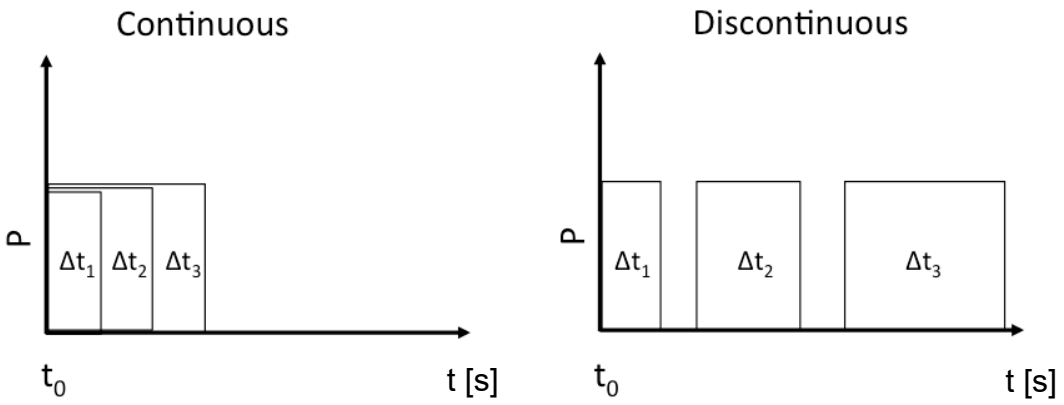

FIGURE 3.12: Schematic description of continuous and discontinuous loading for the repeated compression tests.

The assessment of the experimental results is done by the following approach: For calculating the specific flow resistance the local flow velocity $v_{loc,i}$ is used, where the flow velocity $v_{loc,i}$ is defined as

$$v_{loc,i} = v(t_i) \tag{3.11}$$

$$t_i = \sum_{k=0.6}^{i} \Delta t_k \quad \Delta t = \{0.6, 1, 2, 4, 10, 30, 45\} \tag{3.12}$$

The control variable Δt is the successive term of the pulse length series and i is the index for the number of investigated pulse lengths.

This approach significantly improves the repeatability of the results. To show the validity of this approach, experiments were carried out to investigate whether the repeated compression and expansion has an additional effect on the deformation compared to a continuous loading with a single compression and expansion. FIGURE 3.14 shows two experiments. In the first experiment, the fiber mat was loaded with six pressure pulses of a length of 10 s each. From the 1st to the 3rd pulse, the load is sequentially increased, and from the 4th to 6th pulse the load is constant at a level of 70 kPa. A schematic description of the procedure is shown in FIGURE 3.13.

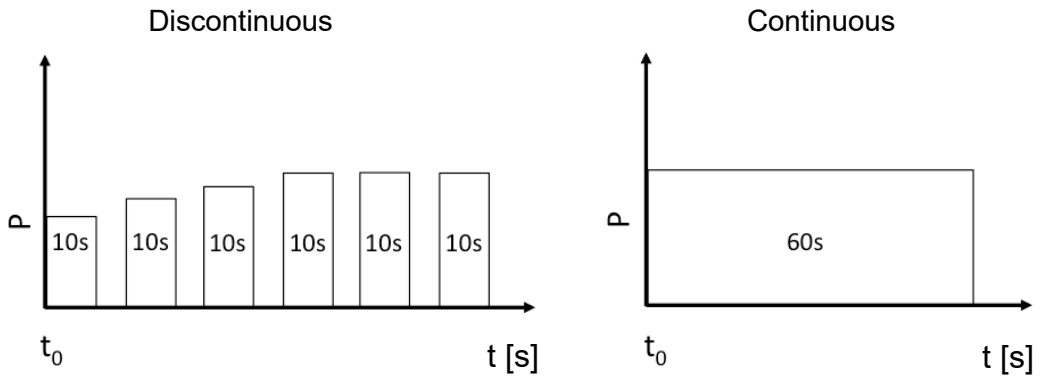

FIGURE 3.13: Schematic description of continuous and discontinuous loading for the compression test shown in FIGURE 3.14.

Here the single pulse lengths sum up to 60s. In the second experiment, the fiber mat was loaded only once at a level of 70 kPa and for 60s. The fact that the expansion curves of both experiments are similar implies that the change in flow resistance during a certain time interval can simply be integrated. As a consequence, the history of the compression and expansion cycles has no influence. Mathematically, this means, if

$$t = t_{cont} = t_{disc,n} = \sum_{k=1}^{n} \Delta t_k \tag{3.13}$$

where t_{cont} is the time with which the fiber mat is loaded during the continuous procedure and $t_{disc,n}$ is the sum of every single pulse length, then

$$r_{cont}(t) \sim r_{disc,n}(t), \tag{3.14}$$

where r_{cont} is the specific flow resistance calculated by results of continuous loading experiments and $r_{disc,n}$ is calculated by the results of discontinuous loading experiments.

This result is only valid for the pressure ranges used in this work. At a lower pressure, a different behavior might be observed because other deformation mechanisms can become dominant. The initial pressure level was at 0.4 kPa.

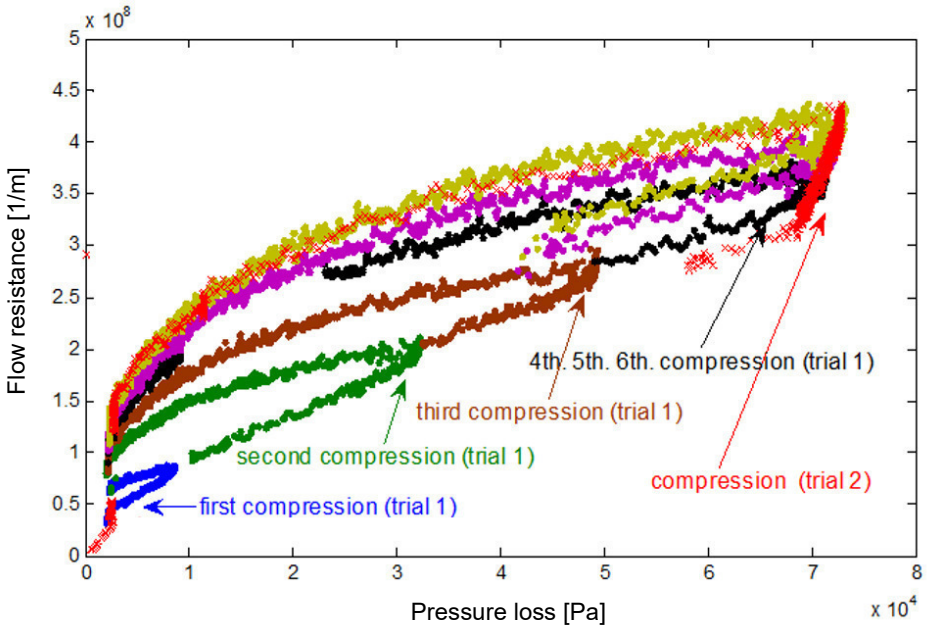

FIGURE 3.14: Pressure loss versus flow resistance of LF pulp during the compression and expansion processes. The red curves show an experiment with one continuous loading. The remaining colored lines show an experiment with several compressions and with increasing pressure. The total loading time remained the same for both experiments. The initial compression at both experiments was at 4 kPa.

3.6.3 Evaluation method of experimental results

The experimental procedure to evaluate different deformation phenomena is executed by varying the hydrostatic pressure during the thickening process of a formed fiber mat. FIGURE 3.15 (left) shows a typical measurement result of a compression sequence. The initial pressure, p_{ini}, is defined as reference pressure and is constant at 0.4 kPa for all experiments. At this pressure level, the fiber mat is formed. When the formation process is completed, the pressure remains constant for another 10 s. In FIGURE 3.15 the preprocessing sequence of 10s is not shown and the time axis is rescaled. Thereafter, the pressure is increased to p_{comp} and remains constant for 350 ms, where p_{comp} is the pressure during the compression state. After the compression process, the initial pressure level p_{ini} of 0.4 kPa is applied again, whereby $p_{exp} = p_{ini}$ which is the pressure at the expanded state of the fiber mat.

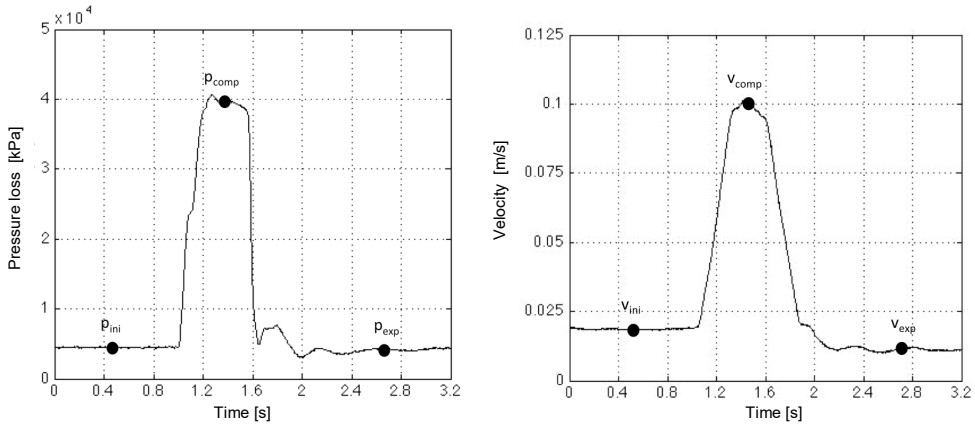

FIGURE 3.15: Typical experimental results for pressure loss (left) and flow velocity (right) of a pressure pulse. The experiment starts at a pressure level of p_{ini}. After the pressure pulse of p_{comp}, pressure p_{exp} is reached. For all experiments $p_{ini} = p_{exp}$.

The velocity recorded during the experiment is shown in FIGURE 3.15 (right). The figure shows that the basic characteristic is similar to the graph of the pressure measurement. At the initial state, the flow velocity is defined as v_{ini}, which is the reference velocity. At the compression and expanded state, the velocity is denoted v_{comp} and v_{exp}, respectively.

The analysis of the experiments is carried out on results at which the parameters reach steady-state condition. The dynamic changes in flow resistance cannot be evaluated, because the measurement frequency of the flowmeter is too low to capture the sharp flank of the step function. This also explains the constant slope during the increase of flow velocity between 1.1s and 1.3s at FIGURE 3.15 (right).

The objective of this experiment is to compare the changes between specific flow resistance in the initial state to the specific flow resistance at the compression and expanded state. Considering the dynamic viscosity, η, as well as the basis weight, W, the specific flow resistance, r_i, can be calculated at various experimental condition.

$$r_i = \frac{\Delta p_i}{\eta\, v_i W}; \quad i = ini, comp, exp \tag{3.15}$$

In the following, the mathematical procedures to calculate the changes in specific flow resistance are explained. There are two different types of experiments. First, the pressure-dependent compression, and second, the time-dependent compression. In both cases, the changes in specific flow resistance are defined as Δr, with the subscript ,pdc, for pressure-dependent compression and tdc, for time-dependent compression.

Pressure-dependent compression and time-dependent compression

The changes in specific flow resistance that result from the variation of the pressure level are expressed as $\Delta r_{pdc}(p_i)$ where $p \in \{37\ kPa, 56\ kPa, 70\ kPa, 85\ kPa\}$. The function $\Delta r_{pdc}(p_i)$ can be determined by using values at the time, t_{ini}, and, t_{comp},. This relationship can be mathematically expressed by

$$\Delta r_{pdc}(p_i) = \frac{r_{ini} - r_{comp}(p_i)}{r_{ini}} \tag{3.16}$$

The time-dependent compression function $\Delta r_{tdc}(t_k)$ is determined by the changes of the flow resistance, r, at the pulse lengths, t_k, where $t_k \in \{0.6s, 1.6s, 3.6s, 7.6s, 17.6s, 47.6s, 92.6s\}$. This function is calculated by subtracting r_{ini} from r_{comp} and dividing the result by r_{ini}, as is shown in equation (3.17). Due to the dynamics of the process, the values for r are the mean values of 300 ms at the time $t_k \in \{0.6s, 1.6s, 3.6s, 7.6s, 17.6s, 47.6s, 92.6s\}$.

$$\Delta r_{tdc}(t_k) = \frac{r_{ini} - r_{comp}(t_k)}{r_{ini}} \tag{3.17}$$

Pressure dependent expansion and time dependent expansion

The influence of a pressure pulse on the pressure-dependent changes for a specific flow resistance in the expansion state is analyzed. These trials are called pressure-dependent expansion with the subscript "pde". The function $\Delta r_{pde}(p_i)$ describes the contribution of the plastic changes for a specific flow resistance. The contribution can be determined by subtracting r_{ini} from r_{exp} and dividing it by r_{ini} at different pressure levels p_i where $i \in \{37\ kPa, 56\ kPa, 70\ kPa, 85\ kPa\}$ as shown in equation (3.18).

$$\Delta r_{pde}(p_i) = \frac{r_{ini,P_i} - r_{exp}(p_i)}{r_{ini,P_i}} \tag{3.18}$$

Additional experiments were carried out to observe the expansion process during a monotonic decrease of the hydrostatic pressure. The purpose of these experiments was to validate the power-law relationship between pressure loss and r, which is shown in equation (2.8.).

The time-dependent change in specific flow resistance was analyzed by the variation of the pressure pulse length. The function of the time-dependent change in specific flow resistance $\Delta r_{tde}(t_k)$ is determined by

$$\Delta r_{tde}(t_k) = \frac{r_{ini} - r_{exp}(t_k)}{r_{ini}} \tag{3.19}$$

Time-dependent and time-independent changes in specific flow resistance

As shown in the experiments of Chen (2014) and Jong (1998), the flow resistance after a monotonic pressure increase, shows a time-independent response (e.g. pure elastic and pure plastic changes) and a time-dependent response (e.g. viscoelastic and viscoplastic changes). To assess the contribution of the time dependent and time independent changes for a monotonic increasing pressure, the Kelvin-Voigt model was used. A detailed description of this model is shown in chapter 2.4.2. The Kelvin-Voigt model is fitted to the experimental results of $\Delta r_{tde}(t_k)$ and $\Delta r_{tdc}(t_k)$. The fitting parameters describe the deformation components, whereby a distinction of time dependent and independent components is possible. In the general form, the total change in specific flow resistance, Δr_{tot}, is the sum of the time independent initial filtration resistance, r_{ini}, the linear time-dependent change, Δr_{lin}, and the nonlinear time dependent change, Δr_{nonl},

$$r_{tot} = r_{ini} + \Delta r_{lin} + \Delta r_{nonl} \tag{3.20}$$

where,

$$\Delta r_{tot} = r_{tot} - r_{ini} = \Delta r_{lin} + \Delta r_{nonl} \tag{3.21}$$

Jong (1998) demonstrated that Δr_{lin} converges to a maximum value under compression for $t \to \infty$. Such a characteristic is typically described by the Kelvin-Voigt model:

$$\frac{dr_{nonl}}{dt} = -\frac{1}{\tau} r_{nonl} + \widetilde{\Delta r_{nonl}}/\tau \tag{3.22}$$

$$r_{nonl}(t = 0) = 0 \tag{3.23}$$

where τ is the time constant. The values for τ must be fitted to the experimental results. For the case that $\widetilde{\Delta r_{nonl}} = constant$ it is possible to integrate equation (3.22) and one obtains

$$r_{nonl}(t) = \widetilde{\Delta r_{nonl}} \left(1 - \exp\left(-\frac{t}{\tau}\right)\right) \tag{3.24}$$

Equation (3.24) does not describe the long-term asymptotical increase of specific flow resistance very well. The gradient of the experimental data is larger than in equation (3.24). Therefore an additional term must be added. The long-term asymptotical increase seems to be linear within time scale investigated in this work. It is therefore reasonable to assume a proportional relationship as

$$\frac{dr_{lin}}{dt} = \widetilde{\Delta r_{lin}} \tag{3.25}$$

$$r_{lin}(0) = 0 \tag{3.26}$$

Integration leads to

$$r_{lin}(t) = \widetilde{\Delta r_{lin}} t \tag{3.27}$$

Adding equation (3.25) to (3.26) and using relation (3.27), the Δr_{tot} becomes

$$r_{tot}(t) = r_{ini} + \widetilde{\Delta r_{nonl}} \left(1 - \exp\left(-\frac{t}{\tau}\right)\right) + \widetilde{\Delta r_{lin}} t \tag{3.28}$$

where $\widetilde{\Delta r_{lin}}$ is a parameter, which must be fitted to experimental results.

To include the contribution of both viscoplastic and plastic deformations on the total plastic change of the specific flow resistance, it is assumed that the total plastic change of the fiber mat is the sum of the viscoplastic and plastic contribution. Mathematically, this can be expressed as

$$\Delta r_{totpl} = \Delta r_{viscopl} + \Delta r_{pl} \tag{3.29}$$

By inserting equation (3.28) into equation (3.19), the components of the irreversible change in flow resistance, $\Delta r_{viscopl}$ and Δr_{pl}, can be calculated.

The elastic and viscoelastic part of the deformation can be calculated by fitting equation (3.28) to the experimental results of equation (3.17). In both cases, the fitting parameter, r_0, can be interpreted as the plastic or elastic change in the flow resistance, which is the sum of Δr_{pl} and Δr_{el}.

Curve fitting

The relationship between hydrostatic pressure, Δp, and specific flow resistance, r, for the compression and expansion process can be described by a power law in the form:

$$r_i = a\Delta p^b, \qquad r_i(\Delta p = 0) = 0 \tag{3.30}$$

where the parameters a and b are constants that must be determined experimentally. This relationship has already been proven by Grace (1953). Vomhoff (1998), who investigated the deformation behavior during compression and expansion at low pressure, stated that both compression and expansion can be described by a power law.

This assumption seems to be valid, as shown in FIGURE 3.16. The graph shows the experimental results of r during the expansion process and a power law function which is fitted by the least square method.

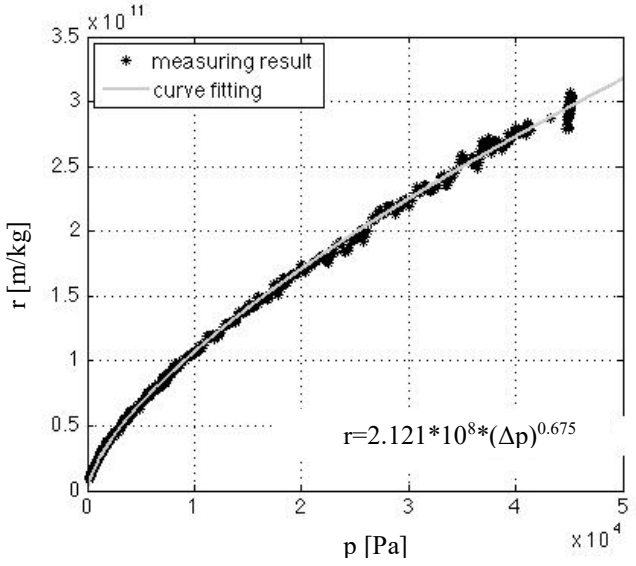

FIGURE 3.16: Specific flow resistance versus hydraulic pressure. The figure shows an expansion of an LF-pulp. The power law agrees well with the experimental results. The R^2-value is above 0.99.

3.6.4 Summary

In this Chapter an apparatus is presented which is designed to represent the dewatering characteristics in a double wire former, as closely as possible. This was accomplished by adding two additional features to the conventional apparatus. First, the sheet forming process and permeability test were decoupled into two separate steps. Since the sheet forming process is completed in the first step and thus the filtration is completed too, the resistance of the formed fiber mat is denoted “flow resistance”. Second, the loading time and the hydrostatic pressure levels could be varied during the permeability tests by the use of predefined switching sequences. The fiber mats were loaded from 0.6 s up to 45 s at a pressure range from 0.4 to 80 kPa. The focus of the experiment is to characterize and to determine deformation related changes in flow resistance. These changes are pure elastic, pure plastic, viscoelastic, viscoplastic.
The permeability experiments were conducted with recycled DIP fiber pulp (RF) for newsprint paper, bleached softwood kraft pulp (LF) and bleached hardwood eucalyptus pulp (SF).

3.7 Results and discussion

3.7.1 Fiber mat flow resistance under compression

Pressure dependency

FIGURE 3.17 through FIGURE 3.19 show the influence of pressure loss on the flow resistance at a pulse length of 600 ms. The investigated pulp types show the same nonlinear dependency of r on p, which is typical for compressible materials. At a low hydrostatic pressure, r increases with a large gradient. At higher pressures loss, the gradient decreases and is almost constant above 20 kPa.

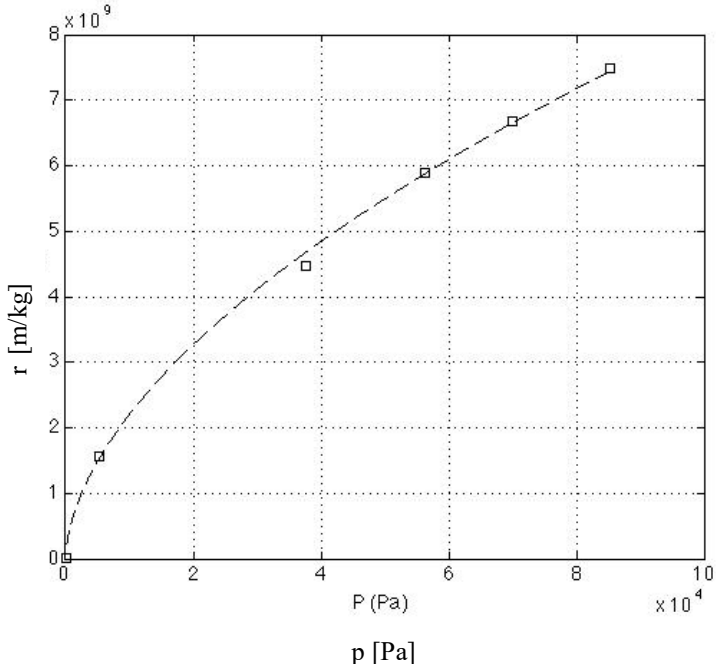

FIGURE 3.17: Specific flow resistance versus pressure for LF pulp. The experiment was carried out at a basis weight of 80 g/m^2. The results show that the specific flow resistance follows the power law of equation (3.30). The parameters are a=9.9103e+7 and b=0.417. The graph shows small curvature at low pressure and an almost linear relation from 40 to 80 kPa.

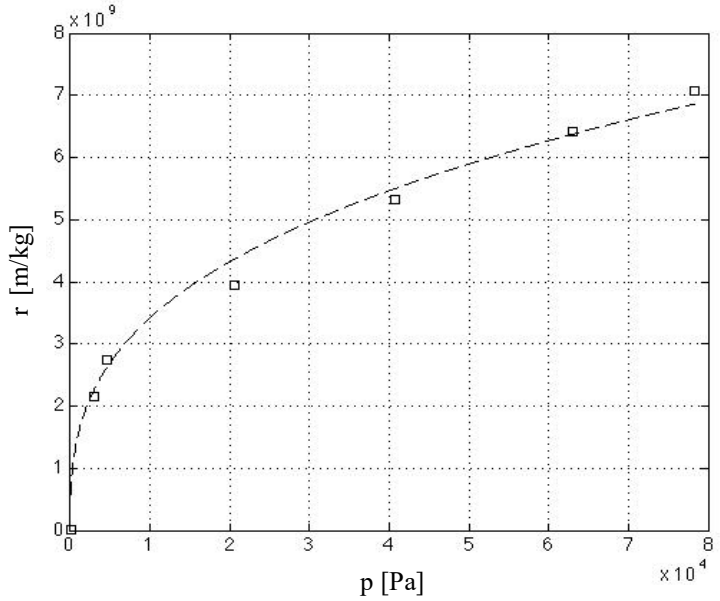

FIGURE 3.18: Specific flow resistance versus pressure for SF pulp. The experiment was carried out at a basis weight of 80 g/m^2. Similar to the behavior of LF pulp, the specific

flow resistance of SF pulp follows also the power law of equation (3.30). The parameters are a=8.15e+7 and b=0.39. The results show a large curvature at low pressure.

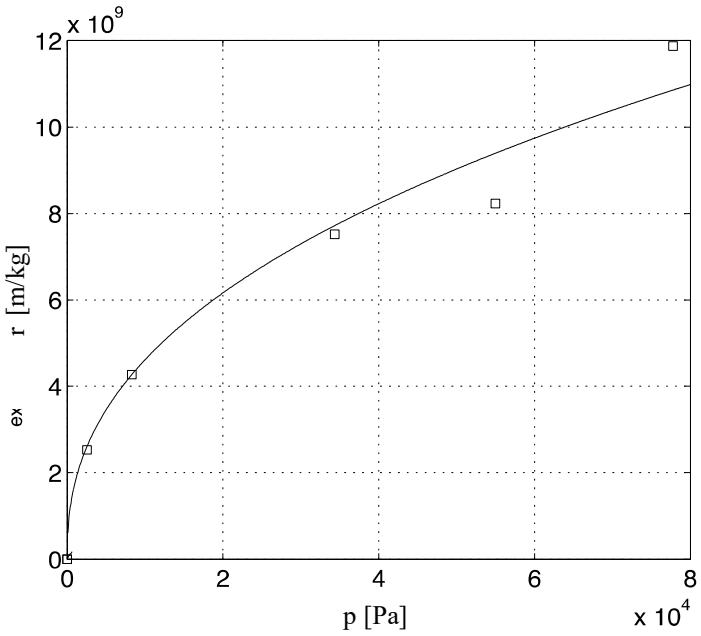

FIGURE 3.19: Specific flow resistance versus pressure for CB pulp. The experiment was carried out at a basis weight of 40 g/m^2. The specific flow resistance of CB pulp fits also the power law of equation (3.30). The parameters are a=5.11e+6 and b=0.64. The results show a similar trend to SF with a large curvature at low pressure.

The deformation process during the experiment, shown in FIGURE 3.17 through FIGURE 3.19, can be described as follows: In the initial state, the fiber mat is built as a loose network at a hydrostatic pressure $P_h(0) = P_{ini}$. The increase in flow velocity and the resulting hydrodynamic drag forces P_d overcome the structural pressure $P_y(0)$, whereby the network is compacted. The fiber mat is deformed plastically and elastically. This is supported by the observations mentioned in chapter 3.6.1 and the observations described in existing literature. This well-known compression process for compressible structures is typically characterized by a total change in the flow resistance r_{tot}, which is the sum of plastic, r_{pl}, and elastic, r_{el}, changes in flow resistance, according to

$$r_{tot}(p) = r_{pl}(p_j) + r_{el}(p_j) \tag{3.31}$$

In these trials, the change rate of the specific flow resistance decreases significantly after a few milliseconds, as the hydrostatic pressure increases. This is a

small period compared to the total pulse length of 600 ms. As a consequence, water flows through the fiber mat at constant hydrostatic pressure. As already stated above, under these conditions the fiber network starts to creep, which results in a rearrangement of the network. The network deforms viscoelastically or viscoplastically. Therefore equation (3.31) must be extended by the viscous term, r_{visco}, to

$$r_{tot}(p_j, t_k) = r_{el}(p_j) + r_{pl}(p_j) + r_{visc}(p_j, t_k) \tag{3.32}$$

The relationship between flow resistance and pressure is essentially a power law in the form of equation (3.30), as shown in FIGURE 3.17 to FIGURE 3.19. For all pulp types, R^2 was higher than 0.96.

The exponent, b, ranges between 0.4 and 0.7, which is characteristic of a degressive curve. These values indicate that the flow resistance tends to a maximum flow resistance for high value of the pressure loss. This means that there is a maximum solid concentration. This is a reasonable assumption as long as the solid volume is constant and no fibers get deformed. Similar results were obtained by Ingmanson & Whitney (1954). Jong (1998) and Vomhoff & Schmidt (1997) to describe the influence of pressure on the concentration used a power law. For the calculation of the flow resistance, they used a relationship similar to the one shown in FIGURE 3.11. They carried out deformation tests at low loads and observed that the concentration reached a maximum at increasing pressure. The exponent obtained by Vomhoff & Schmidt (1997) was approximately 0.3.

Pires et al. (1989) carried out experiments in which a suspension was drained with vacuum under shear conditions. They observed that the flow velocity does not necessarily increase when the pressure is increased. This was not observed in this investigation. An example is shown in FIGURE 3.5. For LF pulp the flow velocity at 80 kPa is 14% higher as compared to the pressure level of 40 kPa. A reason for this different observation is possibly related to the different procedure. As stated in chapter 3.6.1, time plays an essential role during the filtration process. Differences in compression time can lead to a different contribution of deformation components on the total deformation. The consequence is a different curve characteristic.

Time dependency

FIGURE 3.20, FIGURE 3.21, and FIGURE 3.22 show the influence of pulse length on the flow resistance. The curve characteristics of the three pulps are comparable. The behavior of the fiber mat under long-time compression is characterized by a significant change of the specific flow resistance at $t = 0$, and a

moderate viscous change. During the viscous deformation, one can distinguish between a period with a high changing rate up to approximately t=5s and a period with a significant lower changing rate. As a consequence, the assumption of viscous deformation made in equation (3.32), seems to be valid.

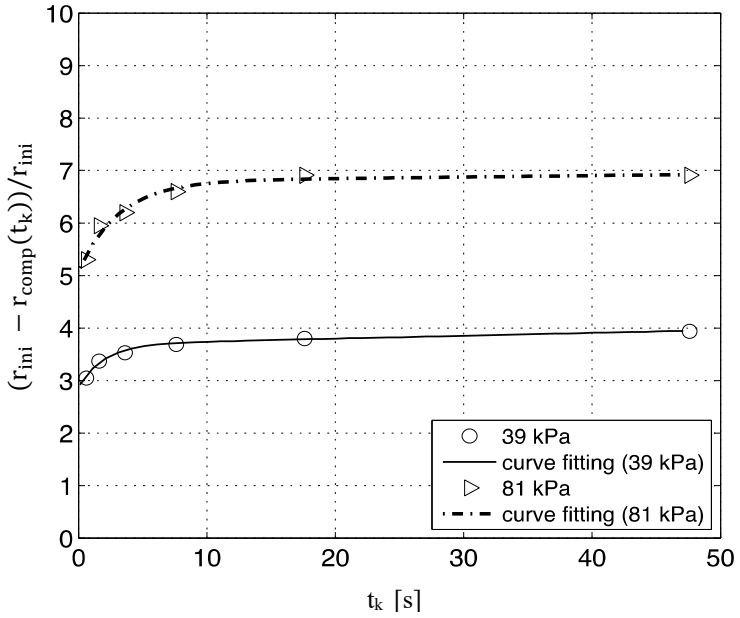

FIGURE 3.20: Specific flow resistance normalized to r_{ini} versus pulse length t_k for LF pulp at a basis weight of 40 g/m^2. The normalized specific flow resistance of LF pulp matches equation (3.28) well. The results show a long-time asymptotical increase. The influence of pulse length is significantly higher than the initial increase.

Δp	Δr_{nonl}	Δr_{lin}	τ	r_{ini}
39 kPa	0.8099	0.00548	1.994	2.88
81 kPa	1.706	0.00270	3.116	5.09

TABLE 3.2: The table shows the parameters of the curve fitting equation (3.28) shown in FIGURE 3.20. The results show a significant difference in the initial flow resistance, r_{ini}, between 39 kPa and 81 kPa.

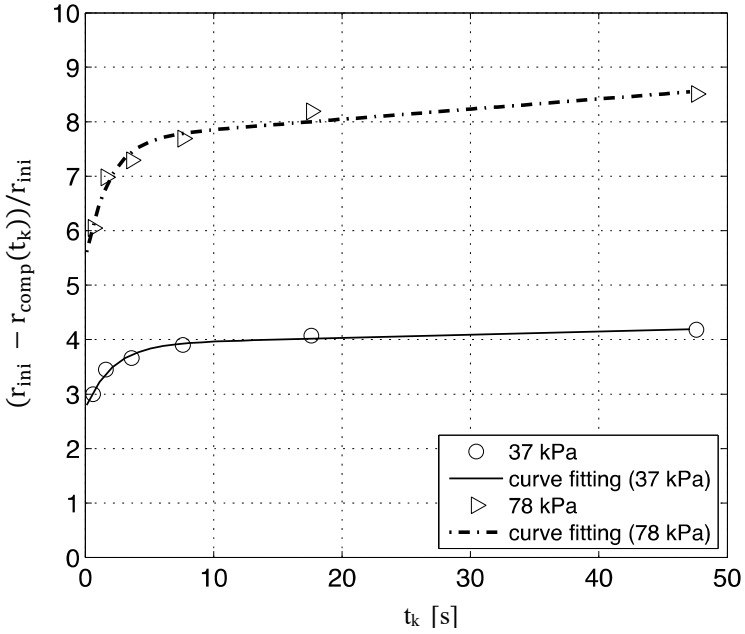

FIGURE 3.21: Increase in r normalized to r_{ini} versus pulse length t_k for SF pulp at a basis weight of 40 g/m^2. The normalized specific flow resistance of SF pulp follows equation (3.28). The results show long-time asymptotical increase. The influence of pulse length seems to be not that significant.

Δp	Δr_{nonl}	Δr_{lin}	τ	r_{ini}
37 kPa	1.17	0.00583	2.141	2.745
78 kPa	2.185	0.01863	1.797	5.488

TABLE 3.3: The parameters of the curve of fitting shown in FIGURE 3.21 and equation (3.28). Similar to the measurements of the LF pulp, the results show a significant difference in the time independent initial flow resistance, r_{ini}.

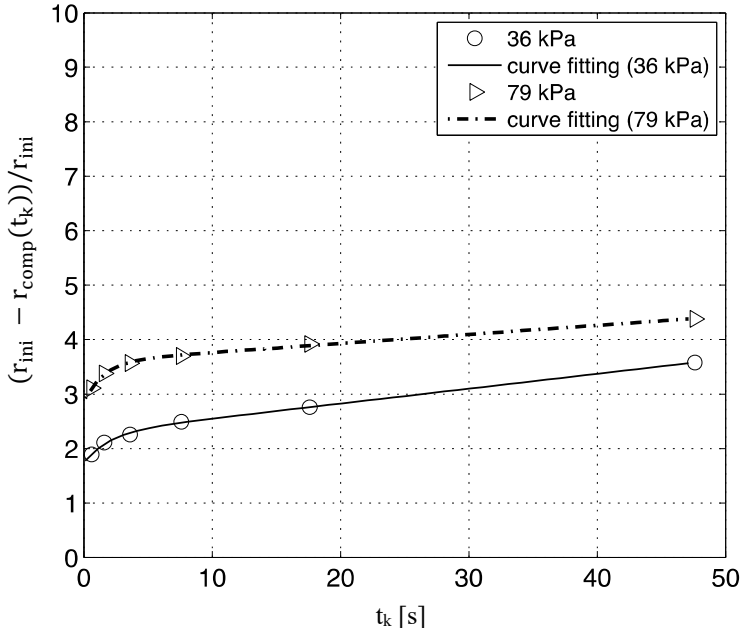

FIGURE 3.22: Increase in r normalized to r_{ini} versus pulse length t_k for CB pulp at a basis weight of 40 g/m^2. The normalized specific flow resistance of CB pulp follows equation (3.28). The results show significant differences in the long-time asymptotical increase.

Δp	Δr_{nonl}	Δr_{lin}	τ	r_{ini}
36 kPa	0.533	0.02729	2.025	1.747
79 kPa	0.722	0.01663	1.555	2.874

TABLE 3.4: The parameters of the curve fitting shown in FIGURE 3.22 and using equation (3.28). The results show significant differences in all parameters. The long-time asymptotical increase in resistance is higher at lower pressure, which is similar to LF and SF pulp.

The relationship between r and τ is described by equation (3.28). Parameters Δr_{nonl} and τ describe the initial increase in specific flow resistance up to a point in which the changing rate seems to be constant; parameter Δr_{lin} describes the long time linear increase in specific flow resistance; parameter r_{ini} is the initial specific flow resistance, which would approximately be reached if the pulse length tends to zero. The reason for the long-time linear increase in resistance is probably the viscoplastic effect. This effect, also called creeping, is a fiber slipping resulting in a rearrangement of fibers which causes a compaction of the fiber mat. Chen (2014) showed in his experiments that the long-time creeping follows a logarithmic law. In this

investigation, a linear description of the long-time behavior is used, which is shown in equation (3.28). The graph is shown in FIGURE 3.23. The mat solids concentration content grows by approximately 10 %. Due to the reorganization of fibers, the fiber mat gets more uniform. This phenomenon is also observed during the two experiments where two fiber mats were formed with different loading times. The sample, which is loaded for several minutes, shows a homogeneous distribution of fibers. In comparison to this, the sample that is removed from the test device after 30s shows small dense flocs. The homogenization of fibers is not restricted to local areas of the fiber mat; it led to a reorganization of fibers of the entire fiber mat. The result is a more dense fiber mat with reduced void volume. In the experiment of Chen (2014), a fiber mat is loaded for 17 min. The fiber mat shows a sustained decrease in height under the influence of the constant hydrodynamic drag forces with a simultaneous increase in drainage resistance. The results are shown in FIGURE 3.23.

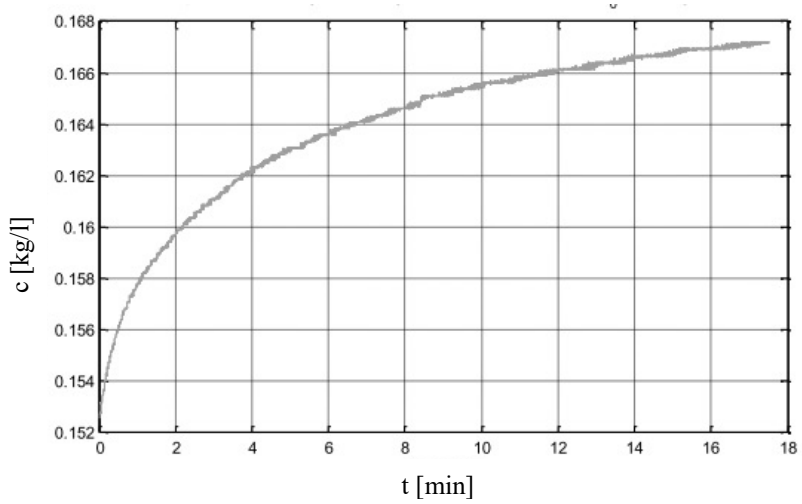

FIGURE 3.23: Mat solid concentration versus time. The continuous loading of a fiber mat led to a sustained increase in solid concentration.

The initial increase in the specific flow resistance is more significant in the case of LF and SF, as shown in FIGURE 3.20 and FIGURE 3.21. An explanation for this phenomenon may be that pulp with longer fibers exhibits a higher compressibility.

The long-time linear increase in resistance is more significant in the case of CB, as shown in FIGURE 3.22. The reason for that might be a low mean fiber length and the existence of fines. Small particles and fibers are not necessarily fixed in the network. The structural stress, which normally fixes the fibers in the network, is not, or only slightly, transmitted via fine particles. So, the particles cannot resist the forces and change the original positions. Already low hydrodynamic drag forces give rise to the movement of fines, and the mobility increases if the driving forces increase. This

is supported by experiments conducted by Wildfong et al. (2000b), who showed that the fines retention decreases if the pressure loss increases. However, these fines do not necessarily contribute to the change of the fiber mat height, because they only occupy part of the void volume, while the height is defined by networked fibers, which form the primary construction of the network. Following this reasoning the redistribution of fines within the fiber network cannot be the main reason for the increase in mat concentration, which is shown in FIGURE 3.23. On the other hand, it is well-known that the fines content and the fines distribution in the network influence the flow resistance significantly (see Wildfong et al. (2000b)). In conclusion, there must be structural changes that are not necessarily represented by the fiber mat height that are responsive for the increase in flow resistance.

Another interesting conclusion suggested by the results is that the creeping rate is not higher at higher hydrostatic pressure, as would be expected for all pulp types. Under static load, the creeping increases when the load is increased. This is shown in the experiments of Wilder (1960). To describe the viscoelastic and viscoplastic decrease in mat height, he added a logarithmic term to the compression equation from Campbell (1947). Under mechanical conditions the force acts in normal direction to the mat surface and is transferred to the contact points between the fibers. Under hydrodynamic conditions, hydrodynamic drag forces act on the entire length of the fibers. The fibers, which are embedded in the network, can also absorb drag forces as long as they are exposed and not covered by surrounding fibers. Due to randomly distributed flow channels through the fiber mat, transversal flows are generated (Bellani, 2011).

A key factor that influences the mobility of an individual fiber in regular and transversal direction is the network strength and the number of contact points of the fibers. The network strength is defined by the counterforces, which hold the fiber in its position. At the contact points, the driving forces for movement and the counterforces are transferred. Due to a higher number of contact points, the hydrodynamic drag forces, which act on an individual fiber, are distributed to more surrounding fibers.

The importance of this effect can be evaluated by calculating the numbers of contact points for different concentration levels during the compression stages. For this purpose, Wahren & Meyer (1964) presented the following calculation method.

$$c_{vol} = \frac{16\pi A}{\left(\frac{2A}{\bar{n}_{con}} + \frac{\bar{n}_{con}}{\bar{n}_{con}-1}\right)^3 (\bar{n}_{con}-1)} \tag{3.33}$$

$$n_{con} = 3n_{crowd}/\,A \quad = 2Ac_{vol} \tag{3.34}$$

$$n_{crowd} = (2/3)AR^2c_{vol} \tag{3.35}$$

The number of contacts between particles is $\bar{n}_{con}$, the volume concentration is c_{vol}, AR is the aspect ratio, and n_{crowd} is the crowding number, which is the expected number of fibers in a spherical volume.

Chen (2014) showed in his experimental results that the mass concentration of a fiber mat for an LF pulp increase from 0.125 g/l to 0.15 g/l if the hydrostatic pressure increases from 37 kPa to 80 kPa. If it is assumed that the aspect ratio, AR, is 60, the number of contact points, $\bar{n}_{con}$, increases from 9 to 10 according to equation (3.33). For pulps with lower aspect ratio, like CB, this effect decreases because of the denser packed fiber mat and lower increase of concentration. This simple analysis shows that the contact points cannot be the major reason for the observed phenomenon.

The directions of forces to fix the particle depend on the points of support in the network. Velocity variations in horizontal direction induce shear forces above and within the network. Hydrodynamic drag forces can act on the particle from various directions. A consequence is that a particle starts to move if it is not supported in the direction in which the hydrodynamic drag forces act. A schematic illustration of this process is presented in FIGURE 3.24, showing two networks with individual fibers indicated by dots. The filled dot represents the fiber onto which the drag, $F_{i,drag}$, and local network forces, $F_{i,sup}$, act (left graph). This illustration represents a network at low compaction pressure and low concentration. The considered fiber is supported by one fiber. The mobility is high. The right graph shows, a network at high compaction pressure and high concentration. The considered fiber is supported by two fibers, thereby mobility is reduced.

This hypothesis does not assume a negligible concentration gradient in z-direction. It is still valid for the case where strong concentration differences exist between the top and the bottom of the fiber mat.

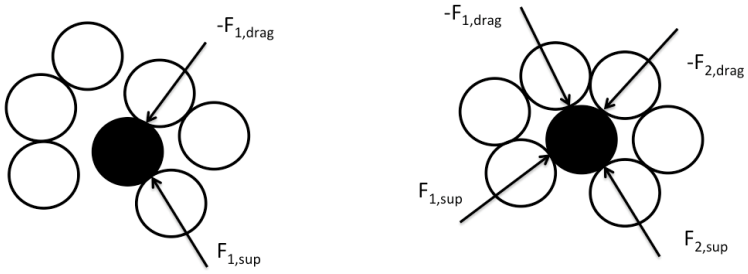

FIGURE 3.24: Illustration of two networks with individual fibers indicated by dots. The filled dot represents the fiber onto which the drag ($F_{i,drag}$) and local network forces ($F_{i,sup}$) act. Left subfigure: A network at low compaction pressure and low concentration. The considered fiber is supported by one fiber. The mobility is increased. Right subfigure: A network at high compaction pressure and high concentration. The considered fiber is supported by two fibers. The mobility is reduced.

These examples show that the transfer and the direction of the forces under hydrodynamic conditions are more complex when compared to cases of mechanical loading by a piston. For a detailed analysis of the force balance and the influence of network geometry, particle-level simulations are required, as it was presented, for example, by Lindström (2008).

The approach used to separate viscoelastic, viscoplastic, plastic and elastic deformation phenomena is only correct for the ideal case. From a theoretical point of view, a similar process takes place during the plastic and viscoplastic deformation. Slippage and rearrangement of fibers cause a compaction of the network. In the case of plastic deformation, fibers change their position to the place where they are stable owing to the higher compaction pressure. So, only some fibers and fines are left, which are loose and show the ability to move. This means that the potential for viscoplastic deformation is reduced due to plastic deformation. Hence, a certain deformation potential can be reached by either plastic deformation or viscosplastic deformation (creep). The ratio between these two processes is determined by the compression history.

3.7.2 Expansion

In FIGURE 3.25 through FIGURE 3.27, the expansion behavior of LF, SF and CB pulp is shown. In the experiment, the fiber mat is loaded for 100 s and slowly expands from a hydrostatic pressure of 85 kPa to 0.5 kPa. The experiments are carried out with 40 and 80 g/m^2. The nonlinear characteristic of the expansion behavior can be

described by a power law relationship. A similar relationship between r and p is indicated in the compression behavior.

FIGURE 3.25 shows r during the expansion process for LF pulp. The flow resistance decreases with decreasing pressure. Different basis weights show overlapping curves. The reason for this could be a similar network structure and deformation behavior at different basis weights. If there is no concentration gradient in z-direction of the fiber mat, the local specific flow resistance is constant at every local position h. This might be related to the fiber characteristic of the LF pulp. The high aspect ratio and the narrow fiber length distribution result in a network in which most of the fibers are fixed in the network and have no possibility to move. The consequence is that no concentration gradient exists in z-direction of the network at this basis weight range. Similar results are presented by Wildfong et al. (2000b), who studied the influence of fines on the flow resistance. The experiments show that the lower the fines concentration is, the lower is the influence of basis weight on the specific flow resistance.

FIGURE 3.26 and FIGURE 3.27 shows the relationship between r and p for SF and CB during the expansion process. The behavior of the CB and SF pulp during continuous expansion shows a strong non-linearity, too, but with a large difference between 40 and 80 g/m^2 compared to LF pulp at which both basis weights show no differences. The difference in r between the basis weights might be caused by the lower aspect ratio of the CB and SF fibers and the existence of fine particles. Different fines distribution in z-direction and different specific fines content at different basis weights might be the reason (Wildfong et al., 2000b).

The compressibility of the pulps can be described by the exponent of the power law function. For all pulps, the exponent does not differ significantly at different basis weights. This was not expected, because it was assumed that different fines contents at the two basis weight levels affect the filtration resistance to a varying extent. Because the LF pulp shows a similar behavior as the CB pulp, it must be assumed that the fines content does not vary between 40 and 80 g/m^2. Thus, a rearrangement of the fines would affect the change in flow resistance to a similar extent, at the basis weight level used in this work. The biggest compression-based change in flow resistance has CB pulp with b=0.7 for both basis weights, while the exponent for LF pulp is much lower at approximately b=0.5. The SF pulp shows the lowest exponent with b= 0.4 at 40 g/m^2 and b= 0.36 at 80 g/m^2. The high values for CB pulp may be caused by a high-density fiber mat, which tends to block the flocs with increasing pressure (Wildfong et al., 2000b).

In an additional experiment, the expansion was investigated during a sequence of four step pulses of 600 ms. The pressure level decreased from approximately 80 kPa to 15 kPa in four steps. The flow resistance at the expansion state after every

compression was taken and was fitted to a power law. The result of the curve fitting is shown in TABLE 3.5. In comparison to the continuous expansion, the r values for the short expansion are significantly lower. This can be explained by weaker viscoplastic behavior for short pulse lengths. This is not the case for LF pulp. The long-time viscoplastic effect is not very significant. This observation matches the results shown in FIGURE 3.21. The LF pulp shows a lower long-time increase in flow resistance than CB and SF pulp.

For CB and SF pulp the exponent is significantly lower in incidents of short expansion. The exponent of LF, however, is the same for continuous and short expansion. The reason for this is not obvious. One possible explanation for this phenomenon is that during the compression and expansion process the fines are washed out. This would also explain why LF pulp, with its low fines content, does not show any differences between short and continuous expansion.

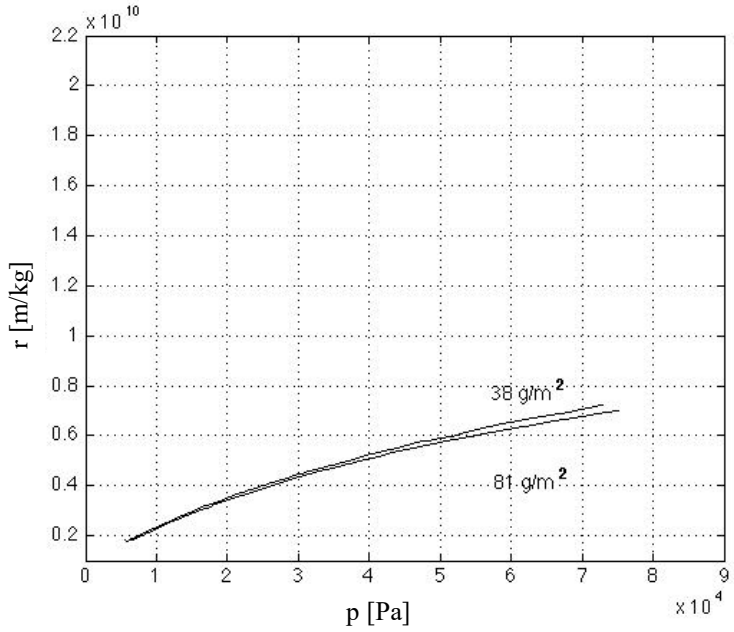

FIGURE 3.25: Continuous expansion of LF pulp for 38 and 81 g/m^2. The curves of both basis weights overlap which indicates a similar network structure.

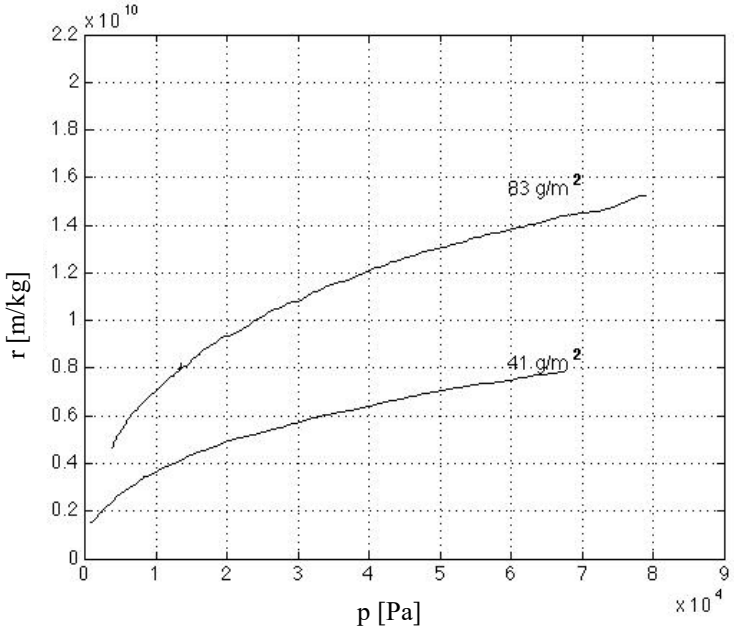

FIGURE 3.26: Continuous expansion of SF pulp for 41 and 83 g/m^2. SF pulp shows the highest nonlinearity compared to LF and CB pulp.

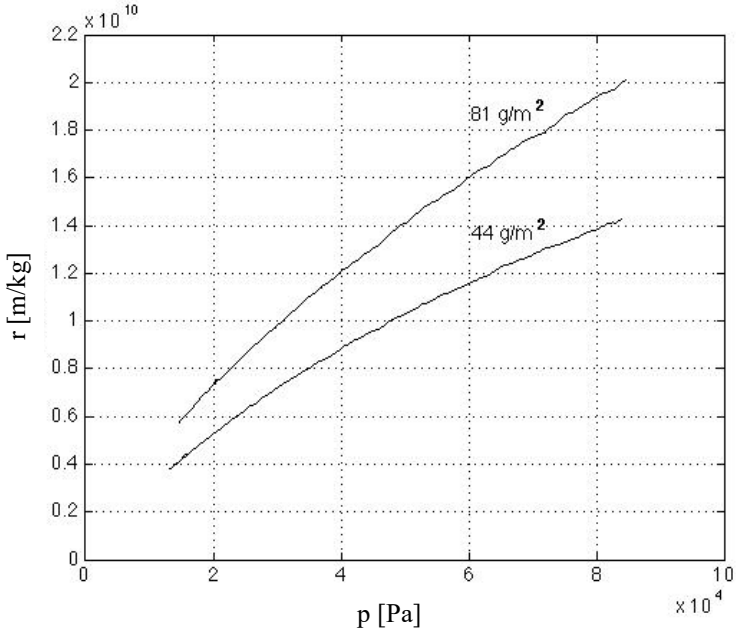

FIGURE 3.27: Continuous expansion of CB pulp for 44 and 81 g/m^2. The curves show an almost linear relationship between flow resistance and pressure loss.

Curve fitting parameters for LF pulp

Trail condition	g/m^2	a	b
Pulse expansion	80	2.13e+7	0.516
Continuous expansion	40	1.32e+7	0.56
Continuous expansion	80	1.396e+7	0.55

Curve fitting parameters for SF pulp

Trail condition	g/m^2	a	b
Pulse expansion	80	1.06e+9	0.168
Continuous expansion	40	9.26e+7	0.4
Continuous expansion	80	2.42e+8	0.368

Curve fitting parameters for CB pulp

Trail condition	g/m^2	a	b
Pulse expansion	40	1.155e+9	0.20
Continuous expansion	40	4,8e+6	0.71
Continuous expansion	80	7.12e+6	0.7

TABLE 3.5: Curve fitting parameters for LF, SF and CB pulp for equation ((3.30). The pulse expansion represents experiments in which the fiber mat is loaded four times with pulses of 600 ms and the pressure decreases with each additional pulse from approximately 80 kPa to 15 kPa. During the continuous expansion, the pressure is decreased monotonically from 80 kPa to 0 kPa.

Pressure dependency

FIGURE 3.28 shows the increase of the specific flow resistance r after a pressure pulse which is calculated by $\Delta r = (r_{exp} - r_0)/r_0$. According to equation (3.18), r shows a pressure-dependent plastic deformation. The measurements follow a power law. The use of the power law is derived from the power law relationship between r and pressure loss during compression and expansion. This assumption is supported by the fact that the relationship between the measurements at the compression state and

the elastic change in flow resistance are linearly proportional, which is shown in FIGURE 3.29. This assumption is valid if $r_{pl,0}(P = 0) = 0$. The R^2 for the fitting results are higher than 0.95.

As shown in FIGURE 3.28, LF pulp shows the lowest gradient of the flow resistance with respect to pressure. CB pulp shows the largest gradient, whereby the differences to LF pulp are not significant for low-pressure, but it increases to a significant extent if the pressure is increased. CB pulp shows an almost linear relationship between the changes of the flow resistance and the pressure. The results of the curve fitting are presented in TABLE 3.6.

As described above, changes in the flow resistance due to viscoelastic, viscoplastic, elastic and plastic deformation emerge during the pressure pulses. In the case of a change due to plastic deformation in the flow resistance, the compressive yield stress is exceeded and the network starts to deform plastically, provided that the relationship in FIGURE 3.11 is valid. The change in the filtration due to plastic deformation is apparent in an increase of r at the expanded state, as compared to the initial state. As discussed above, a plastic change in the flow resistance already in the initial state is assumed. Thus, the results represent only a section of the entire change in the filtration potential of the fiber mat. Due to water flows through the fiber mat for 600 ms during the compression state, an additional viscoplastic and viscoelastic change in the flow resistance occurs. The contribution to the viscoplastic and viscoelastic part of the total change in the flow resistance is not known a priori. A further analysis of the viscosplastic change in the flow resistance is required.

These results prove the hypothesis that a significant plastic change in flow resistance r occurs after a pressure pulse. The magnitude of the change is a function of the height of the pressure pulse. The results also show that the pressure-related changes in flow resistance under compression are in a linear relationship to changes in the expanded state.

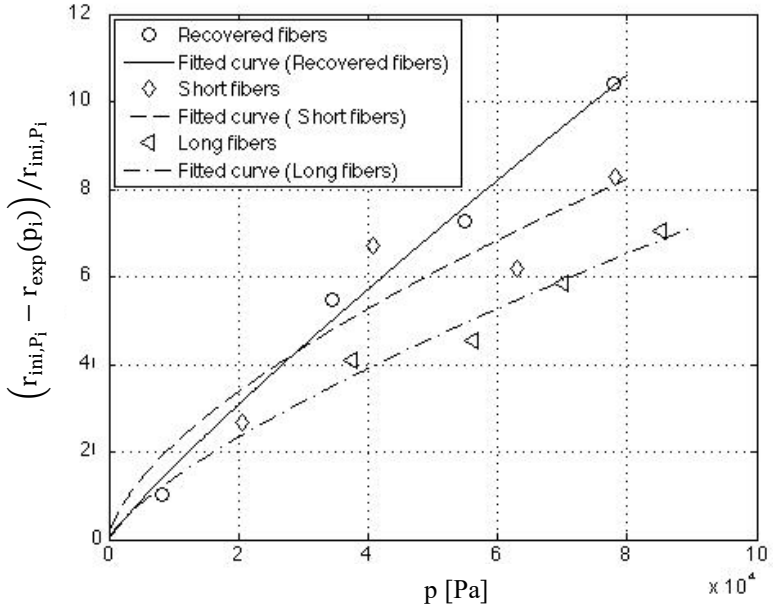

FIGURE 3.28 : Increase of specific flow resistance after various compression levels in the expanded state. At a pulse strength of 80 kPa, the flow resistance is doubled for CB pulp and is increased by approximately 60% for LF pulp.

	a	b
CB	0.0044	0.893
SF	0.0575	0.6435
LF	0.014	0.742

TABLE 3.6: Parameters of the curve fitting of the graphs shown in FIGURE 3.28 for equation ((3.30). The R^2-values of the power law curve fitting are higher than 0.95.

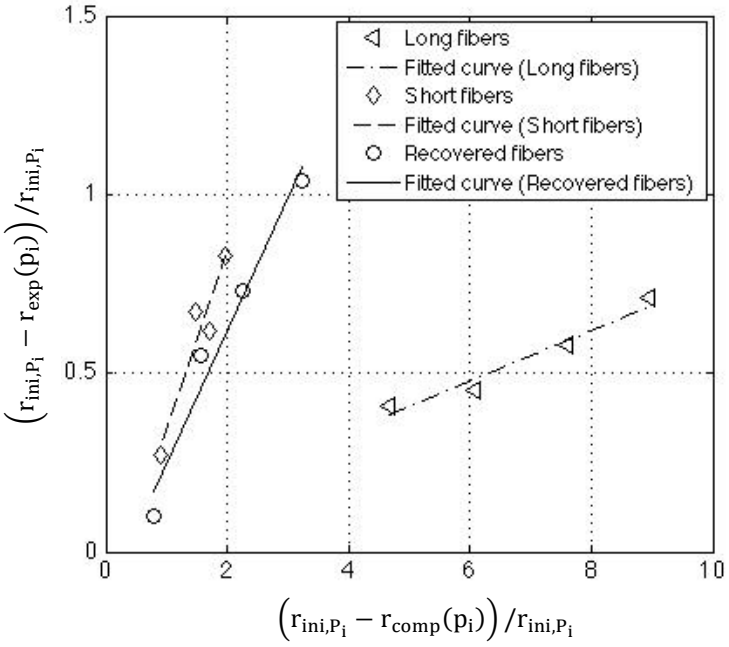

FIGURE 3.29: Correlation between the changes in the flow resistance after the compression process and the changes after the expansion process.

Time dependency

From FIGURE 3.30 to FIGURE 3.32, the changes in r after various pulse lengths are shown. The results reveal the same characteristic as the pulse length experiments during the compression, presented in section 3.7.1, i.e. the higher the pressure pulse is, the higher is the changes in the flow resistance. After a significant increase in the flow resistance up to a few seconds, the values tend to a maximum value.

An interesting phenomenon can be observed in the results. For all pulp types, the relative increase in the flow resistance happens within a very narrow range of about 0.5-1.7(m/kg)/(m/kg). This result was not expected for pulp types with such significant differences in fiber length, fiber length distribution, and thickness. No explanation has been found for this phenomenon so far.

The relationship between the relative change in r during the compression and the relative change at the expanded state is proportional for the pressure range, which is investigated in this work. This fact supports the assumption that viscoplastic changes in flow resistance can be described by a first order system as described by equation (3.28). As already stated above, this approach is used to distinguish between viscoplastic and plastic changes in the flow resistance. The parameter r_{ini} is the plastic change in the flow resistance. The results of the fitting procedure are shown in TABLE 3.7 through TABLE 3.9.

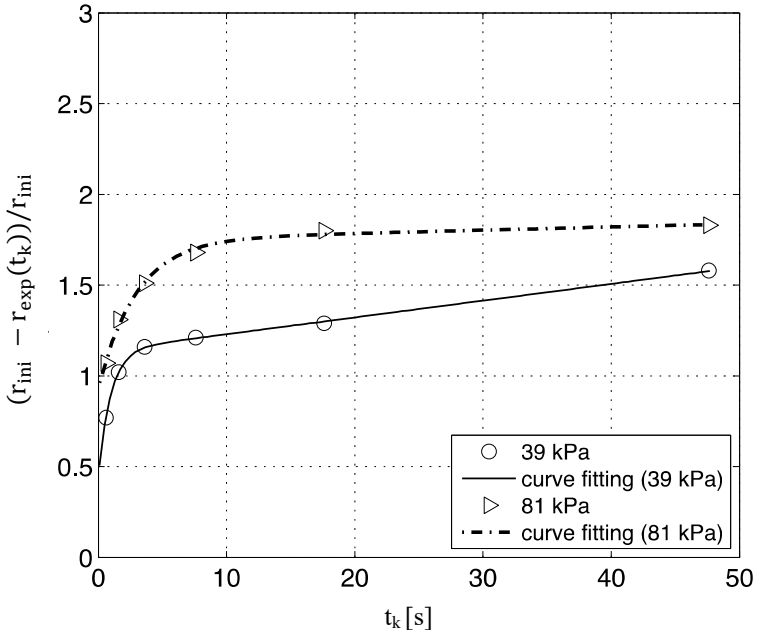

FIGURE 3.30: Increase of r after various pulse lengths at two compression levels (LF pulp). For 39 kPa the slope $\frac{dr}{dt_k}$ of the long time increase in the flow resistance is much higher compared to 81 kPa.

Δp	Δr_{nonl}	Δr_{lin}	τ	r_{ini}
39 kPa	0.702	0.00925	0.946	0.4341
81 kPa	0.815	0.00177	2.933	0.9345

TABLE 3.7: Curve fitting parameter for LF pulp for equation (3.28). At 81 kPa, the parameter r_{ini} is significantly higher than at 39 kPa.

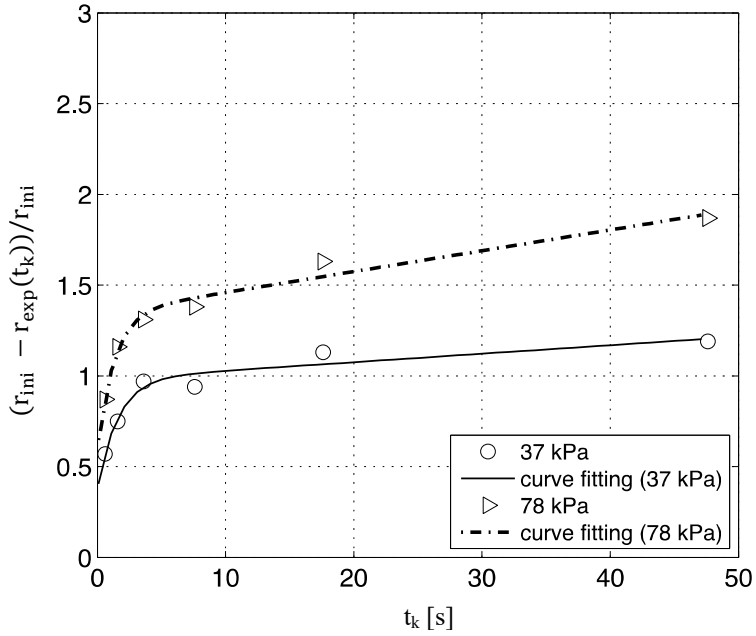

FIGURE 3.31: Increase of r after various pulse lengths at two compression levels (SF pulp). The slope at a high pulse length for 37 kPa is significantly lower than for 78 kPa.

Δp	Δr_{nonl}	Δr_{lin}	τ	r_{ini}
37 kPa	0.614	0.00468	1.572	0.367
78 kPa	0.755	0.0115	1.314	0.589

TABLE 3.8: Curve fitting parameter for SF pulp. The differences between the plastic change in the flow resistance r_{ini} for two different pressure levels is significantly lower than for LF pulp.

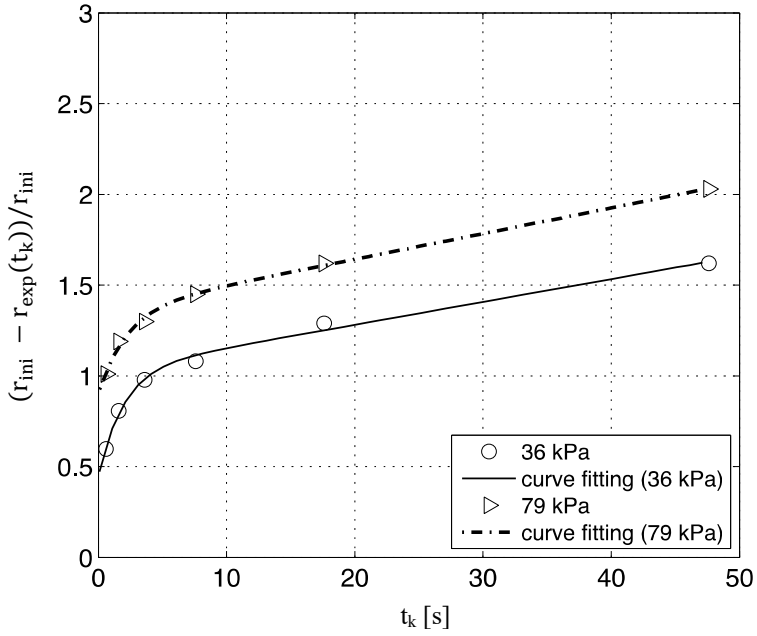

FIGURE 3.32: Increase of r after various pulse lengths at two compression levels (recovered fibers). The slope for two different pressure levels is similar.

Δp	Δr_{nonl}	Δr_{lin}	τ	r_{ini}
36 kPa	0.587	0.0126	1.943	0.442
79 kPa	0.454	0.01416	2.19	0.9041

TABLE 3.9: Curve fitting parameter for CB pulp. Similar to LF pulp, the plastic change in the relative flow resistance r_{ini} is significantly higher at the pressure level of 79 kPa as compared to a pressure level of 36 kPa.

3.7.3 Summary

The experiments were carried out in four individual sections. In the first two sections, the pressure and time dependency of the flow resistance during the compression were analyzed. In the last two sections, the pressure and time dependency of the flow resistance during the expansion process were analyzed. The pressure dependency shows the influence of pressure loss on the flow resistance at a pulse length of 600 ms. The investigated pulp types show the same nonlinear dependency of the flow resistance on the pressure loss, which is typical for compressible materials. At a low hydrostatic pressure, the flow resistance increases with a large gradient. At higher pressures loss, the gradient decreases and is almost constant above 20 kPa.

Time dependency experiments show the influence of pulse length on the flow resistance. The curve characteristics of the three pulps are comparable. The behavior

of the fiber mat under long-time compression is characterized by a significant change of the specific flow resistance at $t = 0$, and a moderate viscous change. During the viscous deformation, one can distinguish between a period with a high changing rate up to approximately t=5s and a period with a significant lower changing rate. As a consequence, the assumption of viscous deformation made in equation (3.32), seems to be valid.

Pressure dependency during the expansion: In the experiment, the fiber mat is loaded for 100 s and slowly expands from a hydrostatic pressure of 85 kPa to 0.5 kPa. The nonlinear characteristic of the expansion behavior can be described by a power law relationship. A similar relationship between the flow resistance and the pressure loss is indicated in the compression behavior.

Time dependency during the expansion: The results reveal the same characteristic as the pulse length experiments during the compression, i.e. the higher the pressure pulse is, the higher is the changes in the flow resistance. After a significant increase in the flow resistance up to a few seconds, the values tend to a maximum value. This fact supports the assumption that viscoplastic changes in flow resistance can be described by a first order system.

3.7.4 Modeling of the fiber mat dewatering in a twin wire former

Boundary conditions and simplifications

As indicted by the experiments and the literature review, the compression behavior of pulp fiber mats contains the following deformation components:

- Elasticity
- Plasticity
- Viscoplasticity
- Viscoelasticity

For modeling these phenomena and including the compression history, an incremental formulation is required. Typically, this is accomplished by using hysteresis operators. For a more detailed description see Brokate & Sprekels (1996) and Visintin (1991). The objective is to generate a simple model that covers all relevant phenomena, and includes the compression history of the fiber mat, which is typical for the dewatering process during the sheet forming process in a fast double-wire paper machine.

The typical machine speed of a double wire paper machine is between 20 and 30 m/s. The dewatering zone is approximately 2 to 3 m. That means that the dewatering time takes approximately 150 ms. Furthermore, the pressure profile in the

suspension between the wires varies significantly. At the forming roll, a typical suction pressure is approximately 10 to 20 kPa. At the suction boxes and the blades, the difference pressure varies typically between 15 to 60 kPa. In fact, the time with almost no pressure difference is approximately 50% according to the pressure profile measurements shown in FIGURE 1.1. This leads to a reduction of the time span, in which water flows through the fiber mat to approximately 75 ms. That means that deformation phenomena with a time horizon of more than 75 ms are not relevant for the modeling a modern gap former.

Furthermore, the experiments show that the long time asymptotical strain rate can be described by equation (3.28). Since the shortest pulse lengths in these experiments are 600 ms, values for the changes in the filtration resistance for smaller pulse length must be calculated by extrapolation. If it is assumed that the initial slope at t = 600 ms is the same at t = 75 ms the increase during a compression time of 75 ms is 4% and 1% for a compression level of 36 kPa and 81 kPa for LF pulp, respectively, as shown in FIGURE 3.33. Compared to the plastic change of a flow resistance of 43% and 93%, the viscoplastic change can be neglected for time ranges smaller than 75 ms. FIGURE 3.33 shows the results of the change in flow resistance for a short time scale.

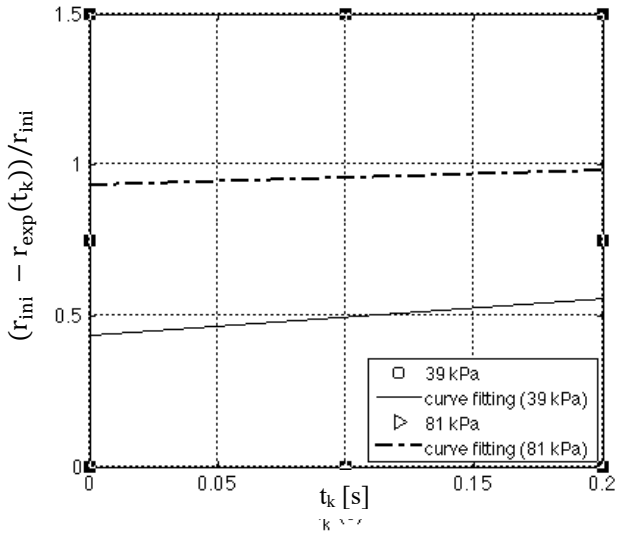

FIGURE 3.33: Rate dependent changes in a specific flow resistance using equation (3.28). The analysis shows that for short time intervals up to 75ms, the change in flow resistance is not significant.

Another observation during the experiments, which allowed a simplification of the gap former model, is that the plastic change in flow resistance is simply a function of time and pressure. The same plastic change in flow resistance can be expected if the fiber mat is compressed 10 times for 1 sec or one time for 10 sec at the same pressure. The first compression significantly dominates the rate, independently of an irreversible change in the flow resistance as long as the maximum pressure level at the compression state is the same for different experiments with different compression histories. This can be shown by the fact that for the same compression time the final pressure levels at the experiment in FIGURE 3.14 are the same. This is true although the numbers of compression and the compression history are different. As a consequence, the maximum pressure during the entire compression history of the fiber mat determines the plastic and elastic change in flow resistance. In order to model the flow through a fiber mat in a modern gap former, some simplification can be done.

- The viscoplastic changes in flow resistance at time spans smaller than 75 ms are one order of magnitude smaller than the rate-independent changes in flow resistance. For this reason, viscoplastic changes in the flow resistance can be neglected.
- Expansion and compression cycles do not contribute to changes in the flow resistance.
- The plastic change in the flow resistance depends on the maximum pressure level during the pressure history.

Governing model equation of the fiber mat behavior in a twin-wire former.

A model is developed that describes the influence of pressure on the flow resistance of a fiber mat. As the experimental results show, the viscoplastic changes in flow resistance can be neglected. Equation (3.20) can therefore be simplified by removing the term for viscoplastic changes in the flow resistance. The total specific flow resistance, r_{tot}, is the sum of the elastic and plastic changes in the flow resistance and can be expressed by:

$$r_{tot} = r_{el} + r_{pl} \tag{3.36}$$

Where r_{el} refers to the elastic change in the flow resistance and r_{pl} is the plastic change in the flow resistance. Both components of the total specific flow resistance are modeled independently.

The influence of pressure on the rate-independent elastic deformation can be described by the function

$$r_{el}(p) = a_{el} * p^{b_{el}}, \qquad r_{el}(p = 0) = 0. \tag{3.37}$$

The constants a_{el} and b_{el} are parameters to be estimated from experimental results. The expression was used in modeling the nonlinear elastic change in the flow resistance.

The plastic change in the flow resistance r_{pl} is assumed to be a function of p_{max}. This method is used in order to consider the entire history. The expression for the nonlinear plastic change in the flow resistance is modeled by

$$r_{pl}(p_{max}) = a_{pl} * p_{max}^{b_{pl}}, \qquad r_{pl}(p_{max} = 0) = 0. \tag{3.38}$$

where a_{pl} and b_{pl} are fitting constants and p_{max} is the maximum pressure of p_{max} = max(p(t)). Equation (3.37) and (3.38) can be inserted into equation (3.36). The total total specific flow resistance r_{tot} can then be described by

$$r_{tot}(p, p_{max}) = a_{pl} * p_{max}^{b_{pl}} + a_{el} * p^{b_{el}}. \tag{3.39}$$

These constants can be determined with the least-square method.

Simulation of experimental results

Equation (3.39) is used to simulate the experimental results. The values of the ideal plastic and elastic change in flow resistance are modified experimental results. The parameter r_{ini} in equation (3.28) calculates the plastic and elastic component of the total change in flow resistance. The ideal plastic and ideal elastic behavior cannot be distinguished by the real experimental data from the test devices evaluated within the scope of this work. Due to the viscous behavior of a fiber mat, the network starts to creep immediately after the forces act. Comparisons between the modified experimental results and the simulation are shown from FIGURE 3.34 to FIGURE 3.36.

The ratio of the elastic change in the flow resistance is dominant for all tested pulp types. The ratio of plasticity for LF and SF pulp is 14% and 10% of the total change, respectively. The highest ratio of plasticity is shown by the recovered fiber pulp with 30%. Sayegh & Gonzalez (1995) presented plasticity ratio for mechanical pulp between 55 to 80% and less than 10% for kraft pulp. These values are not comparable with the data presented in this work. In contrast to the values presented by Sayegh & Gonzalez (1995) who calculated the sum of ideal plasticity and viscoplasticity, this analysis separates ideal plasticity and viscoplasticity. However, the observation that pulp types with lower fiber length distribution shows lower plasticity than pulps with

higher fiber length distribution is made in both works. LF pulp tends towards lower plasticity than pulps with fiber fines like recovered fibers. A possible reason for this phenomenon is that the lower fiber length of recovered fiber pulps leads to a higher slipping and rearrangement of fibers and fines. This is caused by a lower crosslinking of the fibers inside the network as well as a lower mechanical stability of the network.

For the three pulp types, the plastic change in flow resistance shows an almost linear relationship between the relative change and the pressure. The SF pulp shows a slight curvature for the plastic change in the flow resistance. The graphs for the elastic change in the flow resistance show a higher curvature than those for the plastic change in the flow resistance. For the LF pulp and recovered fiber pulp a linear relationship would also be applicable. The usage of a power law is motivated by higher R^2 values at the parameter fitting.

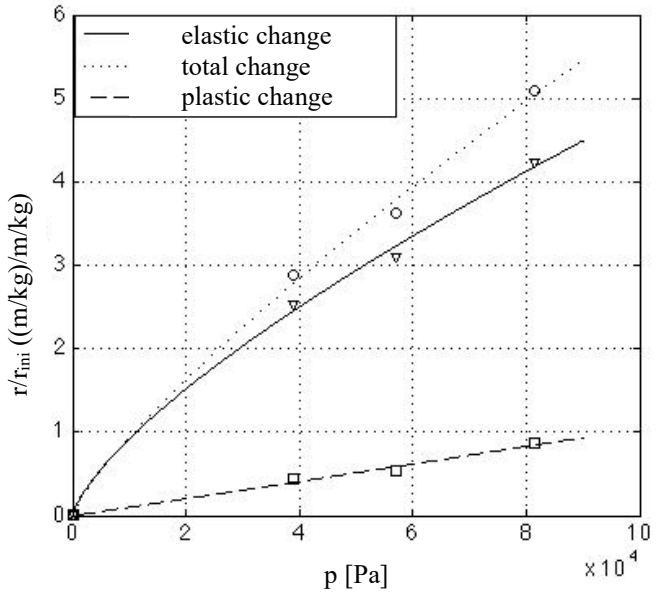

FIGURE 3.34: The plastic, elastic, and total changes in the flow resistance versus pressure for LF pulp. The figure shows the modified experimental measurements and the simulation results. The simulation is in good agreement with the experiments. The fitting parameters are listed in TABLE 3.10. The R^2-values are higher than 0.99. The plastic change in the flow resistance corresponds to 20% of the total change at a pressure of 80 kPa.

	a	b
total change	0.0005587	0.8053
plastic change	7.955e-06	1.023
elastic change	0.001173	0.7232

TABLE 3.10: Parameters of the curve fit of equation (3.37) and (3.38). The total change is the sum of the elastic and plastic change. The plastic change in the filtration shows an almost linear relationship between $\frac{dr}{dp}$ and p. The graphs of elastic and total change show a slight curvature at low pressure.

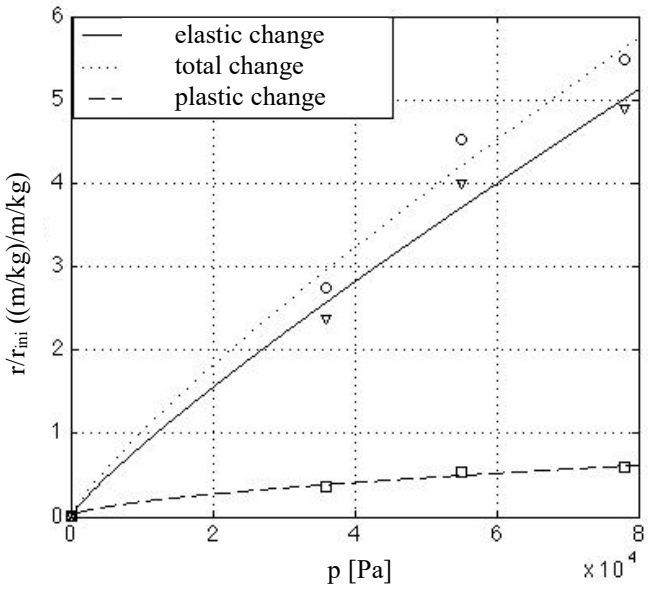

FIGURE 3.35: Total elastic, and plastic relative change in the flow resistance for SF pulp. The elastic change in the flow resistance is the dominating part compared to the plastic change. It corresponds to 90% of the total change. The R^2-values are higher than 0.98.

	a	b
total change	0.000481	0.831
plastic change	0.000773	0.592
elastic change	0.000297	0.863

TABLE 3.11: Curve fitting parameters of equation (3.37) and (3.38). The ideal plastic change in flow resistance is approximately 10% of the total change. The major part is the elastic change with 90% of the total change.

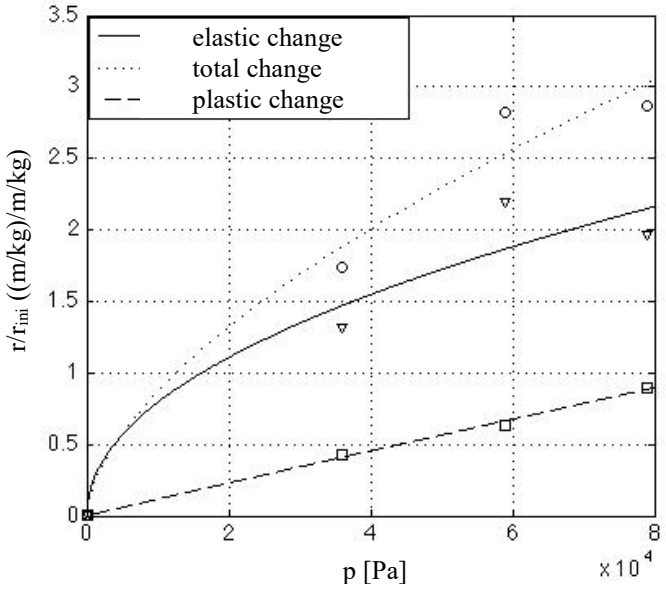

FIGURE 3.36: Total, elastic, and plastic changes in the flow resistance versus pressure for recovered fibers. The plastic change corresponds to 30% of the total change in the flow resistance. The R^2-values are higher than 0.95.

	a	b
total change	0.00337	0.6029
plastic change	1.39e-5	0.9809
elastic change	0.00921	0.4835

TABLE 3.12: Curve fitting parameters of equation (3.37) and (3.38). The curve characteristics of the total and elastic change differ significantly from the LF and SF pulp due to a much higher curvature.

3.7.5 Conclusion

A test device was developed to investigate the relationship between flow velocity, pressure loss, and fiber mat height during the sheet forming process. The test device has been validated and found to be in good agreement with the existing data from literature for the investigation of the flow resistance.

The results from the strain measurement reveal that the different pulp types have a linear relationship between specific flow resistance and modified compressive strain for a pressure level ranging from 10 to 80 kPa. This result differs from existing literature. The reason for this discrepancy is assumed in a different pressure and a different concentration level. Ingmanson (1952) presented a non-linear relationship between a concentration range of the compressed fiber mat from 8% to 16%. The concentration range in this work was from 11% to 15%. In this narrow concentration range, the nonlinearity is not significant and can be correlated by a linear function. For a larger concentration range a nonlinearity would be expected.

This assumption could not be validated by the experiments due to the limitations within the measurement of the flow velocity. The compression behavior of the fiber mat indicates the existence of elastic, viscous, and plastic deformation after a pressure pulse. The viscous effect seems to be viscoplastic deformation. The viscoelastic deformation was not significant for the experiments carried out.

The experiments of the change in the flow resistance during compression and expansion reveal a power law relationship. The exponent is characteristic for a digressive curve. These values indicate that the flow resistance tends towards a maximum flow resistance for high values of pressure loss. This means that there is a maximum solid concentration.

The compression of the fiber mat with constant pressure shows a continuous increase of the flow resistance. The reason for this behavior is probably the viscous effects, also called creeping, which is caused by a fiber slipping and a rearrangement of fibers.

The experiments, in which the pulse time is varied, are described by the Voigt model. This approach enables the calculation of the viscoplastic, viscoelastic, plastic and elastic components of the change in the flow resistance. This procedure is carried out for the elastic and plastic components. The plastic component of the flow resistance is characterized by an almost linear relationship between pressure and flow resistance. The elastic component is described by a power law. The elastic change in flow resistance is dominant for all tested pulp types. The ratio of plasticity for SF pulp is 10% of the total change. The highest ratio of the plasticity is shown the recovered fiber pulp with 30%.

A model is created which describes the influence of pressure on the flow resistance of a fiber mat for the elastic and plastic changes in the flow resistance. The results show that the compression history has a significant influence on the flow resistance. A maximum function for the plastic component is used, to consider this effect in the model.

Chapter 4

4 Modeling dewatering in a double wire former

In this Chapter a simulation of a double wire former section is presented that shows the influence of backflow on the pressure profile. The model includes a variable flow resistance, which changes from the flow resistance of the wire in the case of backflow to the combined flow resistance of the fiber mat and wire in the case of drainage. The effect of backflow is illustrated at segment of the former section between the forming roll and the first blade where the wire is unsupported. The simulation includes the calculation of the release point of the wire from the forming roll.

4.1 Introduction

The modeling in this work seeks to achieve two objectives: first, the investigation of the backflow phenomenon, and second, the extension of the model library, that was recently published by Holmqvist (2002).

The model library of Holmqvist (2002) covers a blade module and a free wire section. In order to simulate an entire former section, a suitable description of the forming roll, including the impingement point and the release point of the wire, is required. In this work, the simulated section ranges from the release point of the forming roll to the first blade in downstream direction. More specifically, the location of the release point of the bottom wire at the forming roll is calculated. The influence of wire speed, wire tension and inlet gap size on the wire positions is analyzed. This section is chosen because it is here that backflow is expected, based on the work of Schmidt-Rohr (2007), who reported that the wires are separated from each other in this section. He mentions that this leads to defects in the paper, which are appear to be

caused by backflow. In the simulation, the flow situation can be analyzed and the parameter which influences backflow can be identified.

4.2 The computational model

A review of literature shows several investigations, that have dealt with this subject. The most relevant works are from Dalpke & Green (1999), Holmqvist (2002), Martinez (1998) and Roshanzamir et al. (2000). These investigations were carried out in terms of applicability for the simulation of the suspension dewatering in a double wire former. The following criteria were applied for the model presented in this work:

- Dominant physical processes are covered.
- Precise prediction of the pressure difference in the suspension core.
- Modeling the fiber mat and the suspension core as a continuum.
- Definition of initial and boundary conditions, to describe the dewatering in a double wire former.

The model, which includes most of these criteria, was presented by Holmqvist (2002). The model library includes former elements such as suction boxes or loadable and curved blades. Through the creation of models for separate components, more complex composite models can be built. The simulation was in good agreement with experimental results for a low filtration resistance. At a high filtration resistance, the system showed oscillations with high amplitudes for the pressure inside the suspension. This behavior is not observed for the pressure distribution that occurs in a real former. An additional limitation of the model is the assumption that the backflow from outside of the wire needs to overcome the filtration resistance of the wire and the fiber mat. This assumption is not valid a priori.

For the model developed in this work, the system of equations from Holmqvist is used as a foundation. Some simplifications were introduced to achieve a higher accuracy of the prediction. Additionally, the following refinements were made:

- a flow-direction-dependent filtration resistance
- a water layer between wire and fiber mat in the case of backflow
- effects of doctoring of drag water at the outside of the wire

4.2.1 The scope of the model

The model structure is split into two identical model components from the center of the suspension layer up to the wires on both sides. Each model component has a wire layer, a fiber mat layer, a liquid layer and half of the suspension layer. It is further assumed that the suspension layer is not removed completely. This assumption seems to be valid because typically the drained water volume at this position is less than two thirds of the suspension injected at the inlet of the forming roll. This means, more than one third of the suspension is still remaining between the upper and lower fiber mat. The individual layers are described as continua with a defined boundary layer and a constant density along the thickness of the layers. A simplified illustration of the model is shown in FIGURE 4.1.

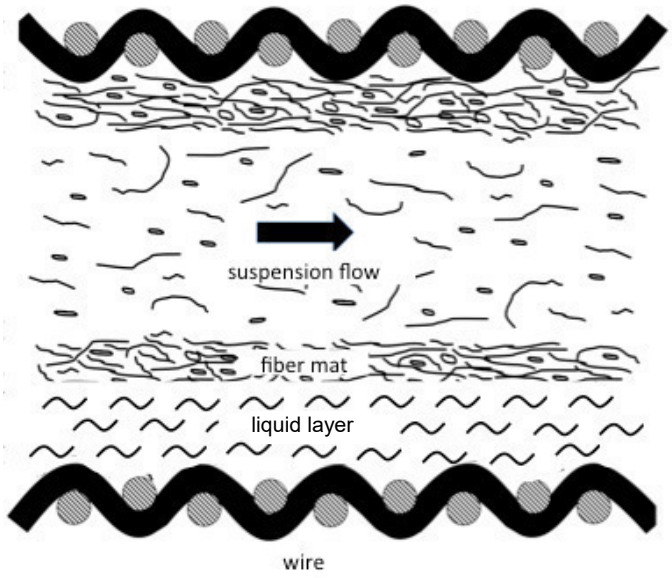

FIGURE 4.1: Schematic description of a double wire segment. The segment is covered by two wires on each side. On the surface of the wire the filtered fiber mat is deposited. The suspension is in the middle of the segment.

In this work, a model is developed which covers the section between the release point from the wire at the forming roll and the first blade. In FIGURE 4.2. the model domain is marked. The model determines the position of the wires in this section. The model is built up by a lower and an upper wire. The lower wire has a fixed position on the surface of the forming roll, and the upper wire is fixed at a blade downstream. The model segment, which is modeled in this work, is shown in FIGURE 4.2.

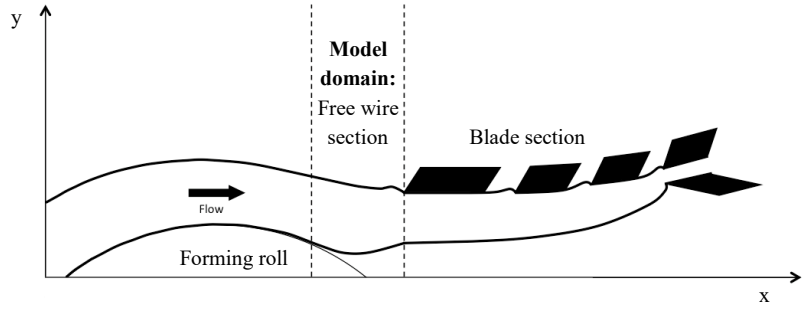

FIGURE 4.2: Schematic illustration of the initial dewatering in a double wire former. The dewatering elements from left to right: Forming roll, free wire section, Blade section.

4.2.2 Analysis

The flow through the wires and fiber mats

The wires and the fiber mats are treated as individual layers with their individual permeabilities. For reasons of simplicity, it is assumed that both layers can be considered as a continuum. Holmqvist (2002) suggested defining the wire and the fiber mat as one layer with a combined filtration resistance. This simplification must be removed, to enable a flow-direction-dependent filtration resistance in the case of backflow. An illustration of the segment, starting at the center of the suspension, is shown in FIGURE 4.3.

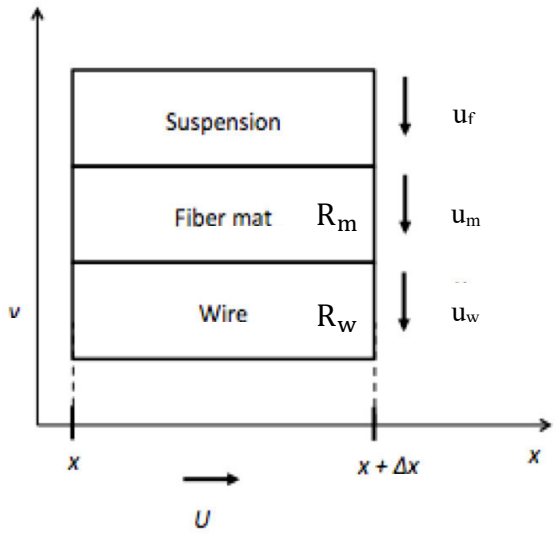

FIGURE 4.3: Illustration of a wire segment with the fiber mat and the suspension. Here R_m is the fiber mat resistance, R_w is the wire flow resistance, and u_s, u_m, u_w are the flow velocities from the suspension in y-direction, the fiber mat, and the wire, respectively. The speed of the wire, the fiber mat and the suspension in x-direction is U.

The total flow resistance of the wire and the fiber mat, R_{tot}, is modeled as the sum of the individual flow resistance of the fiber mat, R_m, and the wire, R_w.

$$R_{tot} = R_w + R_m \tag{4.1}$$

Here, a simplification was made. As reported by Han (1962) the total filtration resistance is not simply the sum of the filtration resistance of the wire and the fiber mat. There is a third filtration resistance component, which called interfacial resistance. This resistance is caused by the interaction between the fibers and the wire. Yet in this study, an empirical filtration curve is used which is determined by experiments with a forming wire; here the filtration resistance data includes already the interfacial resistance.

The filtration resistance of the wire is typically described by the Forchheimer equation (2.7). This expanded Darcy equation that describes not only the viscous but also the inertial pressure loss is required at higher flow velocities (Dalpke, 2002).

Another drawback of the model by Holmqvist is the linear dependency between the basis weight and the filtration resistance, R. This assumption seems to be

reasonable if the increase in basis weight is marginal due to a low drainage rate or even hindered due to the direct contact with the blade. In the model of the forming roll, a high drainage rate leads to a fast increase in basis weight. Thus, this approach would not be applicable. This can be assessed by experiments. Typically, one third of the total water volume is drained at the upper and one third at the lower wire (Lobosco, 2004). Assuming that a basis weight of 90 g/m^2 is produced, a fiber mat layer of 30 g/m^2 deposits at the surface of each wire. In order to include the basis weight dependency in the model and to enable a higher applicability, various approaches are available. In an earlier work, we proposed to use a power law relationship (Flitsch et al. 2013). This approach contains no physical fiber properties and does not provide any information about the local properties of the fiber mat. The form of the power law is

$$R(B) = aB^{b} \tag{4.2}$$

where a and b are the fitting parameters, which are determined by a least-square regression and B is the basis weight. The use of equation (4.2) however limits the application of the model since the compression history is not taken into account.

Backflow

In the simulation results from Holmqvist (2002), the suspension pressure decreases below the level of the exterior pressure. This is caused by a high suction pressure, which acts on the wire. The curvature of the wire changes from concave to convex form. A schematic illustration is shown in FIGURE 4.2. The distance between the wires is higher in the free wire section compared to the forming roll section. The effect on the flow condition was discussed by Holmqvist (2002), who claims that a negative pressure drop occurs only under certain circumstances. The first situation is when a flow exists from outside the wire to the suspension side, a process called “backflow”. The flow direction of the suspension changes the sign at the convex side. The second situation is when the surface tension of the fluid causes menisci to form in the void volume of the wires. Holmqvist assumes that menisci resist forces up to 1 kPa until the water gets sucked out of the pores. At higher pressure differences, backflow takes place. In this work, it is assumed that backflow occurs, but at the same time, the negative internal pressure caused by menisci can be neglected. In this case, the essential question is which medium, liquid or air, flows from the outside into the wire. For the first scenario, it is assumed that air is flowing through the wire. This assumption can probably be discarded for several reasons. Schmidt-Rohr (2007) measured internal pressures between -1 and -3 kPa. Since the viscosity is about 1/50 of water, the flow velocity of the air through the wire would be 50 times higher

compared to water according to equation (3.15). A typical flow velocity of water at the dewatering process is 0.5 m/s (Lobosco, 2005). For air, the flow velocity would be 5 m/s. This would lead to an air layer of 5 cm, if the backflow occurs for 0.2 m along the dewatering line in a paper machine and the machine speed is 20 m/s. So, the thickness of the air layer would approximately 5 times more than a typical distance between the upper and the lower wire. The result would be strong forces on the suspension and probably a destruction of the already build fiber mat. This phenomenon has not been observed at an industrial paper machine. It is therefore not appropriate to assume an air layer. There is another reason contradicting this assumption: Water adhering to the outside of the wire and water within the void volume of the wire must be removed before air can pass into the wire. The assumption that a water layer exists on the outside of the wire was introduced by Roshanzamir et al. (1999). They assumed the magnitude of the liquid layer to be about 0.5 mm. With the assumption that a typical wire thickness is 1mm, and the void volume is 0.5, the available liquid corresponds to a layer thickness of 0.5 mm for the water storage capacity of a wire. If these two assumptions are valid, air can only start to flows through the wire at a point at which both liquid layers, on the surface and within the wires, disappear completely. This specific point depends on the available amount of the liquid, the flow velocity, as well as the length over which the backflow happens. In the first approach, it is assumed that the liquid volume, which is available for backflow, is not removed completely and liquid is continuously flowing through the wire.

The implementation of the backflow into the model requires the consideration of different flow situations. In the standard case, water flows through the fiber mat and the wire perpendicular to the surface of the fiber mat. This requires that the exterior pressure, p_e, is smaller than the suspension pressure, p_{sus}. This process is illustrated schematically in FIGURE 4.4 (left). In this case, the filtration resistance is the sum of the filtration resistance of the wire and the fiber mat as defined in equation (4.1). The flow velocity of the liquid, u_f, is negative and different to the velocity of the fiber mat, u_m. Due to the velocity difference between fiber mat and liquid, the fiber mat grows with the velocity $\Delta u_{grow} = u_f - u_m$.

Backflow takes place and a liquid layer is built up, respectively, if the exterior pressure p_e is higher than the suspension pressure, p_{sus}. The drag liquid layer is completely preserved and the void volume of the wire is filled with water. The flow velocity turns to positive values which causes backflow and the liquid penetrates from outside of the wire in between the fiber mat and the wire (FIGURE 4.4 right). The fiber mat does not grow in the case of backflow and it is $u_f = u_m$. A liquid layer between the wire and the fiber mat is built up and the fiber mat is separated from the wire (FIGURE 4.5 right). For simplicity, it is furthermore assumed that the liquid layer has a defined boundary layer to the fiber mat, and the fiber mat is not destroyed due

to the backflow, remaining in its original form. The drag liquid layer and void volume of the wire decrease continuously.

If the exterior pressure, p_e, decreases below the suspension pressure, p_{sus}, the fluid velocity, u_f, is negative and the fluid layer decreases (FIGURE 4.5 left). In this situation, the filtration resistance of the wire is active. After the liquid layer is degraded completely, the fiber mat gets in contact with the wire and the flow resistance returns to the combined flow resistance of the wire and the fiber mat.

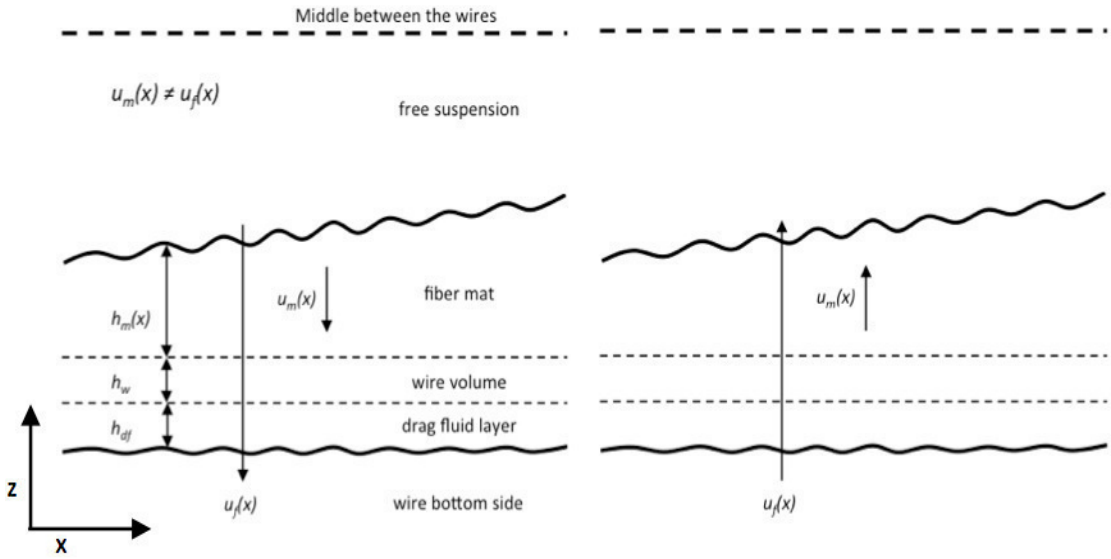

FIGURE 4.4: Schematic illustration of two flow scenarios between the bottom wire and the center of the free suspension. Left: The filtration process at which the fiber mat grows continuously due to the deposition of the fibers in the free suspension area. The fiber mat is in contact with the bottom wire. The liquid flows through both, the wire and the fiber mat. Right: The initial situation of backflow. The drag liquid layer is completely preserved, and the void volume of the wire is filled with water. The fiber mat is still in contact with the wire.

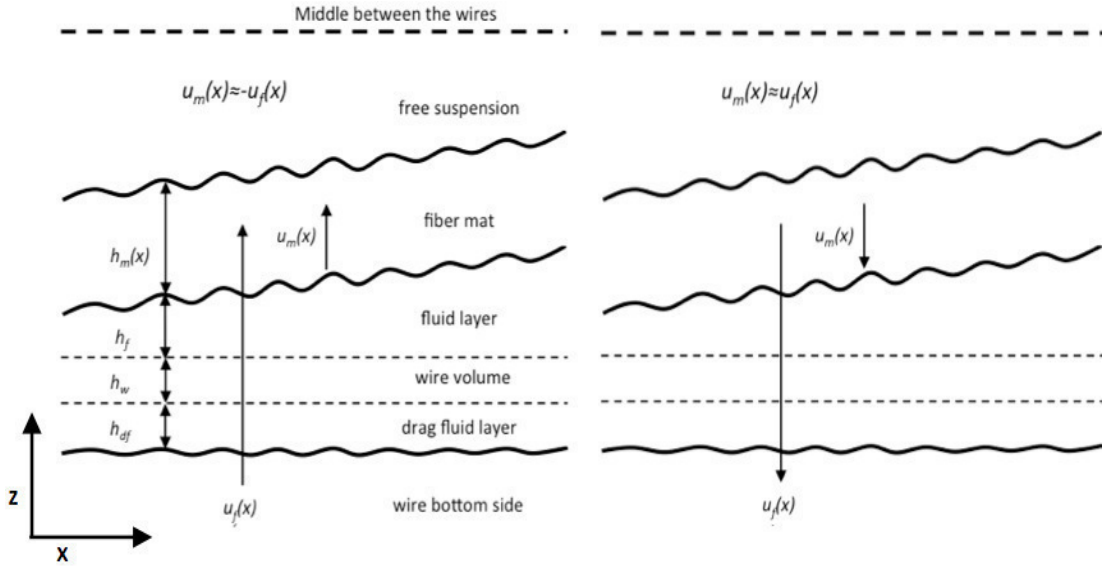

FIGURE 4.5: A schematic representation of two flow scenarios at which the height of the liquid layer increases and decreases: The liquid flows from outside of the wire to the inside. Left: A liquid layer separates the fiber mat from the bottom wire. The flow direction is from the outside to the inside of the wire. It is assumed that the fiber mat and the liquid layer have approximately the same flow velocity. Right: The liquid layer is fully formed and the fiber mat is separated from the wire. Due to the negative flow direction the fluid layer decreases.

These flow scenarios determine the filtration resistance depending on flow velocity and flow direction:

$$R_{tot}(x) = \begin{cases} R_w(x) + R_m(x), & h_f < 0, u_f > 0 \\ R_w(x), & h_f < 0, u_f < 0 \\ R_w(x), & h_f > 0, u_f < 0 \\ R_w(x), & h_f > 0, u_f > 0 \end{cases} \quad (4.3)$$

It is assumed here that the filtration of the fiber mat increases monotonically. This assumption is not known a priori since the backflow could locally reach pressure peaks, which exceed the network strength of the fiber mat. The result could be the destruction of the fiber mat and a homogenization of the concentration in y-direction. In that case, the filtration resistance would probably decrease locally and a new fiber mat would be formed.

The crucial factors for the destruction of the fiber mat are the deflection and the elongation, due to a water layer locally building up. Elongation is a function of the thickness and the width of the water layer. Whether an elongation of the fiber mat leads to a destruction at a given water layer mainly depends on the length of the fibers,

the distribution of the elongation at the numbers of fiber-fiber contacts, and the strength of fiber-fiber bonding. This topic is not a part of this work. For the sake of simplicity, it is assumed that the network is not destroyed.

The mass of the wires and the fiber mats

In order to consider the backflow process in the model, the mass of the suspension layer, fiber mat, and water layer are calculated. Every layer is considered as a single medium and has sharp boundaries to its neighboring layers. The continuity equation for the changing rate of the mass of the fiber mat m_m, of the liquid layer, m_f, and the height, h_m and h_f, respectively, is created. In FIGURE 4.6, a segment of a wire is illustrated in a Cartesian coordinate system. The abscissa represents the machine direction and the ordinate represents the build up of the single layers. The position of the bottom wire is defined as $f(x,y)$, that of the upper wire as $g(x,y)$. The wire is considered to be inelastic. Thus, the wire velocity U is constant. The velocity at a specific point of the suspension is $\mathbf{u}_s$, and the velocity of the wire $\mathbf{u}_w$. The velocity components of the wire and the suspension in x- and y-direction are u_w, w_w and u_s, w_s, respectively. The orientations normal and tangential to the wire are defined by $\hat{n}$ and $\hat{t}$. The definition of the velocity components is mathematically described as follows:

$$\begin{aligned} \boldsymbol{\nabla}\mathbf{u}_\mathbf{w}(\hat{t},\hat{n}) &= 0 \\ \boldsymbol{\nabla}\mathbf{u}_\mathbf{m}(\hat{t},\hat{n}) &= 0 \end{aligned} \tag{4.4}$$

$$\begin{aligned} \boldsymbol{\nabla}\mathbf{u}_\mathbf{w}(\hat{t},\hat{n}) &= \hat{t}w_w + \hat{n}u_w \\ \boldsymbol{\nabla}\mathbf{u}_\mathbf{m}(\hat{t},\hat{n}) &= \hat{t}w_s + \hat{n}u_s \end{aligned} \tag{4.5}$$

The suspension and the wire have the same velocity in x-direction. Thus, it is:

$$\hat{t}w_s + \hat{t}w_w = U \tag{4.6}$$

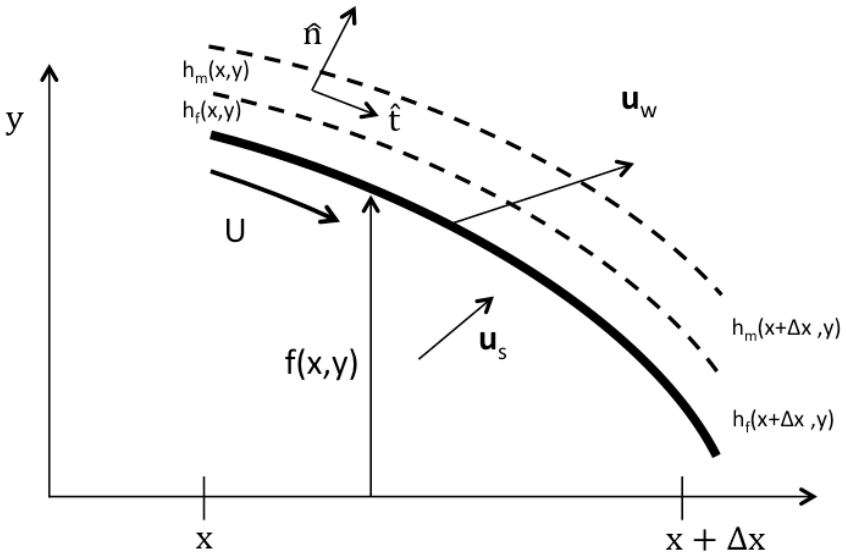

FIGURE 4.6: The buildup of the respective layers at a wire segment of the bottom wire. The segment is defined from x to $x + \Delta x$. The notations of the parameters are given in the text.

The mass continuity equation for a control volume is defined between x and $x + \Delta x$. The change rate of the mass of fibers, m_m, in x- and y-direction can be expressed as follows:

$$\begin{aligned}\frac{d}{dt}\int_x^{x+\Delta x} m_m(x', t)\, dx' \\ = (Uc_{sus}y|_x - Uc_{sus}y|_{x+\Delta x}) \\ - \left(uc_{sus}\Delta x|_{y=1} - uc_{sus}\Delta x|_{y=0}\right)_i\end{aligned} \tag{4.7}$$

Where c_{sus} is the concentration of the suspension, u, is the velocity of the suspension in x-direction and, U, is the wire velocity. Integrating equation (4.7) the continuity equation of the mass becomes:

$$c_{mat_i}\frac{d(uh_{m,i})}{dx} = u_i(x)c_{sus_i}R_i \tag{4.8}$$

The parameter, c_{mat}, is the concentration of the fiber mat, h_m, is the height of the fiber mat and R is the flow resistance of the fiber mat. The mass of the wire, the mass of the liquid in the void volume of the wire, and the mass of the liquid in the fiber mat are not included in the conservation equation.

The equation for the conservation of the water, which flows from the outside to the inside of the wire, is given by

$$\frac{d}{dt}\int_{x}^{x+\Delta x} m_f(x',y)\,dx' = (U\rho_f y|_x - U\rho_f y|_{x+\Delta x}) - \left(u\rho_f \Delta x|_{y=1} - u\rho_f \Delta x|_{y=0}\right)_i. \tag{4.9}$$

By integrating equation (4.9) and transferring the mass to the height of the liquid layer by $h = \frac{\dot{m}}{\rho_f ub}$, equation (4.9) becomes:

$$\frac{d(uh_{f,i})}{dx} = -u_i(x). \tag{4.10}$$

The flow direction of the liquid, and thus the actual condition of the flow direction, depends on the algebraic sign of the pressure loss. A negative pressure loss corresponds to a positive flow direction in the case of the bottom wire, leading to backflow. If the pressure loss is positive, the flow direction is negative, leading to drainage. Depending on these two scenarios, the fiber mat and the water layer behave differently. For the fiber mat, the following cases exist: either the fiber mat grows in the case of a negative flow direction or the fiber mat height is constant in the case of positive flow direction. This behavior results from the assumption that there is no degradation of the fiber mat, i.e. the fiber mat height can only grow or remain constant. This is based on the assumption that the fiber-fiber bonds and the cross-linking of the fibers in the network withstand the forces which lead to a separation of the fibers. The change of the fiber mat height, dh_m, is mathematically expressed by the following case-by-case study:

	$u_f < 0$	$u_f \geq 0$
$h_f < 0$	$dh_m > 0$	$dh_m = 0$
$h_f \geq 0$	$dh_m = 0$	$dh_m = 0$

TABLE 4.1: Case-by-case study for the fiber mat heigth dh_m.

The height of the water layer can increase or decrease. If the flow velocity is positive, the water layer grows at the lower wire. This occurs in the case of the initial situation of backflow, in which no water layer exists, and in the case of an already existing water layer, which then gets thicker. On the other hand, the decrease of the

water layer height takes place if the flow velocity is negative or a water layer exists. This case dependent description for the change of the water layer height dh_f is mathematically expressed as follows:

	$u_f \leq 0$	$u_f > 0$
$h_f \leq 0$	$dh_f = 0$	$dh_f > 0$
$h_f > 0$	$dh_f < 0$	$dh_f > 0$

TABLE 4.2: Case-by-case study for the fluid layer height dh_f.

The momentum of the wires and the fiber mats

Holmqvist (2002) used in his work the momentum equation in the following form:

$$p(x) - p_{e,i}(x) + T_i \cdot \frac{d^2 y_i}{dx^2} = 0 \tag{4.11}$$

Where p is the suspension pressure, p_e is the exterior pressure and T the wire tension. The subscript i indicates the upper and lower wire respectively. This equation is extended in this work, which is explained in this section.

Another source of backflow is caused by the water layer on the outside of the wire, which impinges the blade. Depending on the shape of the blade edge the flow is deflected towards the wire or towards the blade. This results in a stagnation point with a stagnation pressure, which expands to the surrounding elements. The shape of the blade edge determines the part of the stagnation pressure that acts on the wire. This part is called doctoring pressure. The simulation results of Roshanzamir et al. (1999) show that the doctoring pressure, p_d, can exceed the suspension pressure, p_{sus}. Consequently, the condition for backflow is fulfilled and water is pressed into the wire. Green & Kerekes (1998) developed an analytical solution for the two-dimensional problem in order to determine the doctoring pressure:

$$p_d(x) = c_1 p_0 \exp\left(\frac{c_2 x}{h_w}\right) \tag{4.12}$$

where c_1 and c_2 are constants. Green & Kerekes (1998) assumed that c_1 and c_2 are unity. The stagnation pressure $p_0 = \rho V_0^2/2$, where V_0 is the wire speed and ρ the density of the water adhering to the wire. The forces balance (4.11) must be expanded by an additional term, p_d, for the defined distance right in front of the blade and on

the blade side. Orientated on the results of Green & Kerekes (1998), in this analysis, the distance at which p_d is present is 2 mm in front of the blade.

$$p(x) - p_{e,i}(x) + p_d(x_{n-2mm}) + T_i \cdot \frac{d^2 y_i}{dx^2} = 0 \tag{4.13}$$

where x_n represents the end of the free wire module.

The flow of the suspension

The continuity equation

$$u\frac{du}{dx} + \frac{1}{\rho} \cdot \frac{dp}{dx} = 0 \tag{4.14}$$

describes the flow of the suspension for a one-dimensional approach and is derived from the Navier-Stokes equation relating to the x-direction for the momentum for an incompressible fluid. The viscosity is not taken into account in equation (4.14) and it is assumed that stationary flow dominates. The velocity, u, and the pressure, p, are only functions of x, and independent of the z-direction. A detailed derivation of equation (4.14) is given by Holmqvist (2002). Due to the small velocity in z-direction, the momentum is neglected. The continuity equation

$$\frac{d(u \cdot (f-g))}{dx} = \left(\frac{p - p_{e,i}}{R_i} + \frac{p - p_{e,i+1}}{R_{i+1}}\right) \tag{4.15}$$

is integrated in y-direction. The variable f is the position of the upper wire, and the variable g is the position of the lower wire. The left term describes the accumulation of the mass and the right term governs the flow through the wire. The complete derivation of the continuity equation is given by Holmqvist (2002).

Wire release point at the forming roll

The model includes the calculation of the release point of the wire on the forming roll. The exact description of the release point is not trivial. Due to simplifications, the position of the upper and bottom wire can be estimated. This position of the wire on the roll side depends on the forces that keep the wire on the surface of the roll. These forces increase in the x-direction, due to an increasing deviation from the natural path between the forming roll and the blade position. A schematic illustration of the modeled section is shown in FIGURE 4.7. The forming roll has the radius, R, and the

surface of the roll is described by the function $s(x)$. For a constant distance between the wires, the upper and the bottom wire would follow the path $\bar{g}(x)$ and $\bar{f}(x)$, respectively. Under this condition the release point, $\bar{x}$, would be at the center of the roll. Because of the vacuum between the forming roll and the bottom wire, the wire gets curved in direction of the forming roll. This natural path, which is indicated by $\tilde{g}(x), \tilde{f}(x)$, is blocked due to the position of the forming roll that is denoted by $s(x)$. At the intersection point between $\tilde{g}(x)$ and $s(x)$, the new web release point, $\bar{x}$, can be determined between $\tilde{x}$ and $\tilde{x} + S$. If the new release point is defined, the path of the upper and lower wire $g(x)$ and $f(x)$ are specified.

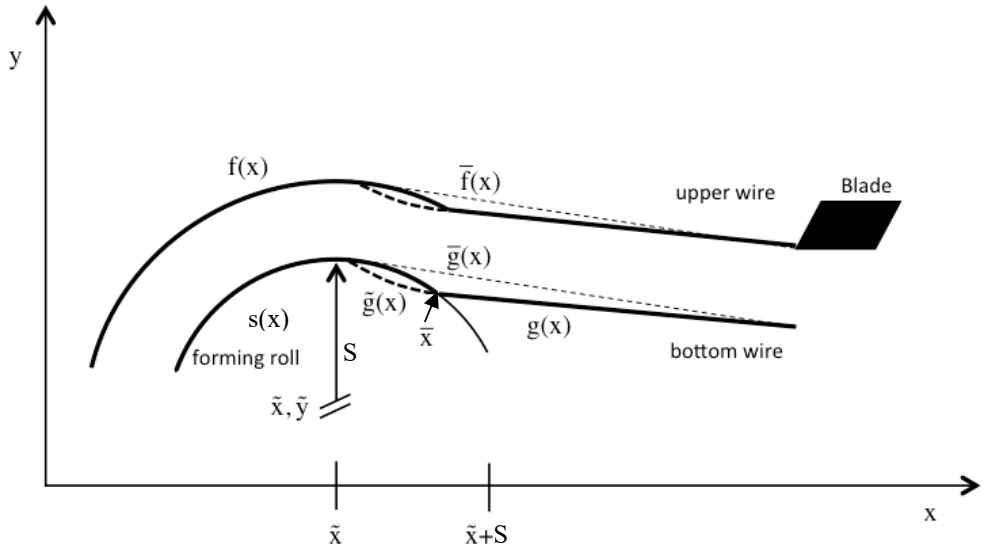

FIGURE 4.7: Schematic illustration of the modeled section from the natural release point at the forming roll to the first blade. The wire path with forces $(\bar{g}(x), \bar{f}(x))$ and without the acting forces $(g(x), f(x))$ are shown. The effective release point, $\bar{x}$, is calculated by the model.

The theoretical position of the bottom wire $\tilde{g}(x)$ is calculated by equation (4.15). The effective path of the bottom wire $g(x)$ is determined by a maximum function, where $x \in (\tilde{x}, \tilde{x} + S)$. At $\bar{x}$ upstream, it is $g(x) = \tilde{g}(x)$. Mathematically, these constraints can be expressed as follows:

$$g(x) = \begin{cases} \max\{s(x), \tilde{g}(x), & x \in (\tilde{x} \leq x < \tilde{x} + S)\} \\ \tilde{g}(x), & x \geq \tilde{x} + S \end{cases} \tag{4.16}$$

$$\bar{x} = \min\{x \in (\tilde{x}, \tilde{x} + S) : g(\bar{x}) = \tilde{g}(x)\} \tag{4.17}$$

4.2.3 The Model

The model equations for the wire section between the forming roll and the first blade are derived in section 4.2.2. A complete overview of the used equations in the model is given below.

$$R_f(W_f) = a_{1,f} W^{a_{2,f}} \tag{4.18}$$

$$R_g(W_g) = a_{1,g} W^{a_{2,g}} \tag{4.19}$$

$$c_{mat_f} \frac{d(uh_{m,f})}{dx} = u_f(x) c_{sus_f} R_f \tag{4.20}$$

$$c_{mat_g} \frac{d(uh_{m,g})}{dx} = -u_g(x) c_{sus_g} R_g \tag{4.21}$$

$$\frac{d(uh_{fl,f})}{dx} = -u_f(x) \tag{4.22}$$

$$\frac{d(uh_{fl,g})}{dx} = u_g(x) \tag{4.23}$$

$$\frac{d(u \cdot (f-g))}{dx} = \left(\frac{p - p_{e,f}}{R_f} + \frac{p - p_{e,g}}{R_g} \right) \tag{4.24}$$

$$u \frac{du}{dx} + \frac{1}{\rho} \cdot \frac{dp}{dx} = 0 \tag{4.25}$$

$$p - p_{e,f} + p_d(x_{n-2mm}) + T_f \cdot \frac{d^2y}{dx^2} = 0 \tag{4.26}$$

$$p - p_{e,g} + p_d(x_{n-2mm}) - T_g \cdot \frac{d^2y}{dx^2} = 0 \tag{4.27}$$

Equation (4.18) and (4.19) govern the local flow resistance for the upper and lower wire. Equation (4.20) and (4.21) are the mass continuity equation for the upper and lower fiber mat. Equation (4.21) differs from the general equation (4.8) in the sign of the flow velocity. In the lower wire dewatering occurs at a negative flow velocity. The accumulation of the liquid layer is governed by (4.24) and (4.25). The liquid layer at

the lower wire increases at a positive flow direction. Therefore, the sign of the flow velocity in equation (4.25) differs from the general description in (4.10). The mass balance is shown in equation (4.24). The term of the left side describes the accumulation of the mass and the term of the right side governs the flow through the wire. The momentum balance for the one-dimensional flow is governed by equation (4.25). Equation (4.26) and (4.27) describe the deflection of the upper and lower wire. Due to the fact that the forces at the lower wire act in the reversed direction, the sign changes.

4.3 Numerical algorithm

4.3.1 Verification

To study the convergence rate, the model is validated by a grid dependent analysis. For this purpose, the simulation is carried out with a different number of mesh points. FIGURE 4.8 shows the simulation results for a grid width Δx of 1.22mm, 2.5mm and 5mm along the model domain l. The differences between 1.22 mm and 2.5 mm are close to zero for almost the entire section. It can be concluded that the grid independence can be reached below a Δx of 2.5 mm.

To evaluate the convergence rate, the same simulation is evaluated for different grids. The result at an x-position of 0.143 is taken to compare the errors between the simulation results at different mesh points. At this position there is the highest pressure gradient and thus the influence of the grid width is high.

$$e_p = \frac{p(\frac{l}{\Delta x})}{p_0} \tag{4.28}$$

To calculate the error e_p a reference mesh grid with a Δx of 0.75 mm is considered as the exact solution p_0. The result of the error versus the sampling of the mesh is shown in FIGURE 4.9.

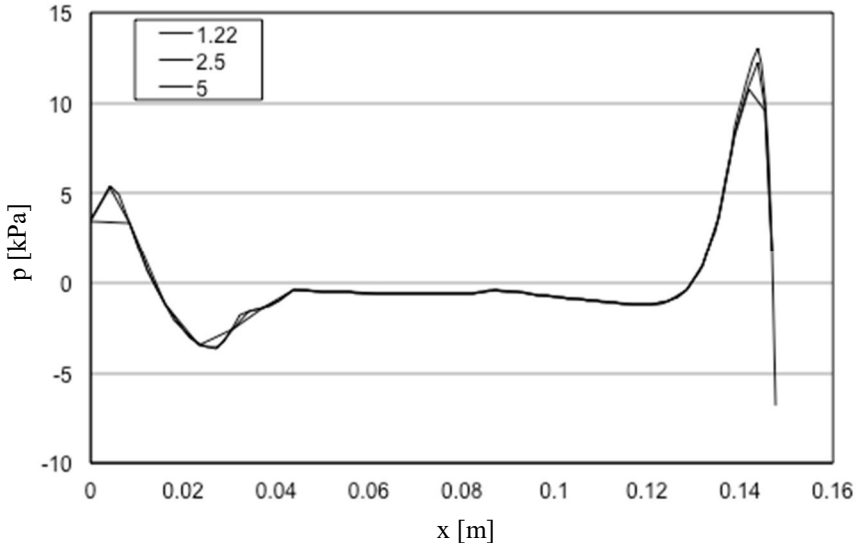

FIGURE 4.8: Simulation results of the grid dependence study. The calculation was done at module length l/Δx of 1.22, 2.5 and 5. At maximum and minimum values, the graphs differ by more than 20%.

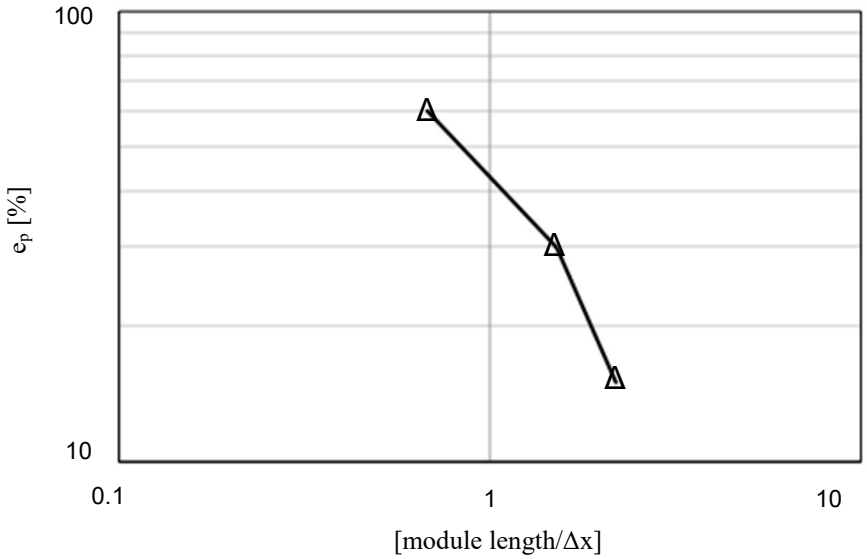

FIGURE 4.9: Convergence rate of the internal pressure. The error e_p is determined at the x-position 0.143m. It is assumed that the exact simulation results are achieved by a grid of 200 nodes.

4.3.2 Validation

The simulation results are validated by pressure measurements in an industrial double wire former. These measurements were carried out by Schmidt-Rohr (2007). The method was also used by Gooding et al. (2004). They used a capillary tube which is inserted into the gap between wires. In FIGURE 4.10, the simulation and the measurements of the pressure profile are shown in comparison. The geometric boundaries of the simulation fit to the geometry of the former at which the measurements are carried out. The initial value for the flow resistance is $2 \cdot 10^6$ kNs/m^3, which corresponds to a basis weight of 15 g/m^2 for a newsprint pulp. The initial gap size is set to 3 mm. Both numbers are calculated by the amount of water, which is drained at the forming roll during the process trials. The machine speed and the wire tension are set to 1200 m/min and 8000 N/m respectively. The simulation results show a good agreement with the measurement results.

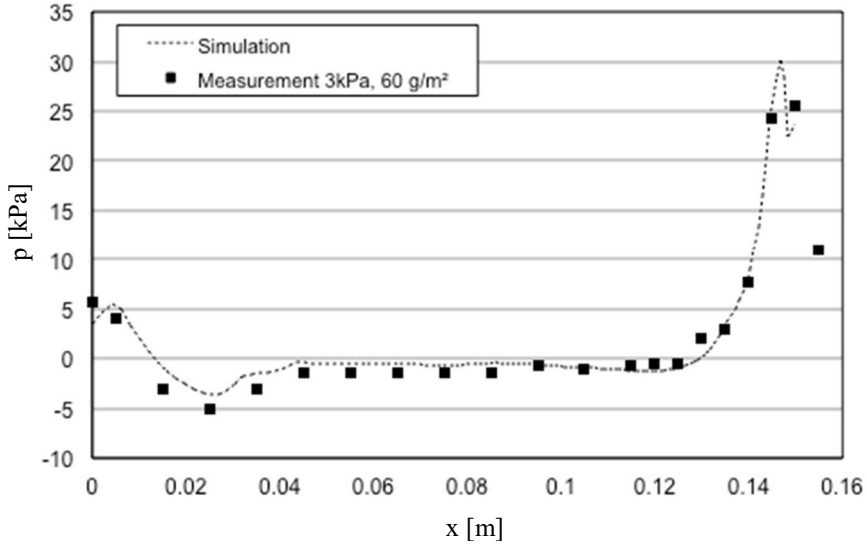

FIGURE 4.10: Validation of the simulation results. The simulation results match the measurement of the internal pressure along the entire simulated spatial domain.

4.4 Results

In this Chapter, the model in section 4.2.3 was used to calculate the internal pressure, the flow velocity of the liquid, the position of upper and lower wire and the height of the liquid layer at different machine settings. In the simulation the parameter wire speed, the wire tension, the wire resistance and the initial gap size was varied.

4.4.1 Influence of the backflow concept on the simulation results

In their simulations, Holmqvist (2002), Zhao & Kerekes (1996), and Zhao & Kerekes (1995) observed an oscillation behavior at a high flow resistance. The hypothesis was that, due to the backflow function of the model and a flow-direction-dependent flow resistance, the oscillation tendency could be reduced. To analyze the influence of backflow, simulations with and without backflow were carried out. The results are shown in FIGURE 4.12 (left).

Zhao & Kerekes (1996) mention that pressure oscillations occur during the simulation as soon as a critical flow resistance value of 67 kNs/m^3 is reached. A similar value was determined by Zahrai & Bark (1995). They mentioned that oscillation behavior could be avoided by reducing the flow resistance. In the presented work, a simulation was carried out at a flow resistance of 700 kNs/m^3, which corresponds to a basis weight of 30 g/m^2 for a Newsprint pulp. The results are shown in FIGURE 4.11 and FIGURE 4.12, indicated by the solid line. As expected, the simulation results for the pressure with the model of Zhao & Kerekes were oscillate significantly, and with high amplitudes. Zahrai & Bark (1995) proposed that this oscillating behavior might be caused by capillary waves. In contrast to that, a simulation was carried out with backflow and a flow-direction-dependent flow resistance. In those sections where backflow occurs, the flow resistance of the wire is present. In cases in which dewatering occurs, the flow resistance increases. In these areas the combination of the flow resistances of the wire and the fiber mat is present. The results of the simulation are represented by a dotted curve in FIGURE 4.11 (left), and the boundary conditions are the same as in FIGURE 4.10. Comparing both curves it is evident that the implementation of backflow and a direction-dependent flow resistance reduces the tendency for oscillations. This can be explained by the fact that, at the upper wire, backflow occurs, and thus the flow resistance is reduced significantly. FIGURE 4.12 shows the simulated results of the liquid layer at the upper and lower wire. At the upper wire, a liquid layer covers the entire model domain predominantly. In this domain, only the flow resistance of the wire is present, which is assumed to take a value of 21 kNs/m^3.

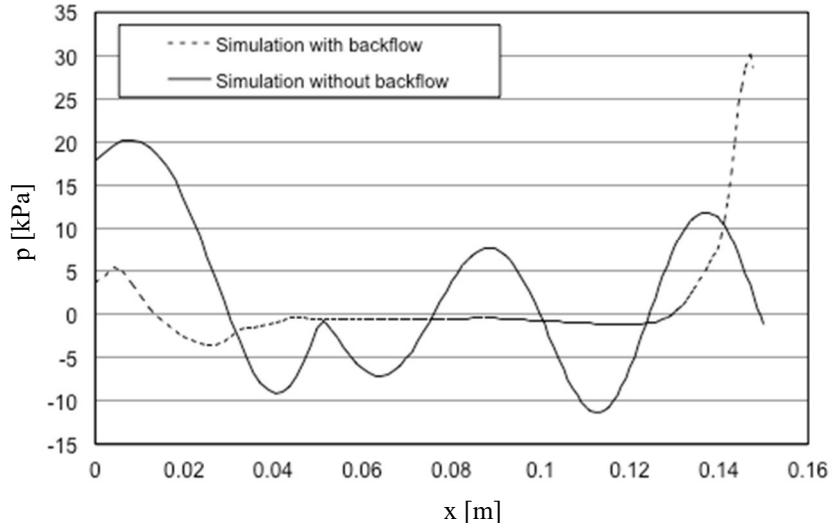

FIGURE 4.11: Comparison of the pressure profile of a simulation with backflow and flow-direction-dependent flow resistance to the model of Holmqvist (2002) with a constant flow resistance that is independent of the flow direction.

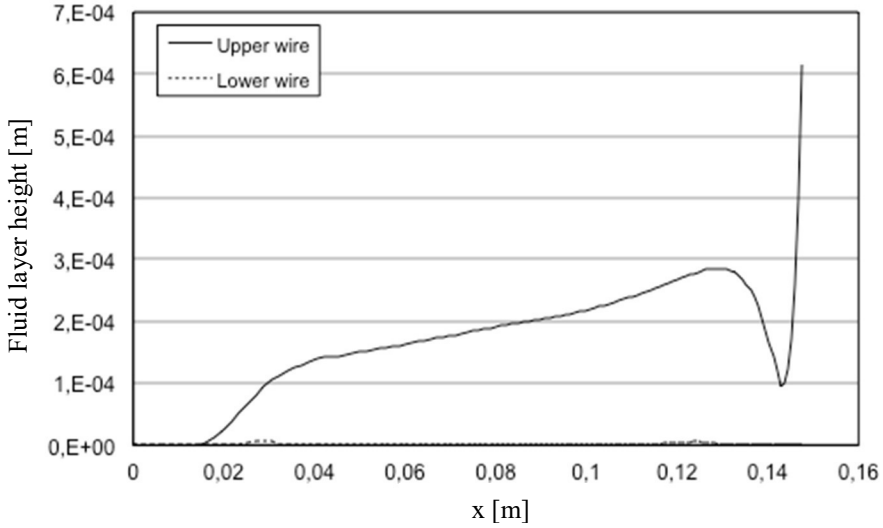

FIGURE 4.12: The fluid layer of the upper and lower wires.

4.4.2 Analysis of free wire length

FIGURE 4.13 and FIGURE 4.14 show the simulation results for the wire release point at the forming roll and the free wire segment. In FIGURE 4.13, the internal

pressure starts at a level of 5.5 kPa. This level corresponds to an approximation of the pressure of $\frac{T}{S} - p_e$. Dalpke (2004) showed a similar relationship for the maximum pressure at the forming roll. At the release point of the wire, the pressure decreases to -3.6 kPa at an x-position of 0.026 m. Beneath this position, at the gap between the forming roll and the bottom wire, a suction pressure is assumed. By means of a pressure transducer, Holm (2002) measured values between -2 to -4 kPa on the surface of the forming roll. Because of simplicity, a suction pressure of -3 kPa is assumed up to the position of 0.043 m in x-direction. At an x-position of 0.026 m, the pressure increases to -0.5 kPa for the distance at which the exterior pressure at the bottom wire is -3 kPa. After reaching the local maximum between the x-positions 0.02 through 0.09, the pressure remains almost constant. The exterior pressure at the outside is assumed to be -1 kPa. At the end of the unsupported wire, the doctoring pressure leads to a pressure peak up to 13 kPa. The doctoring pressure is assumed to increase from -1 kPa to 60 kPa and acts at the outside of the upper wire through a distance of 0.004 m.

FIGURE 4.13 represents the gap between the bottom and the top wire. The gap decreases to an x-position of 0.02m, which indicates that the wires are compressed. After the minimum is reached, the results show a significant broadening of the gap. As the pressure levels indicate, the wires are pulled apart from each other. The reasonable explanation for this is that the pressure in the vacuum at the bottom wire pulls the wire to the surface of the roll. The upper wire is stretched in transversal direction and withstands certain deformation forces in normal direction, whereby the wire distance increases. From an x-position of 0.03 up to 0.135 m, the gap further grows and reaches its maximum expansion at 0.137 m. The characteristics of the pressure and the gap curve are similar. The simulation results confirm the observations of Schmidt-Rohr (2007) that after the forming roll, the wires are pulled apart from each other.

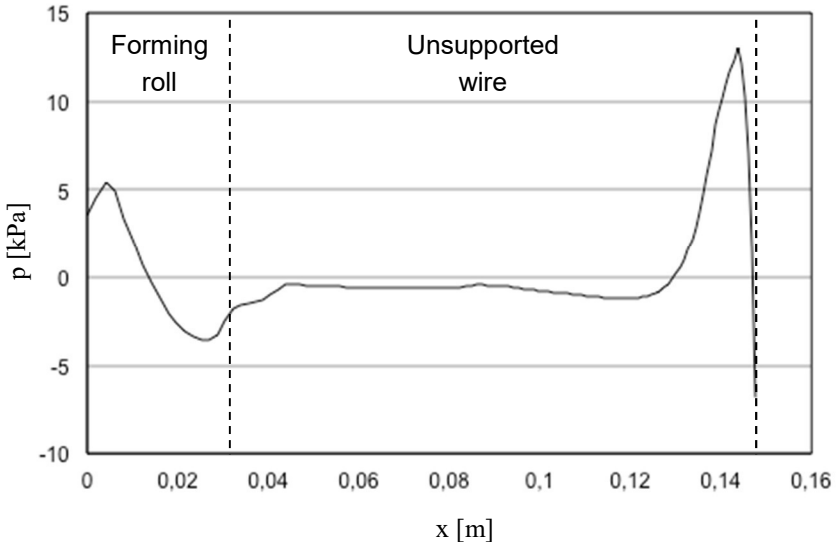

FIGURE 4.13: The pressure distribution at the release point of the wire from the forming roll, and the free-wire segment from the forming roll downstream to the blade.

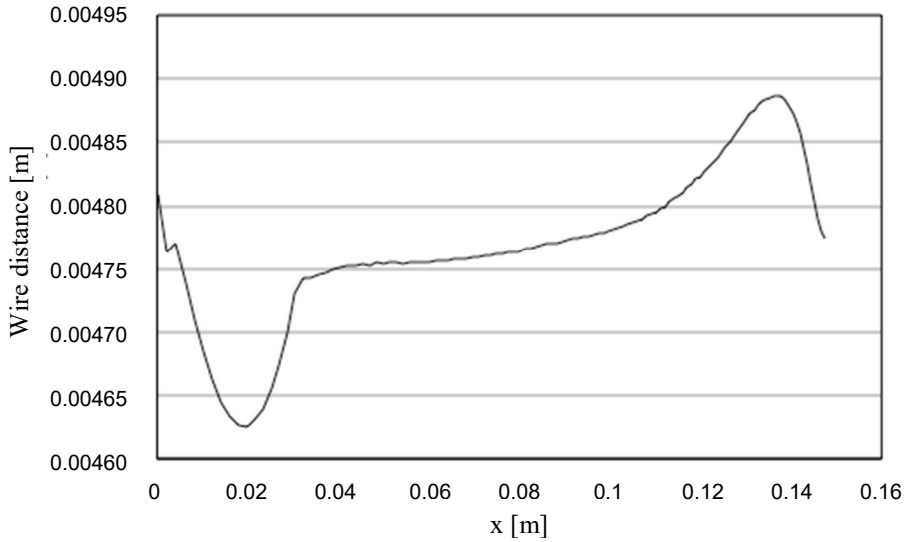

FIGURE 4.14: Corresponding to FIGURE 4.13: distance between the upper and lower wire. For the predominating distance of the segment, the wires are pulled apart from each other.

In FIGURE 4.15, the difference pressure between the pressure in the middle of the suspension and the exterior pressure is shown. The difference pressure defines the direction and the flow velocity of the medium, which is shown in FIGURE 4.16. The flow velocities of the upper and lower wire are defined in a Cartesian coordinate system. This means that a negative flow velocity at the upper wire leads to a backflow of the fluid from the outside to the inside. A negative flow velocity at the bottom wire leads to a flow from the gap between the wires to the outside of the bottom wire.

The simulation results in FIGURE 4.15 show that the pressure at the upper wire is significantly below ambient pressure, and the distance at which negative pressure acts ranges from 0.014 to 0.129 m in the x-direction. After this distance, the pressure increases and shows two peaks. The first peak is generated by the wire curvature directly in front of the blade. The second peak has its origin in the doctoring pressure, which reaches its maximum at the end of the unsupported wire. The height of the pressure peak is determined by the stagnation pressure. In contrast to that, the lower pressure reaches a ambient pressure only at a small distance of 0.023 to 0.12 m and in the very end of the free wire segment in x-direction. In these areas, the flow velocity is positive, which means that backflow occurs (FIGURE 4.16). The flow velocity at the upper wire is predominantly negative, which causes backflow. The effect on the liquid layer, which is formed, is shown in FIGURE 4.17. The lower wire shows two peaks, which are not significant compared to the height of the upper wire. These formed liquid layers are removed completely when the flow velocity turns to negative values. In case of the upper wire, the liquid layer starts to grow at x=0.018 m and keeps growing continuously up to x=0.13 m. After a short distance at which the layer is reduced, the doctoring pressure becomes effective and the liquid flows from outside of the wire to the inside. The fluid layer increases significantly.

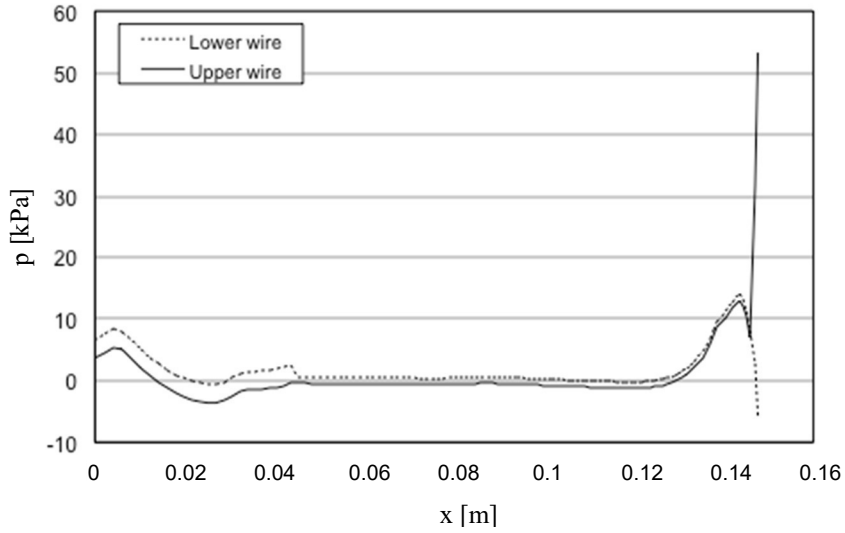

FIGURE 4.15: Simulation results of the pressure loss for the upper and lower wires. The pressure loss of the upper wire is predominantly negative. In contrast to that, the pressure loss of the lower wire is predominantly positive.

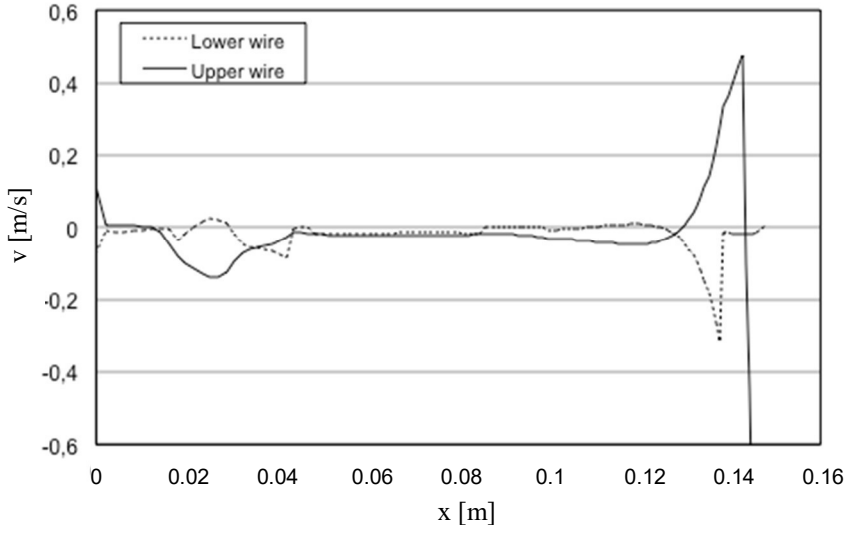

FIGURE 4.16: The flow velocity of the upper and lower wire along the x-direction at the free wire segment. The flow velocities change their algebraic sign whereby backflow occurs.

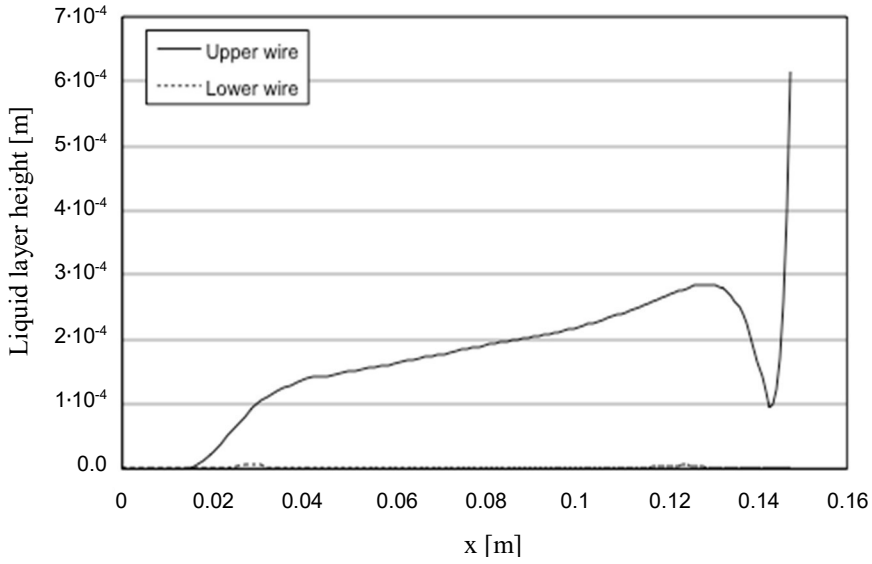

FIGURE 4.17: The development of the liquid layer at the upper and lower wire. At the lower wire, a liquid layer is formed at two regions, both of which get removed completely. At the upper wire, the liquid layer is formed at the beginning of the segment and is preserved along the whole segment.

FIGURE 4.18 displays the simulation results of the position of the upper and lower wire. Additionally, the liquid layers and the fiber mats at both sides are shown. At the upper wire, the liquid layer is formed at approximately half the distance at which the lower wire is guided by the shape of the forming roll. Upstream of this position, the upper wire is shaped in similar ways than the lower wire. Downstream of this position the wire tends to run in a slight curve in the direction of the downstream-positioned blade. This deformation is caused by the force that normally acts on the wire in a negative direction. This force is generated through the negative pressure between the lower wire and the forming roll. As a result, the wire is deformed and deviates from the straight line, from the zero position to the blade downstream which would be formed, if no forces would act. The force, which is needed to deform the wire, increases when the curvature of the wire increases. The deformation of the wire stops when the regular force acting on the wire in negative direction equals the forces in positive direction. This deformation force is determined by the flow resistance, and thus by the pressure loss which is generated by a negative pressure of -3 kPa. Due to the deformation, the concave curvature turns into a convex curvature, whereby the internal pressure turns from positive to negative values.

In case of the lower wire, the force that is responsible for the deformation of the wire is determined by the pressure loss between the wires. Due to the significantly higher values of the filtration resistance, the force which is acting on the wire, is

higher, and thus the deformation is more distinctive. The distance at which the wire takes the shape of the forming roll, is therefore longer. At this region, the pressure loss is positive, whereby the fiber mat grows. When the lower wire leaves the roll, the curvature of the wire turns from convex to concave. The internal pressure decreases below the level of the exterior pressure, whereby a backflow occurs. This condition remains constant for a distance of 0.005 m. The flow velocity turns its direction and the liquid layer is removed completely.

In the region, where the wires are not supported, the liquid layer at the upper wire increases continuously. Consequently, the fiber mat height remains constant. At the lower wire, the fiber mat grows up to the position at which the wire is deformed from convex to concave, and the internal pressure decreases below the level of the exterior pressure. This position is at a position of 0.135 m in x-direction. Due to the low flow velocity, the liquid layer has a height of $5 \cdot 10^{-6}$ m. At this position, the wires are pulled apart from each other before they get compressed just before the blade acts. Directly on the blade, the doctoring pressure leads to a widening of the wires.

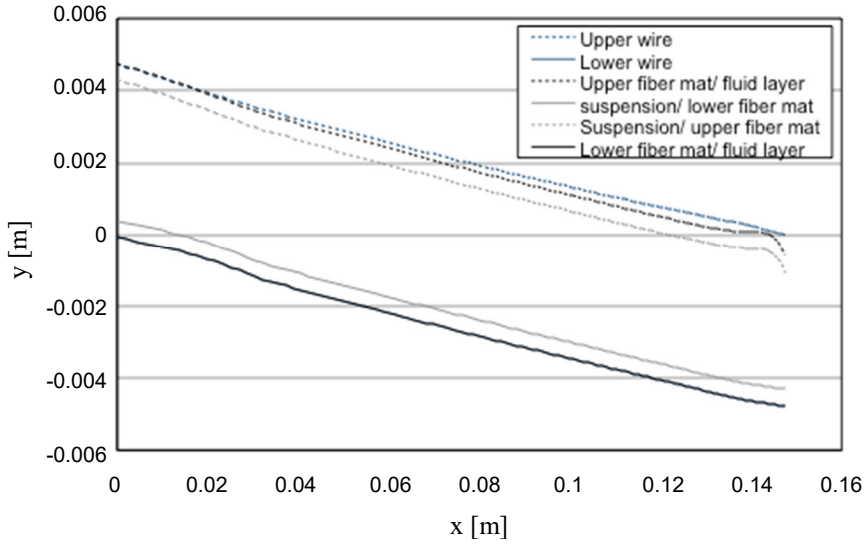

FIGURE 4.18: The position of the upper and lower wire, the boundary between fiber mat and fluid layer and the boundary between suspension and fiber mat at each wire. At the upper wire, a significant liquid layer is formed. In this area, the fiber mat keeps constant. The fiber mat of the lower wire grows although the growth is not significant thanks to the low forces that act along the segment.

4.4.3 Wire speed

FIGURE 4.19, FIGURE 4.20 and FIGURE 4.21 show the internal pressure profile, as well as the upper and lower liquid layer, at two different wire speeds, respectively. The wire speed has an effect on the internal pressure distribution as well as on the liquid layers of the wires. With increasing machine speed, the amplitudes of the internal pressure increase at the section of the forming roll. The pressure increases from approximately 2 kPa up to 5 kPa. The low pressure at the release point is more significant in the case of higher machine speeds. The pressure difference is approximately 1 kPa. As a result, the deflection of the wires and the liquid layer at the lower wire are higher. An increase in the internal pressure due to an increase in machine speed was already observed in the results of Zhao & Kerekes (1995). In contrast to that, the amplitudes of the internal pressure in the center of the model region are not significantly dependent on the machine speed. At low machine speeds, the internal pressure is lower. Directly at the blade, the more distinct wire deflection leads to a significantly lower pressure at higher speeds (15 m/s).

The machine speed significantly influences the development of the liquid layer which is shown in FIGURE 4.20 and FIGURE 4.21. A higher machine speed results in a stronger liquid layer at the release point of the forming roll. At a wire speed of 10 m/s the internal pressure does not drop below atmospheric pressure. Therefore, no liquid layer is formed. In the case of a wire speed of 15 m/s the internal pressure drops below the atmospheric pressure whereby a liquid layer is formed. The lower liquid layer downstream of the segment increases at lower machine speed. The liquid layer at the upper wire starts to grow at the release point of the roll at both wire speeds. At a wire speed of 10 m/s, a significantly thicker layer is formed in comparison to 15 m/s. In both cases the liquid layer decreases significantly at the position x=0.142 m. Further downstream, due to the change of the direction of the wire deflection and the doctoring pressure which acts from the upper wire, the liquid layer at the upper wire increases significantly.

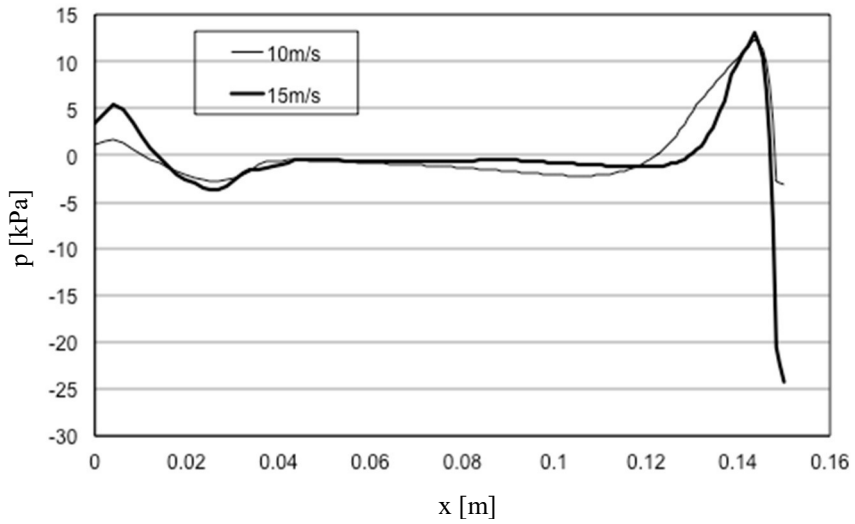

FIGURE 4.19: Influence of variations of machine speed on the internal pressure. An increase in machine speed leads to higher pressure amplitudes at areas in which the external forces act. In areas in which low forces act, the machine speed has no significant influence.

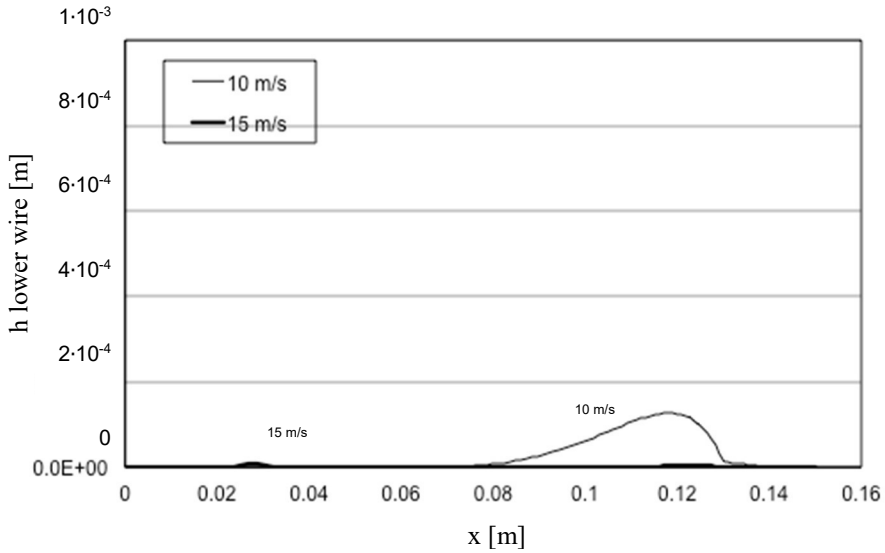

FIGURE 4.20: Left: Liquid layer at the lower wire: The machine speed influences the development of the liquid layer significantly. A higher machine speed results in a higher liquid layer at the release point of the forming roll. The liquid layer downstream of the segment increases at a lower machine speed.

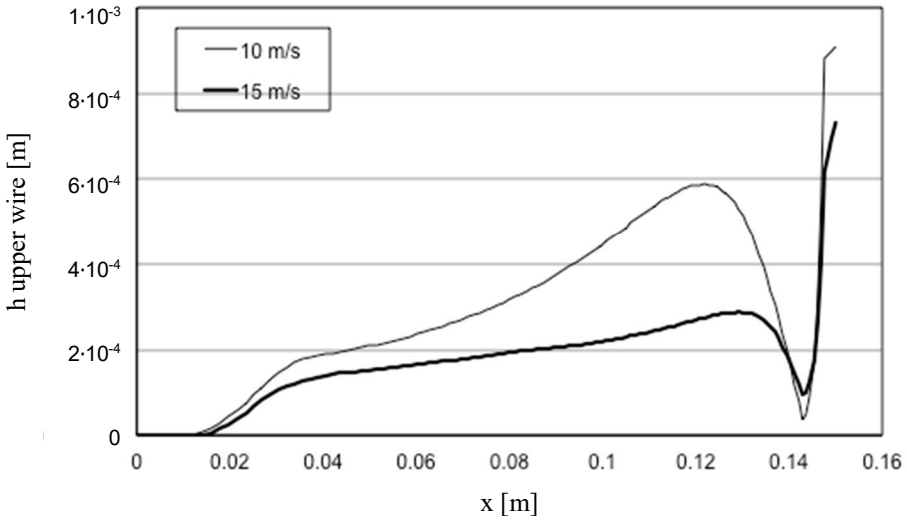

FIGURE 4.21: The liquid layer at the upper wire: The liquid layer starts to grow at the release point of the roll. At 10 m/s, a significantly thicker layer is built in comparison to 15 m/s.

4.4.4 Wire tension

FIGURE 4.22 shows the pressure profile along the model domain. At the positions at which the wire has contact with the forming roll, the pressure is higher for the lower wire tension. In contrast, the pressure is lower at the release point for the lower wire tension. This phenomenon can be explained by the lower forces in transversal direction at a lower wire tension and similar forces in normal direction. This leads to a higher wire deflection and thus to higher pressure amplitudes. Between the x-positions 0.05 and 0.1, both simulated results show a pressure level close to zero. Similar to the pressure gradients upstream of the model, the pressure downstream shows more significant amplitudes at a lower wire tension. The reason for that is a lower force in transversal direction in case of lower wire tension. The movement in normal direction is higher and thus the pressure amplitudes are higher. FIGURE 4.23 and FIGURE 4.24 show the liquid layer of the lower and upper wires at two different wire tensions. The liquid layer is thicker in case of a lower wire tension for the dominant model domain. This behavior can be explained by a higher wire deflection of the wires at low wire tension. In contrast to that, downstream of the model domain the significant decrease of the internal pressure, which is caused by the doctoring pressure, leads to a high thickness of the liquid layer at the upper wire.

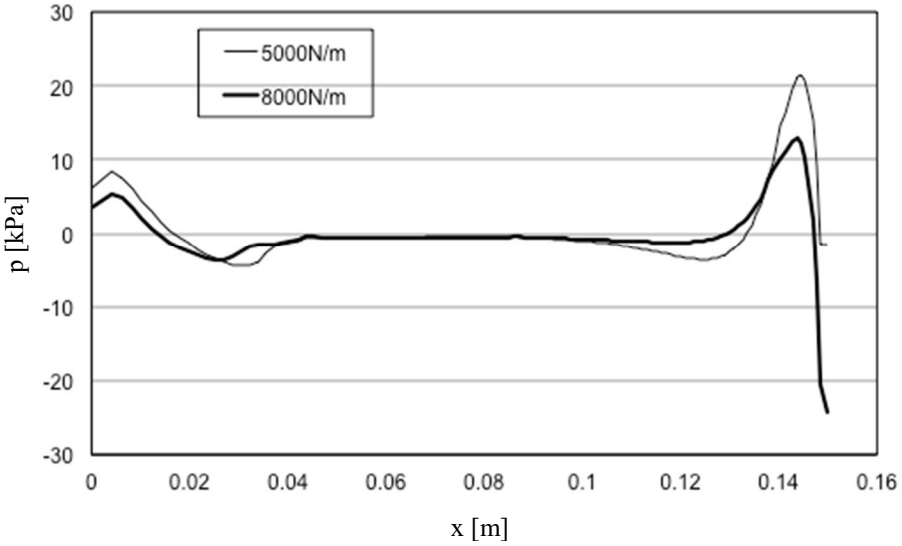

FIGURE 4.22: Internal pressure profile at two different wire tensions. At higher wire tensions, the amplitudes decrease.

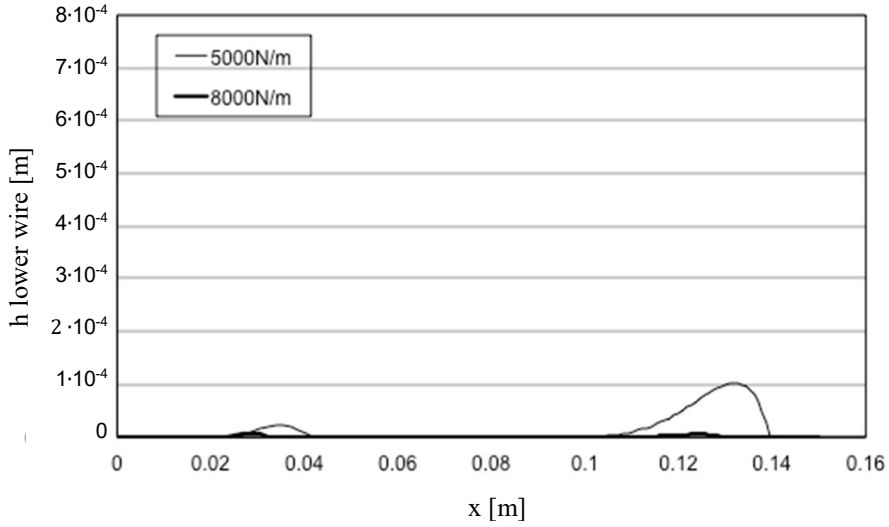

FIGURE 4.23: Liquid layer of the lower wire at two different wire tensions. The liquid layer is thicker in the case of a lower wire tension for the dominant model domain.

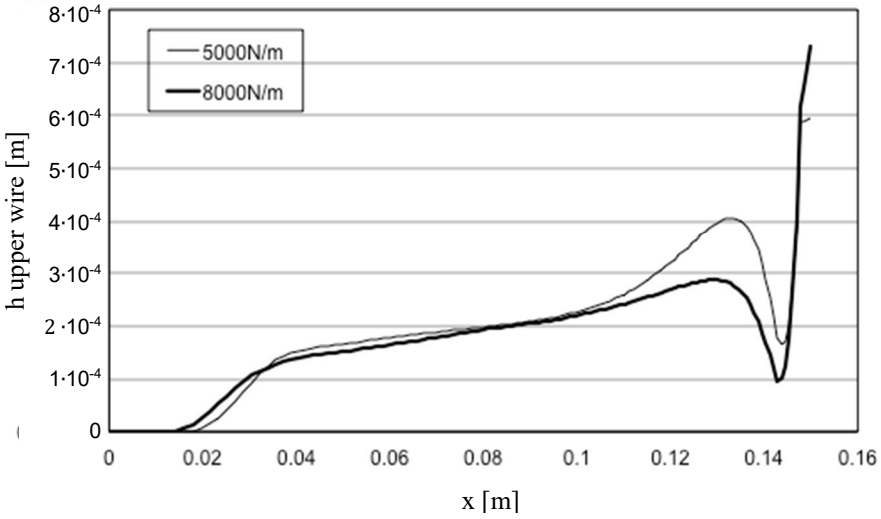

FIGURE 4.24: Liquid layer of the upper wire at two different wire tensions. Downstream of the model domain the significant decrease of the internal pressure, which is caused by the doctoring pressure, leads to a high thickness of the liquid layer at the upper wire.

4.4.5 Wire resistance

FIGURE 4.25 shows the pressure profile along the model domain for two different wire resistances. Up to x=0.06 m the pressures do not differ significantly for both flow resistances. This can be explained by the fact that both the wire and the fiber mat resistance are effective in this area. After x=0.06 m at a flow resistance of 30 kNs/m^3 the amplitudes are more significant. This result seems to be reasonable, since the transfer of forces to the wire decreases with decreasing flow resistance. This lead to a reduction of the wire deflection.

FIGURE 4.26 shows the liquid layer at the upper (right) and lower (left) wire. At the lower wire, the development of the liquid layer is similar in both cases. At position x=0.12 m, the liquid layer at 30 kNs/m^3 reaches a higher level compared to 26 kNs/m^3. At the upper wire, between x=0.05 m and 0.1 m, the liquid layer at higher flow resistance shows a lower liquid layer. In contrast, above x=0.12 m, the maximum liquid layer height is larger at higher flow resistance. Downstream of the domain, the doctoring pressure injects liquid into the wires, whereby the liquid layer increases significantly. FIGURE 4.28 shows the changes in gap height along the model domain at two different wire flow resistances. Downstream of the model domain no significant difference between both wire flow resistances are found. At an x-position of 0.06 m, the gap at higher flow resistances decreases below the second curve and exceeds it

afterwards. At the end of the model domain the gap height is lower than the initial gap height. This means that in total dewatering takes place.

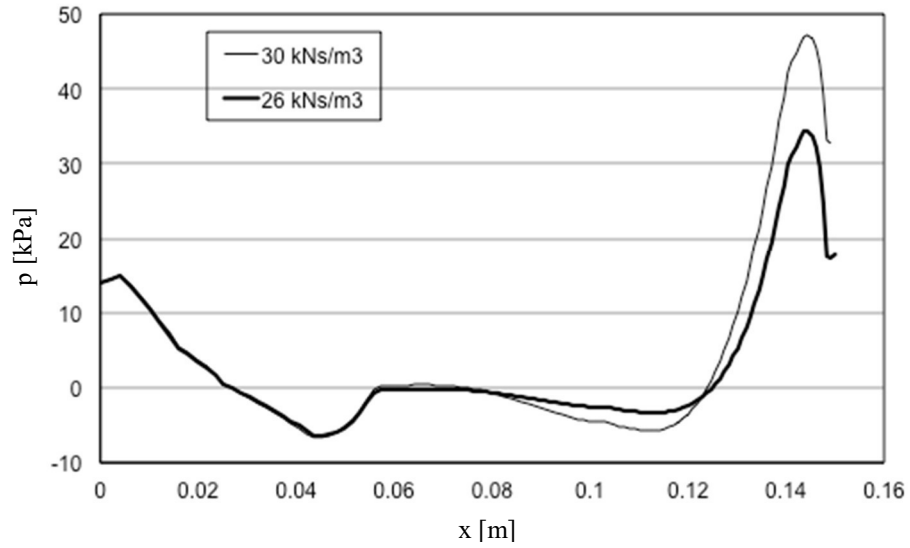

FIGURE 4.25: Pressure profile along the model domain at two different wire resistances. Upstream of the domain there are no differences. Downstream of the model region, the pressure increases with increasing resistance.

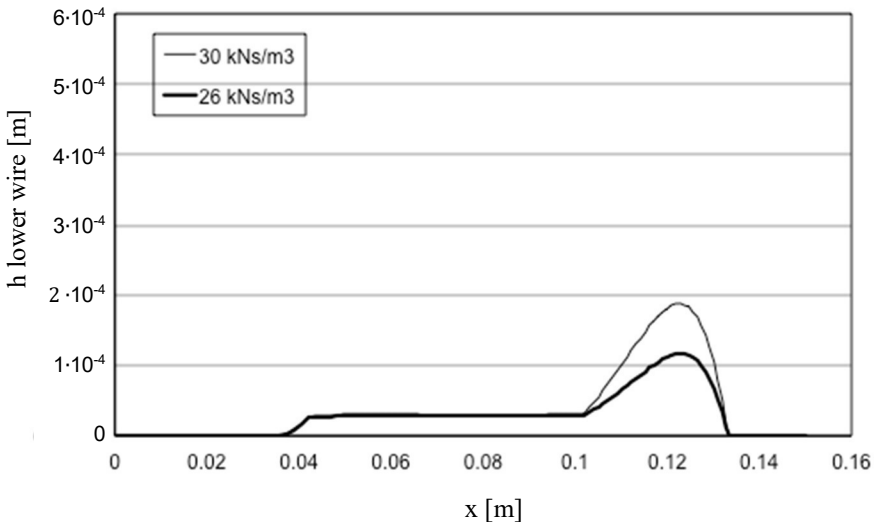

FIGURE 4.26: Liquid layer at the lower wires. At the lower wire the development of the liquid layer is similar in both cases. At position x=0.1 m, the liquid layer at 30 kNs/m^3 reaches a higher level compared to 26 kNs/m^3.

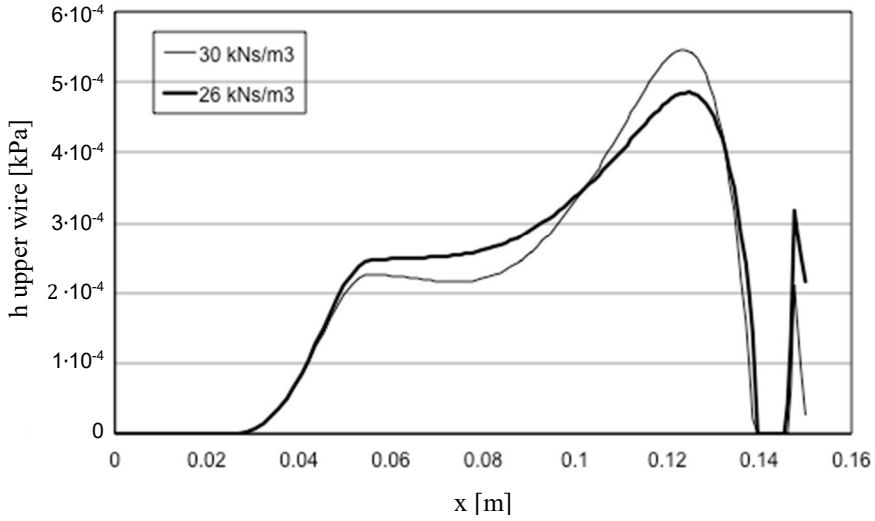

FIGURE 4.27: Liquid layer at the upper wires. Between x=0.05 m and 0.1 m, the liquid layer at higher flow resistance is lower. In contrast to that, above x=0.1 m, the liquid layer at higher flow resistance shows the largest hight. At the end oft he modeling domain, the doctoring pressure injects liquid into the wires, whereby the liquid layer increases significantly.

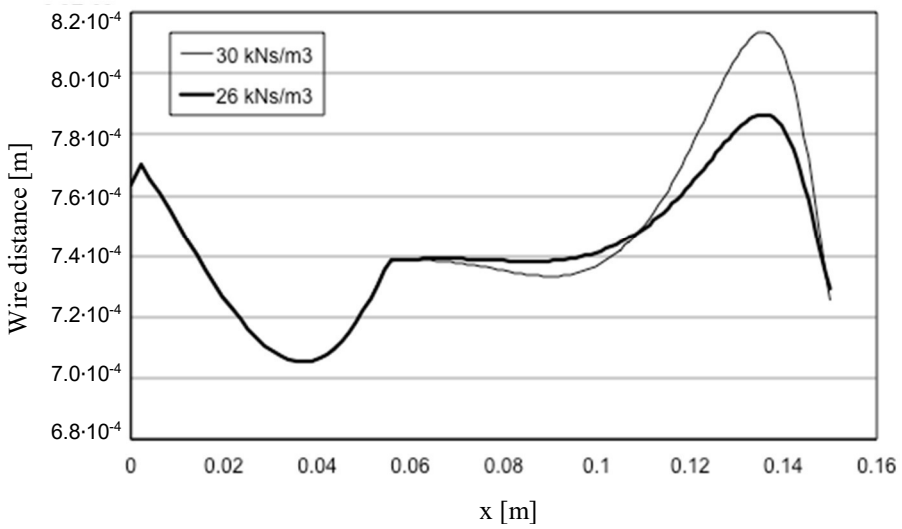

FIGURE 4.28: Gap height along the model domain at two wire flow resistances. Downstream of the model domain there is no significant difference. At an x-position of 0.06 m, the gap height for the higher flow resistance decreases below the gap height for the lower flow resistance and exceeds it afterwards.

4.4.6 Initial gap size

In FIGURE 4.29 the pressure profile along the gap domain for an initial gap height of 0.0047 m and 0.0076 m is presented. The influence of the initial gap size on the pressure profile is obvious. At a higher initial gap height, the pressure is about 7 kPa higher than for the lower initial gap height up to the position of x=0.02 m. Due to a higher gap height the position of the release point changes from approximately 0.03 m to 0.05 m. At the end of the domain the pressure at higher initial gap height is significantly higher than at lower initial gap height. This can be explained by the fact that the liquid layer is completely removed and the flow resistance of the wire and the fiber mat is present.

FIGURE 4.30 and FIGURE 4.31 show the liquid layer at the lower wire and at the upper wire on the right side for two different initial gap heights. The liquid layer at the lower wire differs significantly for the two initial gap heights. At the gap height of 0.0047 m only a small liquid layer is formed at x= 0.03 m and x=0.125 m. In case of the gap height of 0.074 m a liquid layer from x=0.04 m to x=0.135 m is formed. At the upper wire the liquid layer starts to grow at x=0.015 m for the case with lower initial gap height. In contrast to that, at the initial gap height of 0.0074 m the liquid layer starts to grow at x=0.03 m. The differences can be traced back to the changes of the release point.

FIGURE 4.32 shows the development of the gap height for an initial gap height of 0.0076 m and 0.0047 m. The spatial position of the minimum at both curves differs significantly due to the change of the position of the release point. At higher initial gap height the gap height at the end of the domain is lower than the gap height at the beginning of the domain. Thus, in total dewatering takes place. In contrast to that at lower initial gap height no dewatering occurs.

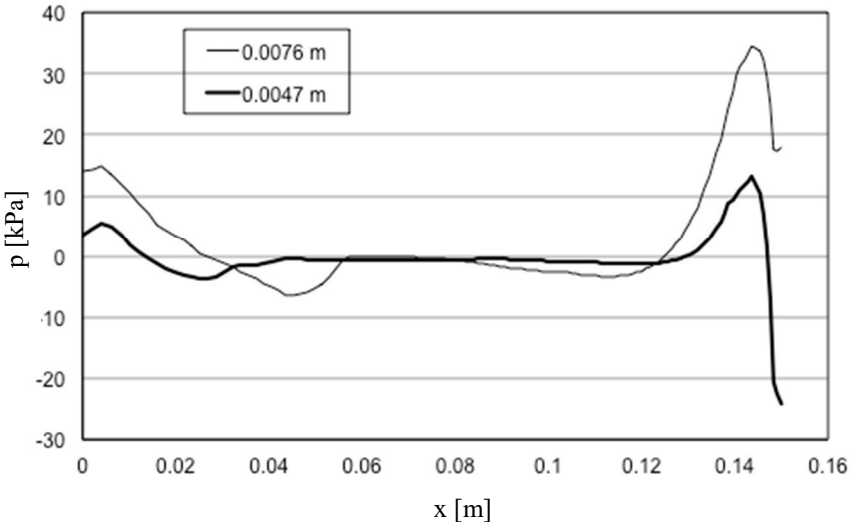

FIGURE 4.29: Pressure profile along the model domain at two initial gap heights. The influence of the initial gap height on the pressure profile is significant. At a higher initial gap height, the pressure is significantly higher at the forming roll position at x=0.02 m. At the end of the domain the pressure at higher initial gap height is significantly higher than at lower initial gap height

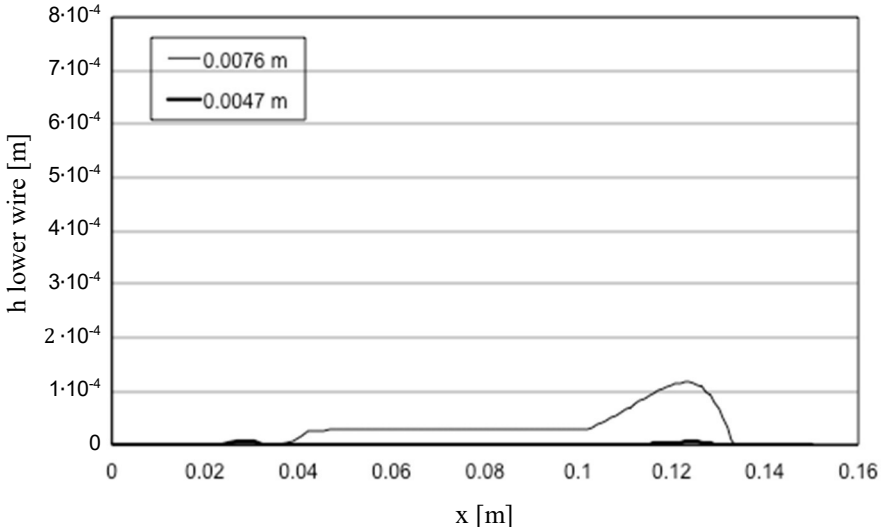

FIGURE 4.30: Liquid layer at the lower wire for two different initial gap heights. The liquid layer at the lower wire differs significantly for the two initial gap height. At the gap height of 0.0047 m only a small liquid layer is formed at x= 0.03 m and x=0.125 m. In case of the gap height of 0.074 m a liquid layer from x=0.04 m to x=0.135 m is formed.

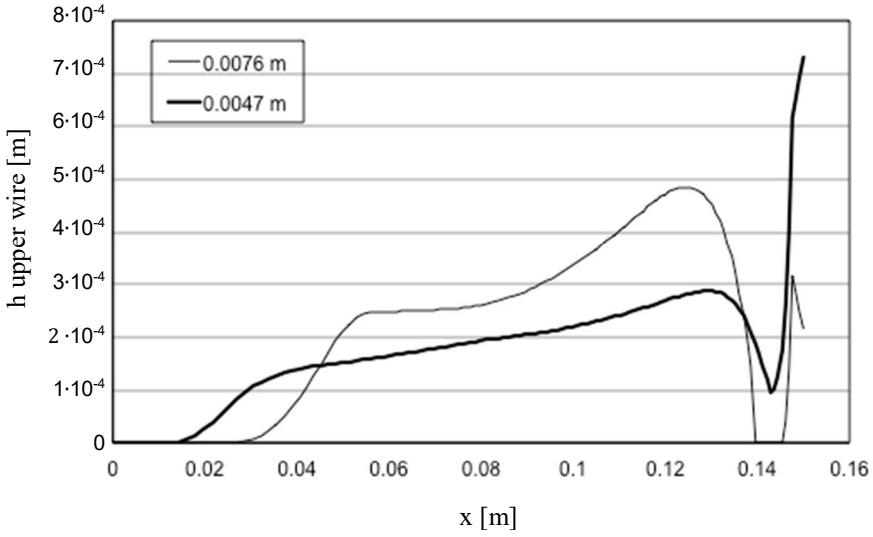

FIGURE 4.31: Liquid layer at the upper wire for two different initial gap heights. At the upper wire the liquid layer starts to grow at x=0.015 m for the case of a lower initial gap height. In contrast to that, at the initial gap height of 0.0074 m the liquid layer starts to grow at x=0.03 m. The differences are caused by the changes of the release point.

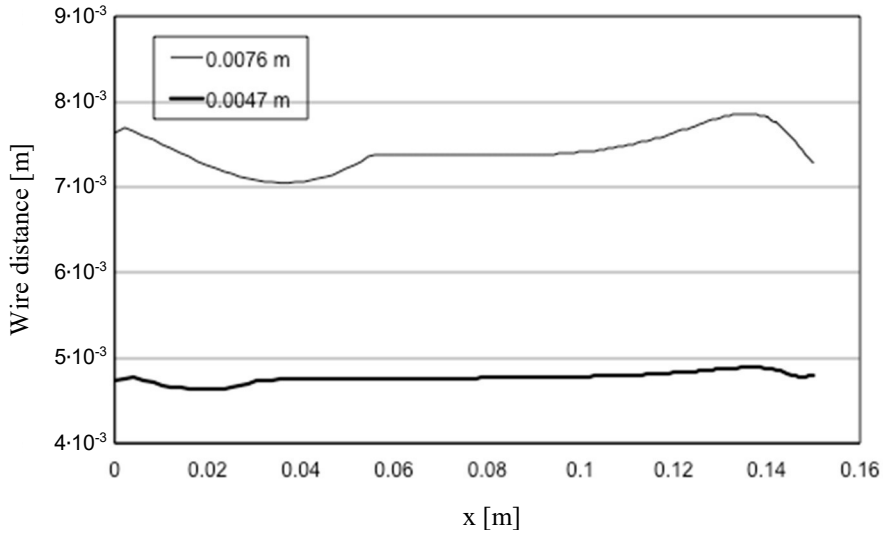

FIGURE 4.32: Development of the gap height at two initial gap sizes of 0.0076 m and 0.0047 m. The initial gap sizes are 0.0076 m and 0.0047 m. The minimum at both curves differs significantly.

4.4.7 Sensitivity analysis

The range of validity of the model is determined by a sensitivity analysis performed for the pressure profile by a variation of the parameters studied in section 4.4.3 to 4.4.6. The results at the x-position of 0.1411 m are taken to compare the behavior of the model. FIGURE 4.33 displays the pressure at a wire velocity between 2 and 25 m/s. The pressure seems to be reasonable up to a flow velocity of about 15 to 20 m/s. The pressure increases with increasing wire velocity. Above this level the pressure starts oscillating and decreases down to -92 kPa. This result does not seem to be reasonable since a negative pressure at this level would lead to high flow velocities and an unrealistic height of the liquid layer. For this velocity range, the model seems to be not appropriate. FIGURE 4.34 shows the pressure at wire tensions from 3000 to 20000 kN/m. At this range the pressure results are comparable to the ones observed by Schmidt-Rohr (2007). In FIGURE 4.35 the pressure versus the flow resistance of the wire from 21 kNs/m^3 to 121 kNs/m^3 is shown. The influence of the wire resistance is significant. An increase of the flow resistance from 21 kNs/m^3 to 40 kNs/m^3 leads to an increase of the pressure from approximately 30 kPa to 110 kPa. Schmidt-Rohr (2007) presents measured pressure values of about 30 kPa at this position. It is therefore assumed that values above this pressure level are caused by oscillations. FIGURE 4.36 shows the pressure versus the initial gap height at the inlet of the model domain. Up to a gap height of 0.008m the simulation results seem to be reasonable. Above this level oscillations occur.

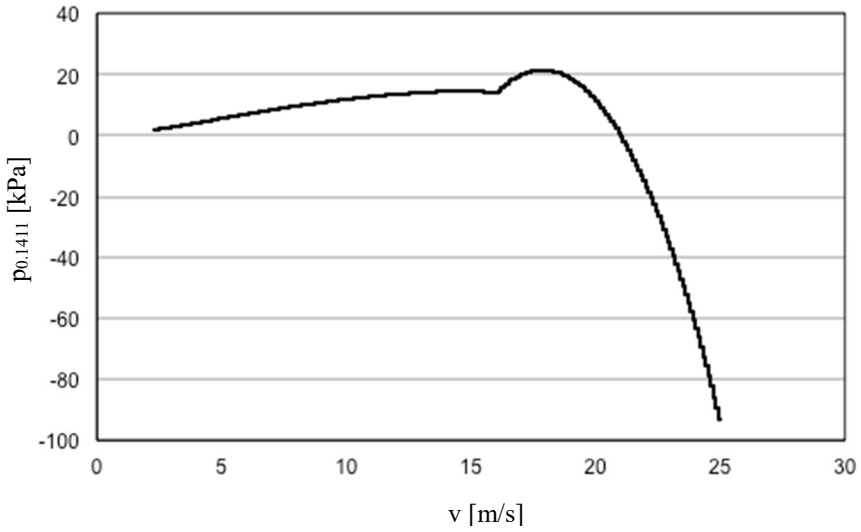

FIGURE 4.33: Internal pressure versus wire velocity at x= 0.1411 m.

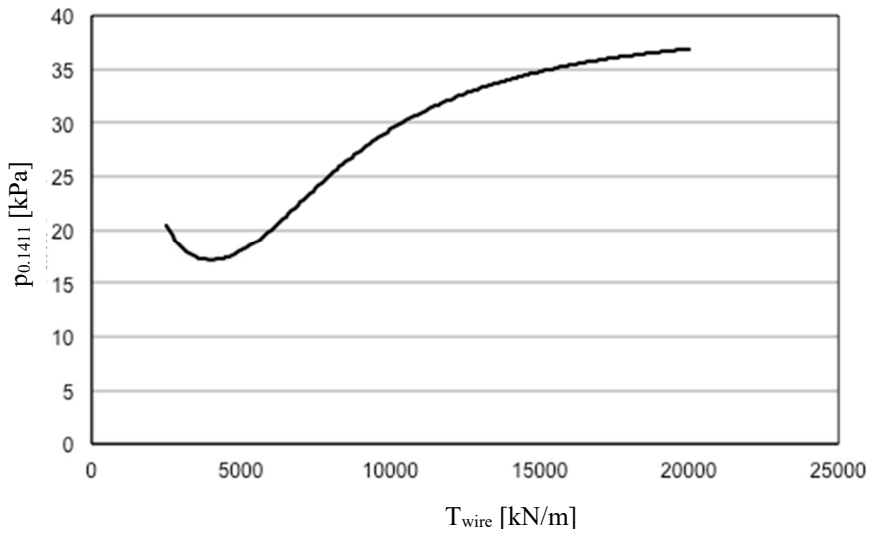

FIGURE 4.34: Internal pressure versus wire tension at x=0.1411 m.

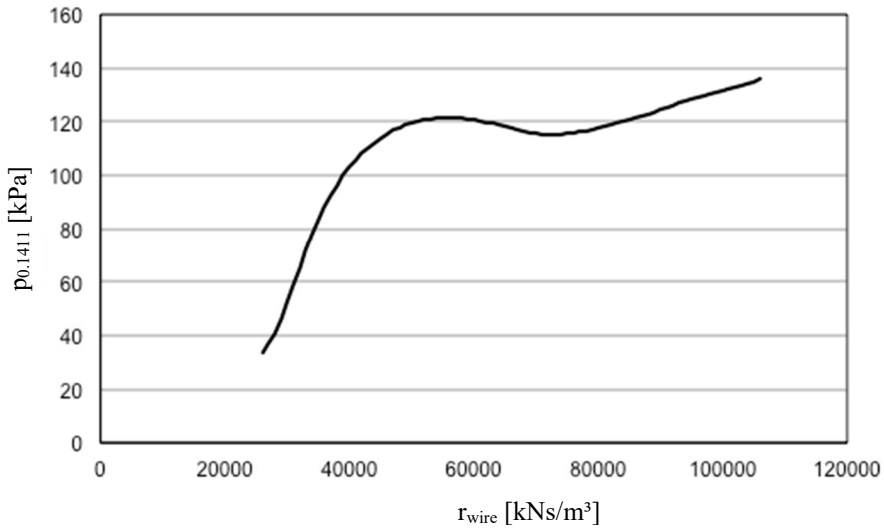

FIGURE 4.35: Internal pressure versus wire resistance at x= 0.1411 m.

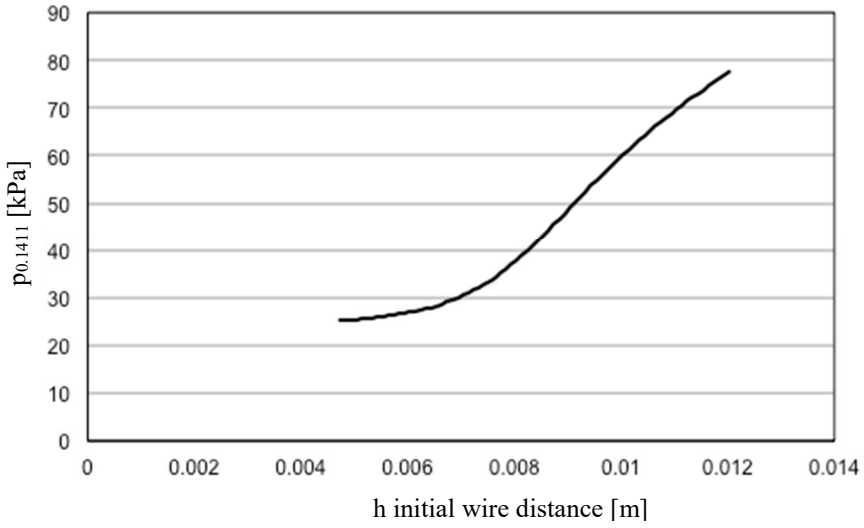

FIGURE 4.36: Internal pressure versus initial gap size at x=0.1411 m.

4.5 Conclusion

The presented simulation of a double wire former segment shows the influence of backflow on the pressure profile along the model domain. In the case of backflow water flows from outside of the wire into the gap between the wires whereby a liquid layer is formed. The model considers in the case of backflow only the flow resistance of the wire instead of the combination of the flow resistance of the wire and the fiber mat. Thus, in this model the flow resistance depends on the flow direction of the liquid. This approach is called “flow-direction-dependent flow resistance”. The model domain covers the unsupported wire between the forming roll and the first blade. This includes the calculation of the release point of the wire from the forming roll.

The simulation results show a good agreement to the pressure measurements at an industrial double wire former. This includes the positive as well as the negative pressure levels. This good agreement is only possible due to the flow-direction-dependent flow resistance. In contrast, the simulation of Holmqvist (2002) and Zhao & Kerekes(1995) show oscillating pressure at a flow resistance level of approximately 70 kNs/m^{3,} which corresponds to a basis weight of 10 g/m^2. In this work an initial flow resistance of 700 kNs/m^3 is assumed.

Chapter 5

5 Conclusion and future work

This thesis addresses the characterization of the flow through a mat of lignocellulosic fibers under hydrostatic compression at laboratory scale as well as in a simulated industrial environment.

The literature review in Chapter 0 shows that only few works deal with the characterization of the flow resistance behavior under hydrodynamic compression. The models for the flow through a fiber mat in a double wire former, which are available in the literature show results at high flow resistance that are not observed at an industrial former.

In Chapter 3, a test device is introduced to examine the relationship between the flow velocity, pressure loss, and fiber mat height during the flow through a fiber mat. The test device is validated and is in good agreement with flow resistance data of existing literature. The experimental results are used to calculate the viscoelastic and viscoplastic as well as the plastic and elastic deformation leading to characteristic changes in the flow resistance. The separation of the deformation components showed that the viscoelastic and viscoplastic changes in the filtration resistance at time spans smaller than 75 ms are an order of magnitude smaller than the elastic and plastic changes in a filtration resistance that occur in the first few milliseconds, which are considered as time-independent. For the simulation of the fiber mat in an industrial former section viscoelastic and viscoplastic deformations can therefore be neglected, since the duration of the pressure pulse is smaller than 30 ms.

In Chapter 4, a simulation of a section of a double wire former is presented. It shows the influence of backflow on the pressure profile along the model domain. The simulation results were in good agreement with the pressure measurements for an industrial double wire former. This includes the positive as well as the negative

pressure levels. It is assumed that this good agreement is achieved by considering a flow-direction-dependent flow resistance. This means that in the case of backflow only, the flow resistance of the wire is effective. In contrast, to that, Holmqvist (2002) and Zhao & Kerekes (1995) observed an oscillating pressure in the simulation results at a flow resistance level of approximetally 70 kNs/m^3, which corresponded to a basis weight of 10 g/m^2. In presented work, an initial flow resistance of 700 kNs/m^3 is assumed which corresponds to a basis weight of 35 g/m^2.

Future work

In this study, it was assumed that a full compression takes place as soon as the pressure is present. This simplification is not valid a priori. The typical pulse length in a double wire paper machine is between 1 and 10 ms at a reel speed of 20 m/s, assuming that the flow velocity is 0.05 m/s, and the acceleration time in the order of 0.1 ms. The height of a fiber mat is 0.1 mm. The time required for a complete compression of the fiber mat is 2 ms. This example shows that a full deformation of the fiber mat does not necessarily occur. Future experiments should be carried out, at which the fiber mat is not compressed completely.

As suggested by the experiments and the existing literature, the deformation behavior of the fiber mat depends on the deformation history. In future work, a model should be developed which covers these phenomena. A reasonable approach for this problem is a height-dependent deformation history. Different layers of the mat have a different history. A mass balance could be used for simulating the compression history. In the presented analysis, only full deformation has been considered. In order to model these phenomena and to include the compression history, an incremental formulation is required, that might be accomplished by using hysteresis operators. For a more detailed description, the reader is referred to Brokate & Sprekels (1996) and Visintin (1991).

In the experiments, it was observed that the fiber mat shows viscoplastic and viscoelastic deformation under hydrostatic pressure. The deformation rate seems to be velocity-dependent. For flow velocities below 0.02 m/s, no changes in the flow resistance could be observed. The relationship between the velocity and the changing rates in the flow resistance has not been not determined in the present work. A way to investigate this relationship would be the measurement of the mat deformation at different slopes of pressure decreases. A smaller deformation in trials where the pressure is increased slower would be an indication for the occurrence of creeping

occurring during the deformation. A similar approach should be applied for the description of the expansion process under hydrodynamic conditions.

In chapter 4, the concept of a flow-direction dependent-flow resistance was presented. This concept should also be implemented in modelling blade dewatering. As shown by Holmqvist 2002 the phenomenon of backflow occurs in the blade section as well. The model developed in this work would avoid oscillating simulation results, whereby the accuracy of the model would increase significant compared to the model of Holmqvist. The equation system for the blade section model is presented in Appendix A and B.

The sensitivity analysis shows that despite the implementation of the flow direction-dependent flow resistance, the range of validity is limited and does not cover the full range of process parameters of a typical industrial former. It is assumed that the inaccuracy of the model is caused by a simplified description of the process. As the simulation results show, high values for the flow resistance lead to high pressure values in the simulation which are out of the range of values observed in pressure measurements. It is therefore obvious that a further reduction of the flow resistance would reduce the maximum pressure. This can be achieved by assuming that air flows from outside of the wire to the inside of the wire after the liquid layer is removed. This seems to be reasonable, since at a pulse length of 1 ms a flow resistance of 21 kNs/m^3 a pressure level of 22 kPa and a liquid layer of 1mm is removed.

Appendix A

A Model for lower blade

The equation system for the lower blade model is shown below. The subscript u describes the upper wire, and the subscript l describes the lower wire.

$$R_l(W_l) = a_{1,l} W^{a_{2,l}} \tag{5.1}$$

$$c_{mat_l} \frac{d(uh_{m,l})}{dx} = -u_l(x) c_{sus_l} r_l \tag{5.2}$$

$$\frac{d(uh_{fl,l})}{dx} = u_l(x) \tag{5.3}$$

$$\frac{\mathrm{d}(\mathrm{u} \cdot (\mathrm{f} - \mathrm{g}))}{\mathrm{dx}} = \left(\frac{\mathrm{p} - \mathrm{p}_{e,l}}{\mathrm{R}_l}\right) \tag{5.4}$$

$$\mathrm{u}\frac{\mathrm{du}}{\mathrm{dx}} + \frac{1}{\rho} \cdot \frac{\mathrm{dp}}{\mathrm{dx}} = 0 \tag{5.5}$$

$$\mathrm{p} - \mathrm{p}_{\mathrm{e,l}} + \mathrm{p}_{\mathrm{d}} - \mathrm{T}_{\mathrm{l}} \cdot \frac{\mathrm{d}^2\mathrm{y}}{\mathrm{dx}^2} = 0 \tag{5.6}$$

Equation (5.1) governs the local flow resistance for the upper and lower wires. Equation (5.2) is the mass continuity equation for the upper and lower fiber mats. This equation differs from the general equation (4.8). In case of the lower wire, dewatering

occurs at a negative flow velocity. The accumulation of the liquid layer is governed by (5.2). The liquid layer at the lower wire increases at a positive flow direction. Therefore, the sign of the flow velocity in equation (5.3) differs from the general description in (4.10). The mass balance is shown in equation (5.4). The left term describes the accumulation of the mass, and the right term governs the flow through the wire. The momentum balance for the one-dimensional flow is governed by equation (5.5). Equation (5.6) determines the deflection of the upper and lower wire. The fact that the forces at the lower wire act in reversed direction are the reason for the sign change.

Appendix B

B Model for upper blade

The equation system for the upper blade model is shown below. Here the subscript u describes the upper wire and the subscript l describes the lower wire.

$$R_u(W_u) = a_{1,u} W^{a_{2,u}} \tag{5.7}$$

$$c_{mat_u} \frac{d(uh_{m,u})}{dx} = u_u(x) c_{sus_u} r_u \tag{5.8}$$

$$\frac{d(uh_{fl,u})}{dx} = -u_u(x) \tag{5.9}$$

$$\frac{d(u \cdot (f - g))}{dx} = \left(\frac{p - p_{e,u}}{R_u}\right) \tag{5.10}$$

$$u \frac{du}{dx} + \frac{1}{\rho} \cdot \frac{dp}{dx} = 0 \tag{5.11}$$

$$p - p_{e,u} + p_d + T_u \cdot \frac{d^2 y}{dx^2} = 0 \tag{5.12}$$

Equation (5.7) governs the local flow resistance for the upper and lower wire. Equation (5.8) is the mass continuity equation for the upper and lower fiber mats. In case of the lower wire, dewatering occurs at a negative flow velocity. The accumulation of the liquid layer is governed by (5.8). The liquid layer at the lower wire increases at for positive flow direction. Therefore, the sign of the flow velocity in equation (5.9) differs from the general description in (4.10). The mass balance is shown in equation (5.10). The left term describes the accumulation of the mass, and the right term governs the flow through the wire. The momentum balance for the one-dimensional flow is governed by equation (5.11). Equation (5.12) describes the deflection of the upper and lower wires. The fact that the forces at the lower wire act in reversed direction makes the sign change.

Appendix C

C Publications

Flitsch, J., Bauer, W., & Chen, Z. (2013). Experimental filtration study of wood fibers. In *Minisymposium Verfahrenstechnik*.

Flitsch, J., Bauer, W., & Hirn, U. (2016). A new approach to analyse the flow resistance and compression behaviour of a fibre mat. *Journal of Pulp and Paper Science*, *31(4)*

Bibliography

Adorj´an, L. A. (1975). A theory of sediment compression. In *In 11th International Mineral Processing Congress,* 297–318. Cagliari

Alles, C. M. (2000). Prozeßstrategien für die Filtration mit kompressiblen Kuchen. *PhD Thesis, Karlsuhe Institue of Technology, Karlsruhe.*

Baines, W. D. (1967). The Papriformer Part II. Flow in the Formation Zone of a Two-Wire Machine. *Pulp and Paper Magazine of Canada*, 68(10), 497–505, 538.

Batchelor, G. K. (1972). Sedimentation in a Dilute of Spheres. *Journal of Fluid Mechanics*, 52, 245-268.

Bellani, G. (2011). Experimental studies of complex flows through image-based techniques. *PhD Thesis, Royal Institute of Technology, Stockholm.*

Bergqvist, A. (1994). On Magnetic Hysteresis Modeling. *PhD Thesis, Royal Institute of Technology, Stockholm.*

Boxer, T., Dodsen, C. T. J., & Sampson, W. W. (2001). Anlalytic solution to the Martinez dewatering equations for roll gab formers. *Journal of Pulp and Paper Science*, 26(11):391-394.

Brokate, M., & Sprekels, J. (1996). Hysteresis and Phase Transition. *Springer Verlag.*

Buscall, R., Mills, P. D. A., & Yates, G. E. (1986). Viscoelastic properties of strongly flocculated polystyrene latex dispersions. *Colloids and Surfaces*, 18(2-4), 341–358.

Buscall, R., & White, L. R. (1987). The consolidation of concentrated suspensions. Part 1. The theory of sedimentation. *Journal of the Chemical Society, Faraday Transactions 1*, 83(3), 873-891.

Campbell, W. B. (1947). The Physics of Water Removal. *Pulp and Paper Magazine of Canada*, *Convention*, 103–122.

Channell, G. M., & Zukoski, C. F. (1997). Shear and compressive rheology of aggregated alumina suspensions. *AIChE Journal*, 43(7), 1700–1708.

Chen, Z. (2014). Compressability of Fibre Mat. *Master Thesis, Karlsuhe Institue of Technology, Karlsruhe.*

Dalpke, B. (2002). Modelling of the impingement and early roll forming. *PhD Thesis, Universitiy of British Columbia.*

Dalpke, B. (2004). Modelling jet impingement and the initial drainage zone in roll forming. *Journal of Pulp and Paper Science*, 30(3), 65 – 70.

Dalpke, B., & Green, S. I. (2000). Modelling of jet impingement in twin-wire paper-machines: Impingement on one fabric. *Tappi Journal*, 84(2).

Flitsch, J., Bauer, W., & Chen, Z. (2013). Experimental filtration study of wood fibers. In *Minisymposium Verfahrenstechnik*.

Flitsch, J., Bauer, W., & Hirn, U. (2016). A new approach to analyse the flow resistance and compression behaviour of a fibre mat. *Journal of Pulp and Paper Science*, 31(4).

Forchheimer, P. (1901). Wasserbewegung durch Boden. *VDIZ 45*, 1782–1788.

Grace, H. P. (1953). Resistance and compressibility of filter cakes. Part I-III. *Chem. Eng. Progr.* 49, 303-318.

Green, S. I., & Kerekes, R. J. (1998). Numerical analysis of pressure pulses induced by blades in gap formers. *Tappi Journal*, 2(4), 180–187.

Gren, U., & Ljungkvist, K. (1983). Compressibility and permeability of chemical pulps. some notes on the effect of beating. *Cellul. Chem. Technol.*, 17(9-10), 515–523.

Gooding, R., McDonald, J.D., Rompre, A., and Green, S.I. (2004) "Measurements of Pressure Pulses From Blades in a Gap Former," *PAPTAC Conference*, Montreal, January 26-29.

Han, S. T. (1962). Drainage in a Vacuum Former. *Tappi Journal*, 45(4), 292–295.

Hergert, R., & Sandford, L. (1982). Pressure Measurements in the Forming Zone of a Twin-Wire Tissue Machine. In *Intl. Water Removal Symp.*, 47–50, Vancouver, Canada.

Herzig, R., & Johnson, D. B. (1999b). Investigation of thin fiber mats formed at high velocity. *Tappi Journal*, 82(1), 226–230.

Hisey, R. W. (1956). An Investigation of the Mechanism of the Dewatering of Compressible Beds. *Tappi Journal*, 39(10), 690–696.

Holm, R. (2002). On the Fluid Mechanics of Partial Dewatering during Roll Forming in Paper Making. *PhD Thesis, Royal Institute of Technology, Stockholm.*

Holm, R., Söderberg, D., Kth, S., & Norman, B. (2005). Experimental studies on dewatering during roll forming of paper. *Nordic Pulp And Paper Research Journal*, 20(2), 205–211.

Holmqvist, C. (2004). Modelling of the Pressure Distributions in Twin-Wire Blade Formers. *Pulp and Paper Canada,* 105(10), 47-50.

Holmqvist, C. (2002). Modelling of the Pressure Distributions in Twin-Wire Blade Formers . *PhD Thesis, Royal Institute of Technology, Stockholm.*

Howells, I., Landman, K. A., Panjkov, A., Sirakoff, C., & White, L. R. (1990). Time-dependent batch settling of flocculated suspensions. *Applied Mathematical Modelling,* 14(2), 77-86.

Hubbe, M. A. (2007). Flocculation and redispersion of cellulosic fiber suspension: A review of effects of hydrodynamic shear and polyelectrolytes. *Bioresources*, 2(2), 296–331.

Ingmanson, W. L. (1952). An investigation of the mechanism of water removal from paper slurries. *Tappi Journal*, *35*(10), 439–448.

Ingmanson, W. L. (1953). Filtration Resistance of Compressible Materials. In *Chem. Eng. Progr.,* 49(11), 577-584.

Ingmanson, W. L. (1957). Filtration Resistance on the Fourdrinier Tabel Roll Section. *Tappi*, 40(12), 936-943.

Ingmanson, W. L., & Andrews, B. D. (1959). The Effect of Beating on Filtration Resistance and Its r , Components of Specific Surface and Specific Volume. *Tappi*, 42(1), 29–35.

Ingmanson, W. L., & Whitney, R. P. (1954). The Filtration Resistance of Pulp Slurries. *Tappi Journal*, *37*(2), 523.

Jackson, G. W., & James, D. A. V. I. D. F. (1986). The Permeability of Fibrous Porous Media. The Canadian Journal of Chemical Engineering, 64(3), 364-374.

Johnson, P. C., & Jackson, R. (1987). Frictional–collisional constitutive relations for granular materials, with application to plane shearing. *Journal of Fluid Mechanics*, 176(1), 67–93.

Jones, R. L. (1963). The Effect of Fiber Structural Properties on Compression Response of Fiber Beds. *Tappi Journal*, 46(1), 20–28.

Jong, J. H. (1998). Characteristics of Jet Impingement, Drainage and Compression in a Forming Roll of a Twin-Wire Machine. *PhD Thesis, Industrial Engineering*. Toronto.

Jong, J. H., Baines, W. D., & Currie, I. G. (1999). Experimental Characteristics of Forming Fabrics and Fibre Mats. *Journal of Pulp and Paper Science*, 25(3), 95–99.

Kalliokoski, J. (2011). Models of filtration curve as a part of pulp drainage analyzers. *PhD Thesis, Royal Institute of Technology, Stockholm.*

Kataja, M., & Hirsilä, P. (2001). Application of Ultrasound Anemometry for Filtration of Fiber Suspension, *12th Fundamental research symposium, Oxford, UK* (Vol. 2, pp. 591–604). Jyväskylä, Finland.

Krook, K. (1996). Press Drying of Paper, An Experimental study of Heat transfer and Quality changes in Hot Pressing of Wet Paper Webs. *PhD Thesis, University of Lund*, Sweden.

Landman, K. A., White, L. R., & Buscall, R. (1988). The Continuous-Flow Gravity Thickener : Steady State Behavior. *Power*, *34*(2), 239–252.

Lindström, S. B. (2008). Modelling and Simulation of Paper Structure Development. *PhD Thesis. Mid Sweden University*, Sweden.

Lobosco, V. (2004). On the Modelling of Mechanical Dewatering in Papermaking. *PhD Thesis, Royal Institute of Technology, Stockholm.*

Lobosco, V., Norman, B. and Östlund, S. (2005). Modelling of Forming and Densification of Fibre Mats in Twin-Wire Formers, *Nordic Pulp and Paper Research Journal*, 20(1), 1623.

MARTINEZ, D. M. (1998). Characterizing the Dewatering Rate in Roll Gab Formers. *Journal of Pulp and Paper Science,* 24(9). 281-285.

Ng, S. (1990). Dry forming technology- assessment and testing of air fiber suspensions in forming systems. *PhD Thesis, Queen's University,* Canada.

Ng, S., Grandmaison, E. W., & Topolinsky, D. (1990). Pressure drop measurements in dry-formed wood fiber webs, *Tappi Conference (August),* 1–4.

Norman, B., & Söderberg, D. (2001). Overview of forming literature, 1990-2000, In: The Science of Papermaking. *Transactions of the 12th Fundamental. Oxford, UK.* 17-21, 9.2001. *The Pulp and Paper Fundamental Research Society,* Vol. 1, 431–558.

Parker, J. D. (1972). The Sheet-Forming Process. *Tappi Press* (Vol. Atlanta (U, p. 1). Atlanta (USA).

PIRES, E. C., SPRINGER, A. M., & KUMAR, V. (1989). A new technique for specific filtration resistance measurement. *Tappi Journal*, 72(7), 149–154.

Radvan, B., & Gatward, A. P. J. (1972). The Formation of Wet-Laid Webs by a Foaming Process. *Tappi Journal*, 55(6), 748–751.

Ripperger, P. (n.d.). Mechansiche Verfahrenstechnik (pp. 1–190). TU Kaiserslautern.

Robertson, A. A., & Mason, S. G. (1949). Specific surface of cellulose fibers by liquid permeability method. *Pulp Paper Magazine of Canada*, 50(13), 103–110.

Roshanzamir, A. (2000). *Hydromdynamics of blade gap formers*. *PhD Thesis, University of British Columbia,* Canada.

Roshanzamir, A., GREEN, S. I., & Kerekes, R. J. (2000). Two-Dimensional Simulation of Suction Shoes in Gab Formers. *Journal of Pulp and Paper Science*, *26*(4), 158–163.

Roshanzamir, A., Kerekes, R. J., & Green, S. I. (1999). Hydrodynamic Pressure Generated by Doctoring in Blade Gap Formers. In *Tappi Engineering/ Process and Product Quality Conference & Trade Fair*, 1181-1189.

Sayegh, N. N., & Gonzalez, T. O. (1995). Compressibility of Fibre Mats During Drainage. *Journal of Pulp and Paper Science*, *21*(7), 255–261.

Schmidt-Rohr, V. (2007). Versuche mit einem Blastkasten hinter der Saugzone der Formierwalze im DuoFormer TQV. *Heidenheim: Voith Paper (internal Report).*

Shirato, M., & KATO, H. (1970). ANALYSIS OF SETTLSNG OF THICK SLURRIES DUE TO CONSOLIDATION. *J. Chem. Engng Japan*, 3(1), 98–104.

Tiller, F. M. & Hsyung, N. B. (1993). Unifying the theory of thickening, filtration, and centrifugation. *Water Science Technology*, 28(1), 1-9.

Torvinen, K., & Kiiskinen, H. (2014). Foam forming gives bulky board at a high dry solids content. In *Progress in Paper Physics Seminar*. Raleigh, North Carolina, USA, September 8-11.

Visintin, A. (1991). Differential Models of Hysteresis, first edn. New York: Springer Verlag.

Vomhoff, H. (1998). Dynamic compressibility of water- saturated fibre networks and influence of local stress variations in wet pressing. *PhD Thesis. Royal Institute of Technology,* Sweden.

Vomhoff, H., & Schmidt, A. (1997). The steady-state compressibility of saturated fibre webs at low pressures. *Nordic Pulp And Paper Research Journal*, 12(4), 267-269.

Wahren, D., & Meyer, H. (1964). On the elastic properties of three-dimensional fibre networks. *Svensk Papperstidn.*, 67(10), 432–436.

Wilder, H. D. (1960). The Compression Creep Properties of Wet Pulp Mats. *Tappi*, 43(8), 715–720.

Wildfong, V. J., Genco, J. M., Shands, J. A., & Bousfield, D. W. (2000a). Filtration Mechanics of Sheet Forming. Part I: Apparatur for Determination of Constant-Pressure Filtration Resistance. *Journal of Pulp and Paper Science*, 26(7), 250–254.

Wildfong, V. J., Genco, J. M., Shands, J. A., & Bousfield, D. W. (2000b). Filtration mechanics of sheet forming. Part II : Influence of fine material and compression. *Journal of Pulp and Paper Science*, 26(8), 280–283.

Zahrai, S., & Bark, F. H. (1995). On the fluid mechanics of twin wire blade forming in paper machines, 10(4), 245–252.

Zhao, R. H., & Kerekes, R. J. (1995). Pressure Distribution Between Forming Fabrics in Blade Gap Formers: Thin Blades. *Journal of Pulp and Paper Science*, 21(3), 91–103.

Zhao, R. H., & KEREKES, R. J. (1996). The effect of consistency on pressure pulses in blade gap formers.pdf. *Paperi Ja Puu*, 78(1-2), 36–38.